

SELF-CALIBRATION FOR A HEXAPOD COORDINATE MEASURING MACHINE

By

CHIN-CHOU HUANG

A DISSERTATION PRESENTED TO THE GRADUATE SCHOOL
OF THE UNIVERSITY OF FLORIDA IN PARTIAL FULFILLMENT
OF THE REQUIREMENTS FOR THE DEGREE OF
DOCTOR OF PHILOSOPHY

UNIVERSITY OF FLORIDA

1998

Copyright 1998

by

Chin-Chou Huang

To my beloved parents and my wife, Yalin

ACKNOWLEDGMENTS

I would like to thank Dr. John Ziegert for giving me the chance to work on this project, and introducing me into the world of metrology. Without his guidance and support, this research would never have been possible. I also would like to thank Dr. Joseph Duffy who first taught me the concept of a hexapod machine. I would also like to express my gratitude to Dr. Ali Seireg and Dr. Paul Mason who taught me the skills necessary for optimal design and estimation. Thanks also to Dr. Chat Ho for his assistance on mathematics.

My colleagues at the University of Florida Machine Tool Research Center have been extremely generous with advice and assistance above and beyond the bounds of common decency. Thanks to Andy Smith, Doug Yeager, and Bernie Jokiel for working through many problems with me through my time in the MTRC. A special thanks is due to Ben Sanders of the Procter and Gamble Company for his assistance in correcting my writing.

TABLE OF CONTENTS

	<u>page</u>
ACKNOWLEDGMENTS	iv
ABSTRACT	vii
CHAPTERS	
1 INTRODUCTION	1
1.1 Conventional Coordinate Measuring Machine.....	1
1.2 Hexapod Coordinate Measuring Machine.....	3
1.3 Scope of Research	9
2 LITERATURE REVIEW	11
2.1 Open-Loop Kinematic Calibration	13
2.2 Closed-Loop (Parallel Mechanism) Kinematic Calibration	19
2.3 Conclusion.....	24
3 MODELING, MEASUREMENT AND IDENTIFICATION	25
3.1 Kinematic Modeling.....	26
3.2 Measurement	29
3.3 Identification	31
3.4 Conclusion.....	39
4 MEASUREMENT STRATEGY.....	40
Condition Number.....	41
5 CALIBRATION SIMULATION	47
5.1 Simulation Setup and Environment	48
5.2 Measurement Strategy	50
5.3 The Effect of Linear Displacement Measurement Error on Sphere Position.....	55
5.4 The Effect of Measurement Uncertainty on Calibration Results	57
5.5 The Effect of Pose Selections on Calibration Results	62
5.6 The Effect of Number of Poses on the Calibration Results	65
5.7 The Sensitivity Analysis on Condition Number.....	69
5.8 The Effect of Nominal Value on the Calibration Results	73
5.9 The Comparison of Identification Methods	76

5.10 Discussion	77
6 THERMAL EFFECT	79
6.1 Thermally Sensitive Components	80
6.2 The Thermal Response in The Sensitive Components.....	84
6.3 The Effect of the Heat Generated in Actuators	103
6.4 Conclusion.....	105
7 HCMM MEASUREMENT UNCERTAINTY ANALYSIS.....	110
7.1 Error Sources In Strut Displacement Measurement	110
7.2 The Combined Standard Uncertainty	118
7.3 Probe Positional Uncertainty Due to Calibration Error.....	123
7.4 Probe Position Uncertainty Due to Thermal Error and Strut Displacement Measurement Error	127
7.5 The Overall Probe Positional Uncertainty.....	132
8 CONCLUSIONS AND FUTURE WORK.....	134
8.1 Conclusions	134
8.2 Future Work	134
APPENDICES.....	136
A OBSERVABILITY INDICES	136
B OPTIMAL POSE SETS	138
C MATLAB COMMAND FILES	143
LIST OF REFERENCES	154
BIOGRAPHICAL SKETCH.....	158

Abstract of Dissertation Presented to the Graduate School
of the University of Florida in Partial Fulfillment of the
Requirements for the Degree of Doctor of Philosophy

SEFL-CALIBRATION FOR A HEXAPOD COORDINATE MEASURING MACHINE

By

Chin-Chou Huang

May 1998

Chairman: Dr. John C. Ziegert

Major Department: Mechanical Engineering

The Hexapod Coordinate Measuring Machine (HCMM) is composed of six telescoping struts with laser interferometric displacement measurement and a single fixed-length center rod. The laser interferometers measure the length changes of each strut. However, in order to calculate the coordinate of the probe, it is necessary to know the absolute length of each strut and the distance between the three joints. Thus there are nine kinematic parameters to be determined in the calibration process. The nine parameters are the three base lengths and the initial lengths of the six struts.

This research presents a method to find the initial strut lengths and the base joint locations without adopting any external artifacts or measurements. During calibration the measuring probe is moved to a number of different positions within the measuring volume. For each position, the center rod length is assumed to remain constant. The length is calculated based on an initial guess at the machine kinematic parameters. A

non-linear least squares problem is then formulated to search for the values of the base locations and initial strut lengths which minimize the variation in the computed center rod length.

A computer simulation of the self calibration process has been implemented. Noise content in each laser interferometric measurement signal was monitored to determine its effect on the quality of the calibration results. It was found that the magnitude of calibration uncertainty is proportional to the magnitude of the noise level. The simulation tool also found that the data collected from some specific motions is insufficient for calibration use. Thus, the observation indices were used to determine the usability of a data set. This research also investigated the influence of the number of position used for calibration and how it related to the uncertainty of the identified parameters. Experiments were performed to estimate the thermal time constants of the HCMM components. Thus, one can determine the time period that the HCMM has to be re-calibrated. In the final of this research, we demonstrated how to evaluate the HCMM volumetric error.

CHAPTER 1 INTRODUCTION

A conceptual five degree of freedom hexapod coordinate measuring machine (HCMM) was proposed by Jokiel and Ziegert [1]. The research presented in this paper is directed toward the development of the self-calibration algorithm for the HCMM.

1.1 Conventional Coordinate Measuring Machine

Based on a machine's accuracy, price, work volume, and throughput, Slocum [2] categorized the coordinate measure machines (CMMs) into three market brackets: ultraprecision, throughput, and small manual machines. Those CMMs in the ultraprecision group have to achieve submicron accuracy. Only a few machines were being sold worldwide because of their high cost and the great amount hand finishing involved in their manufacture. The throughput group was responsible for the sale of a great number of machines worldwide. These machines typically display accuracy on the order of 400 to 600μ inch (10 to $15\mu\text{m}$) and were capable of making rapid computer controlled measurements. The last bracket of CMMs, in general, was made up of small and benchtop type machines. The market for these smaller machines is fairly limited and highly competitive.

Typically a CMM uses serial kinematic linkages, each providing a degree of freedom. The configuration could be a bridge type or cantilever construction. Generally these designs employ a three-dimensional rectilinear Cartesian coordinate system since

the design is based on three mutually perpendicular prismatic joints. A probe system which establishes the relationship between the workpiece and the machine coordinate system is attached at the end of last serial link. The commonly used bridge type CMM is shown in Figure 1-1.

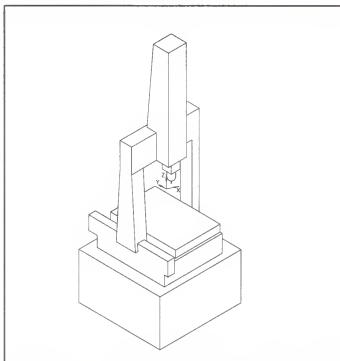


Figure 1-1 Bridge type CMM

When a probe touches a workpiece, its position is actually determined from displacement transducers which are embedded along each of the three axes of CMM. Thus, the structure must be stiff enough to avoid deflections. The required stiffness is commonly achieved using a large structure with high mass. These large masses and their associated high moment of inertia must be driven by the machine drive and control. A high-performance CMM is characterized not only by accuracy, but also by the ability to

move quickly from point to point while making “measurements on the fly.” Heat generation from such a high speed, high power driving system required to quickly move large, high stiffness machine elements, would cause significant distortions of the machine. In order to provide high accuracy measurements the CMM has to be placed in a temperature-controlled environment to minimize the structural distortion due to thermal gradient in the machine elements. Therefore, the total cost for the machine itself and the creation and maintenance of the required working environment is a significant economic issue for CMM users.

1.2 Hexapod Coordinate Measuring Machine

An alternative is the hexapod coordinate measuring machine (HCMM). This machine uses a parallel kinematic structure in which light weight telescoping struts are used to reduce the heavy driving power needed in the conventional CMMs. The HCMM is designed to self-calibrate and compensate for thermally induced changes in its own elements. Thus, the requirements for temperature control in the operating environment are greatly reduced.

The HCMM is composed of six telescoping struts and a single fixed-length center rod. The six telescoping struts are mounted in pairs, with one pair at each of the three spherical joints around the base of the machine. One strut from each pair mounts to the top of the center rod, and one strut from each pair mounts to the bottom of the center rod. Each telescoping strut carries a laser interferometric sensor to measure its length. The configuration of the machine resembles two tetrahedrons which share a common base and whose apex points are connected by the fixed rod. A probe is attached to the lower

sphere such that the probe tip is collinear with the center rod. This kinematic design gives the center rod five degree of freedom (5-DOF) to move within the work space. The prototype HCMM is shown in Figure 1-2. The expected HCMM system performance was outlined by Jokiel in his thesis [3] as follows

1. Overall accuracy: $\pm 89\mu$ to $\pm 213\mu$ inch (2.2 to 5.3 μ m)
2. Workspace: A cylindrical volume 15 inches in diameter and 15 inches in height.
3. Speed: Maximum constant probe speed of 30 in/sec. Strut extension speed of 25 in/sec.

The HCMM can be divided into four subsystems: driving and control subsystem, displacement measurement subsystem, kinematic (geometry) subsystem, and calibration subsystem. Each of the subsystems is dedicated to achieving a critical part of the overall accuracy and performance requirements. A brief description of each subsystems follows:

Driving System

A prototype servo actuated strut of the HCMM was designed and manufactured by Mevoli [4]. The maximum and minimum strut lengths are 30 inches minimum and 50 inches maximum. A rotating nut type drive was used to drive a hollow ball screw and to achieve the required speed. The hollow ball screw allows the laser light to pass through. The strut and the drive system are shown in Figure 1-3. Its maximum acceleration capacity is 64.4 ft/s^2 or 2G.

Displacement Measurement System

The HCMM's linear displacement measurement system is modified from an instrument called the Laser Ball Bar, developed by Ziegert and Mize [5]. It consists of a

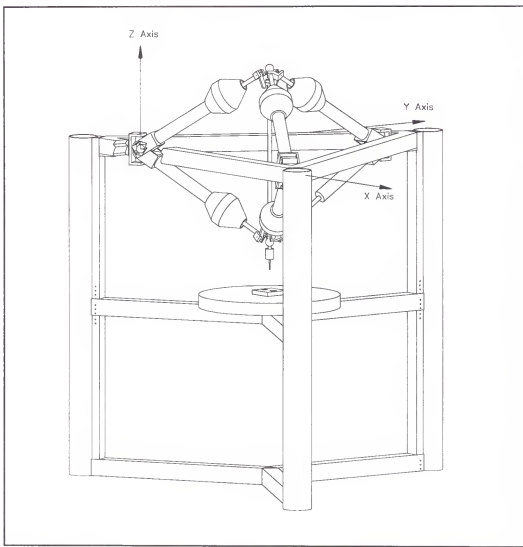


Figure 1-2 The hexapod coordinate measuring machine

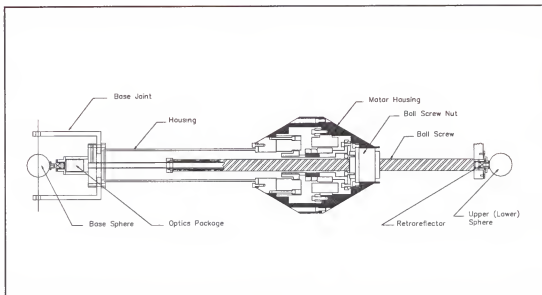


Figure 1-3 The strut and actuating system

heterodyne laser interferometer with a length measurement uncertainty of $\pm 10\mu$ inch or $\pm 0.25\mu$ meter. Two red laser waves generated by HeNe laser with nearly the same frequency are shot out from an emitter which is located at one end of the strut near the base sphere to a moving retroreflector. The moving retroreflector which functions as a mirror is mounted at the other end of the ball screw near the moving sphere. A phase detector is used to measure the phase difference ($\Delta\phi$) between the laser beam as it leaves the laser head and the reflected beam. Thus, the relative distance traveled by the retroreflector is found as

$$\Delta x = \frac{\Delta\phi \lambda}{4\pi} \quad (1-1)$$

where λ is the red light wave length (632.8 nm) from the HeNe laser. Thus, the distance change between the fixed sphere (or base sphere) and the moving sphere could be measured by the above system. Figure 1-4 illustrates how the heterodyne laser

interferometer works. The Δf_1 shown in Figure 1-4 is the frequency shift caused by Doppler effect when the retroreflector moves. The advantage of the laser interferometer is that it has a relatively small measurement uncertainty and is less sensitive to temperature change compared with other displacement measurement devices. However, it has to be noted that the laser interferometer can only measure relative changes in the length of strut. The initial strut length is unknown. Thus, the HCMM needs to perform an initialization (or calibration) procedure to determine the initial strut length before it can be used to take functional measurements.

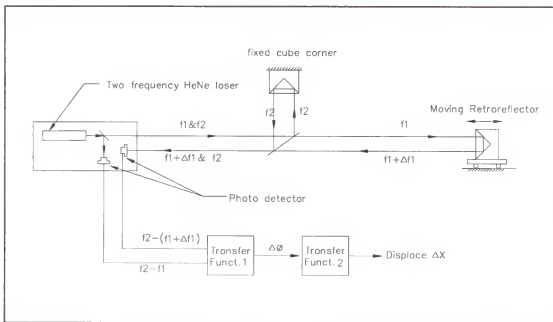


Figure 1-4 Illustration of a heterodyne laser interferometer

Kinematic System

In order to overcome the static and dynamic deflections under actuation forces, the structure has to be very stiff. A maximum of 200 pound force acting on each strut,

each spherical joint and each of the three supporting columns is estimated and is used for determining the dimensions and materials of the structure. Angular contact bearings are installed on all the spherical joints to prevent deflection in their axial direction.

Because the spheres in the base and moving joints provide constant references for length measurement, the imperfections in the form of the spheres will result directly in measurement error along the length of each strut. Therefore, using spheres with highly accurate spherical form is very important. For instance, a grade 5 sphere has a spherical form tolerance of $5.0\mu\text{in}$ ($0.125\mu\text{m}$). The solid triangle frame is made of steel to provide a heavy thermal mass and, consequently, to create a large thermal time constant. The symmetric kinematic structure design also provides symmetric thermal expansion and thus reduces the thermally induced distortion of the structure.

In addition to the measurement accuracy considerations, many other factors have to be considered during the design stages of the HCMM such as the operation safety, part loading convenience, manufacturing costs and the ease of machine installation.

Calibration System

The accuracy of the HCMM depends on the knowledge of the absolute length of each side of the dual tetrahedron kinematic linkage. If there is any measurement error on the displacement sensor (or the laser interferometer), it will result in an error of the measured strut length. Therefore, a frequent calibration for the laser interferometer is important. In addition to the first level calibration, the nominal kinematic parameters need to be calibrated frequently. The nominal kinematic values may be obtained from the blue print of the design drawing, but the errors from manufacturing, installation, and thermal effects are inevitable. A calibration technique for finding the actual kinematic

parameters is needed before the machine can make any measurement. The development of such a calibration technique is the primary objective of this research.

1.3 Scope of Research

As mentioned earlier, the HCMM accuracy depends on the knowledge of the kinematic parameters. Though the laser interferometer measurement system is used in this machine, it only provides the relative length changes of the struts. The initial strut lengths and the distances between base spheres must be determined.

Finding the actual kinematic parameters for a hexapod machine is much more difficult than for a traditional Cartesian type machine. Over the past two-hundred years people have established a mature technique to find the parametric errors of the Cartesian type machines. In contrast, the application of a hexapod coordinate measuring machine with parallel geometry is a recent development. The calibration techniques currently in use for finding the parametric errors for parallel structural machines require highly accurate external measurement devices and the process is very time consuming. Moreover, the calibration technique is different from machine to machine. Even if the kinematic parameters have been obtained, these values will keep changing when the environmental temperature varies. For instance, a one meter long steel bar will have a length change of 13 to 21 μm (520 to 840 μin) when it is subjected to 1 °C (1.8 °F) temperature change. In the traditional Cartesian machines one has to perform a correction procedure to compensate for the thermally induced errors. The development of a fast simple, and reliable calibration method for the HCMM would allow for the online self-

calibration of kinematic parameters and absolute measurement lengths to compensate for basic structural and thermally induced variations of the machine elements.

The research presented in this paper is dedicated to the development and analysis of a self-calibration method for the kinematic parameters of the HCMM. In addition, a basic understanding of the thermally induced error on the machine is within the scope of this research. Thus, the required frequency of re-calibration when the HCMM is subjected to a thermally variant environment can be determined.

CHAPTER 2 LITERATURE REVIEW

In general machine geometry error calibration includes four main steps: (1) kinematic modeling (2) measurement (3) error identification (4) error compensation. Kinematic modeling establishes a mathematical model which relates the machine kinematic parameters to the resulting pose of the machine. Measurement collects physical data which contains information relating the input of the model to the output. If the geometric errors are directly measured, the kinematic parameters of the machine are identified individually. If only the spatial coordinates of the end-effector or the probe tip are measured, the geometric errors and kinematic parameters have to be identified by an identification procedure. When the errors of kinematic parameters are identified, use of this information to correct the machine performance is called error compensation.

We separate machines into two categories: serial kinematic machines and parallel kinematic machines. The serial mechanisms have a open loop structure such as machine tools, Cartesian type coordinate measuring machines, or serial robots. The parallel mechanisms have a closed loop parallel kinematic structure such as hexapod milling machines, Stewart platforms, or the HCMM. In each category we classify the calibration method into two sub-categories: “*require external calibrated standards*” and “*without calibrated standards*” according to the use of the measurement device. The “without calibrated standards” calibration also is referred to as the self-calibration method. For example, the laser interferometer measurement device (an external, calibrated standard)

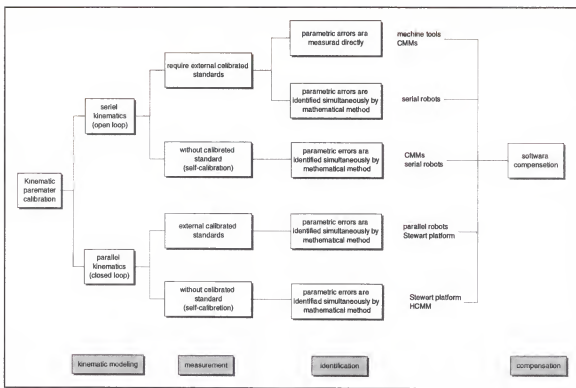


Figure 2-1 The kinematic calibration categorization

is used for the machine tool calibration. In contrast, the center rod (an internal machine component, not a calibrated standard) is used for the HCMM calibration.

According to the identification method, the “require calibrated standards” group in the open loop machines is further separated into two groups: “*the direct measured*” where each of the parametric errors is measured individually, and “*the indirect measured*” where the parametric errors are identified simultaneously by a mathematical method. The calibration categorization is shown in Figure 2-1. A total of five groups are categorized by our classification.

2.1 Open-Loop Kinematic Calibration

Group 1: Direct Measured

The first group of machines in calibration are the machine tool and Cartesian type CMM. In general, a kinematic error model will be first created to relate input command and the position of the tool tip in a machine tool or the position of the probe in a CMM.

The function can be written as:

$$\delta P = [T] \delta e \quad (2-1)$$

δP represents the position errors between the actual and the desired position. $[T]$ is a transformation matrix that is formed by the machine configuration. δe is the error parameters needed to be identified such as the displacement, straightness, and rotation error of a machine carriage. For instance, a 3-axis machine tool or CMM has a total of 21 error parameters needed to be identified. Six parameters for each axis and three parameters for the squareness between axes.

In this group the error parameters are identified by direct measurement. Normally the laser interferometers and straight edge are used as the external measurement device. The main advantage in applying direct measurement methods is that well established methods are employed. The disadvantages are: first, the need to maintain many different and expensive standards or instruments; second, when compared to other methods, the close attention to be paid to sign conventions of error functions as well as the need for a skilled operator. Another disadvantage is that this method is very time consuming; to finish the complete measurement of error parameters on a 3-axis machine might take as long as a week. To overcome these disadvantages a new measurement instrument was

introduced by Ziegert and Mize [5] to accomplish the parametric error measurement of machine tools in hours rather in days. They used a Laser Ball Bar (LBB) to measure the coordinates of a number of points lying along the three sets of mutually perpendicular lines nominally aligned with the three machine axes, in the working volume of a machine tool. The coordinates of these points, as determined by LBB, are used to determine the parametric errors of the three axes of the machine tool. Kulkarni [6] compared the traditional measurement method and the LBB method on a White Sunstrand Series 20 milling machine. The LBB measurements were found to agree with the conventional method.

The parametric errors of a machine will vary under different thermal state. Thus the parametric errors have to be measured in different thermal states. Because of the difficulty in linking the thermal state of the machine to an error function, only a few machine tools have taken full advantage of the software compensation technique. Donmenz [7] implemented a software compensation system on a two-axis turning center to modify the commands generated by the machine controller. In his work the thermal effect was also considered as an error source.

In contrast, the software compensation technique has been widely applied on the CMM. Since the CMM typically functions in a tightly controlled thermal environment, it has less thermal variance than the machine tool. Therefore, the error function is easier to establish.

Group 2: Simultaneously Identified Using External Calibrated Standards

For machines in the second group the error parameters are identified by using a best fit technique. For instance, the calibration of a serial robot is in this group. A typical

robot model locates the link coordinate origins and defines transformations between neighboring links using four-parameter Denavit-Hartenberg (DH) representation. In some cases the DH representation is not sufficient to model the kinematic geometry; for instance, the DH representation is not designed to represent a small misalignment in two consecutive parallel axes. A different modeling approach is proposed in work by Mooring [8]. This model is based on a set of screw theory equations which is sometimes referred to as Rodrigues' equations.

Craig [9] demonstrated the use of the DH technique for modeling a serial link manipulator. The procedure consists of assigning a coordinate system to each link at the joint axis and then expressing the relationship between consecutive coordinate systems with homogeneous transformation matrices. All the individual link transformation matrices may then be multiplied together to produce one transformation relating the coordinate system in the end effector to the base coordinate frame. This procedure is called forward kinematic modeling.

In contrast, given a desired end-effector position and orientation to find the associated joint angle or displacement is called inverse kinematic modeling. To drive a robot to a desired position, the inverse kinematic model has to be used to find the corresponding joint movement. If there is any error in the assumed kinematic parameters, the calculated joint angles or displacements will not drive the end-effector to the desired position. Therefore, an external spatial coordinate measurement device is usually used during a robot kinematic calibration to measure the actual end-effector position. This device may be a precise CMM or a laser tracking system. A detailed description of these

measurement devices is provided by Mooring et al. [10]. When the actual end-effector position is measured by external devices, one can form a residual equation as follows:

$$e_j = P_{act,j} - f(q_j, k) \quad j=1, 2, \dots, m \quad (2-2)$$

where $P_{act,j}$ is the measured end-effector position of the robot at pose j . q_j is the joint readings at pose j . k is the set of kinematic parameters needed to be identified.

Therefore, a least-squares method can be applied to estimate the value of k that minimizes the function

$$L = \sum_{j=1}^m e_j^T e_j \quad (2-3)$$

The selection of the measurement configuration during robot calibration, then, plays an important role in determining the accuracy and speed of convergence of the least-squares identification algorithms. The kinematic parameter errors are not equally observable. The visibility of each unknown parameter varies from one robot to another. There may even be configurations in which some of the kinematic parameters are not observable at all. When the unmodeled error sources and measurement error exist, it becomes impossible to obtain the exact value of k . In minimizing the effect of the inevitable noise on the results of the estimation, the selection of robot measurement configurations may become important. In other words, we have to search for the optimal robot measurement configurations which are least sensitive to the measurement noise and will obtain the best estimation results. Driels and Pathre [11] investigated the factors that will affect the calibration results. The factors include number of measurements, the range of motion of the joints during observations, the encoder resolution and uncertainty, and the selection of configurations. In their calibration experiment simulations the *condition*

number is used to be an indicator of the observability of the parameters to be identified. Zhuang, Wang and Roth [12] adopted a simulated annealing (SA) approach to obtain optimal or near optimal measurement configurations for robot calibration. Zhuang, Wu and Huang [13] developed another selection algorithm called “genetic algorithm” for optimal measurement configurations. In both of the two algorithms the objective is to select the optimal configurations that minimize the condition number. Borm and Meng [14] developed another index called the *observability index* for optimal pose selection. Based on this index, the optimal measurement configurations for kinematic model calibration are determined for PUMA type serial robots. Nahvi and Hollerbach [15, 16] proposed two new indices: *minimum singular value* and *noise amplification index* that are used for the optimal configuration selections. They claim that the noise amplification index is more sensitive to calibration error than the published observability indices.

The last step on the robot calibration is to correct the parameter errors in the kinematic model. Because the accuracy requirement of robots is much less than the machine tool or CMM and the thermal effect is usually ignored, robot error compensation is much easier to accomplish than machine tool or CMM calibration.

Group 3: Self-Calibration

Because the kinematic calibrations of groups 1 and 2 require an accurate external measurement device, an experienced operator, and a large measurement time (between 30 and 60 hours), more and more researchers are seeking new methods of calibration that are less costly and less time consuming. The self-calibration technique, then, is starting to be used in some machines.

The idea of the self-calibration in CMM is using a stable artifact such as a ball plate or ball array. During the calibration the CMM measure the 3-D position of balls fixed on the plate for different locations of the ball plate within the measuring volume of the CMM. These measurements of the ball plate in different work space locations are compared with an off-line computer and kinematic parameters are identified by using the least-square algorithm that minimizes the measurement differences observed in various locations throughout the work space.

The requirement for the artifact is that it has to be very stable. However, the dimensions of the artifact need not to be known accurately. The advantage is that the self-calibration can easily be carried out by non-specialist CMM users with a minimum setup time. Meanwhile, the machine can easily be re-calibrated after a period of operation or maintenance service and the machine error in the whole working volume can be determined.

Kruth, Vanherck and Jonge [17] performed the self-calibration technique by using a ball plate on a Mitutoyo FN905 CMM. The results of the evaluation show that the systematic geometrical errors are greatly reduced. Zhang and Zang [18] used a 1-D ball array to identify the 21 parameters of a 3-D CMM. Belforte et al. [19] used a ball frame to identify and correct the parametric errors on nine CMM machines. They proved that the self-calibration technique can improve the machine performance by a factor ranging between three and ten. The total hours required for these calibration procedures range from 10 to 30 hours which is much less than the direct measurement method. Pahk and Burdekin [20] presented a new parameter identification scheme that uses the stylus of the CMM to measure a horizontal plane and obtain a locus of the stylus. They then identified

the error parameters by minimizing the data deviation from a mean plane. A comprehensive comparison between the direct method and self-calibration technique for machine tools and CMMs is addressed by Sartori and Zhang [21].

In contrast, the self-calibration procedure in robots is much simpler than the CMM. The idea of the open-loop robot self-calibration is to form a closed kinematic chain by interacting with the environment. In other words, no precise artifact is needed in the robot self-calibration. Bennett and Hollerbach [22] investigate the self-calibration of a 6-DOF manipulator grasping a door with a hinge joint. They show that without any external measurement device by only using joint angle reading and self-motions, consistency conditions can be utilized to identify the kinematic parameters. Khoshzaban and Sassani [23] calibrated a teleoperated excavator with unsensed joints by adding an additional linkage (called a calibrator by the authors) with some sensed joints to form a closed loop. Zhuang [24] shows that the closed loop did not need to involve physical linkages, but could be formed by optical paths as virtual limbs to a stereo camera system. He demonstrated that an uncalibrated stereo camera system could be simultaneously calibrated with an uncalibrated manipulator.

2.2 Closed-Loop (Parallel Mechanism) Kinematic Calibration

The majority of today's industrial machines are serial chains (or open-loop) mechanism. Cartesian type machine tools have been developed and used for nearly 200 years. The CMM and industrial robot calibration techniques also have many decades of practical experience behind them. The techniques for manufacturing and calibrating these machines have become very well understood and mature. However, maintaining

these cantilevered machines to be very stiff and accurate is very difficult and expensive. In addition, most the machines only provide single mode functionality. To make a part that requires milling, cutting, welding and other processes will require many different types of machines. In contrast, the parallel (or closed loop) structures offer the benefits of multiple functionality in a single machine, increased stiffness of the mechanism, low weight, and low effective inertia of moving components. A performance comparison between serial and parallel link manipulators has been addressed by El-Khasawneh and Ferreira [25]. These advantages of the parallel type machines offer the potential for better performance than the conventional machines. As a consequence, parallel link manipulator concepts are increasingly being used in the development of a new generation of advanced machine tool.

A typical parallel type machine is the hexapod machine. The earliest known hexapod machine was the tire tester designed by Gough in 1949. However, this structure is widely regarded as the Stewart Platform since Stewart [26] popularized it through its use as a flight simulator. Many unsuccessful attempts were made between 1970 and 1990 to make practical machines. The cost of computing strut lengths has until recently been too high for most applications. Now that the cost of computing has fallen dramatically, many companies are offering hexapod based machines, such as Ingersoll, Gidding & Lewis, Hexel, Geodetics, ITIA and Polytec PI.

Group 4: Simultaneously Identified Using External Calibrated Standards

Since the special demand for using Stewart platform as a machining center was only recently addressed, many of its characteristics are still developing. Although the Stewart platform has many advantages, the disadvantages include a complex work space,

a small orientation range and low structural damping. Because of the complex structure, it is necessary to analyze the contribution of each individual error source to the overall machine accuracy. Before doing this, one has to model the forward and inverse kinematics. Given a set of leg lengths to determine the platform position and orientation is the forward kinematics problem. This problem could lead to multiple solutions.

Merlet [27] developed an algorithm to solve the Stewart platform forward kinematic problem, in which he found that the upper bound on number of solutions is 1320.

Raghavan [28] found that a general Stewart Platform has 40 real solutions. However, Wang and Masory [29] presented a numerical method for solving the forward and inverse kinematics and analyzed the effect of the manufacturing tolerance, installation errors and link offsets on the platform accuracy. Wang, Masory and Zhuang [30] also established a calibration algorithm based on the error model derived by forward kinematics.

Unlike the forward kinematics problem, the inverse kinematics problem is easy to solve, and is defined as, "Given the platform position and orientation, compute the manipulator leg lengths." Because of the difficulty in the forward kinematic modeling, many researchers used the inverse kinematics to find the error sources and how the error sources affect on the accuracy of the parallel machines. According to the analysis of Ropponen and Arai [31] and Patel and Ehmann [32], the error model of a Stewart platform based machine may be expressed as

$$\delta\Lambda = J\delta\Pi + N\delta A \quad (2-4)$$

where $\delta\Lambda$ is the leg length errors. $\delta\Pi$ is the platform position and orientation errors. δA is the joint position errors. J is the Jacobian matrix of the Stewart platform. N is a transformation matrix mapping the joint error to leg length error. Patel and Ehmann

completed an automated error analysis software called SPAEA (Stewart Platform Automated Error Analysis) for platform accuracy analysis. Assuming the error components are given, a platform position and orientation accuracy analysis can be performed using the nominal parameters in the SPAEA. The idea is to invert Equation 2-4 and obtain the platform error function

$$\delta\boldsymbol{\Pi} = \boldsymbol{J}^{-1} (\delta\boldsymbol{\Lambda} - \boldsymbol{N}\delta\boldsymbol{A}) \quad (2-5)$$

The same error model as shown in Equation 2-4 also has been developed by Soons [33] about the same time as Patel and Ehmann. He also used the inverse kinematics idea but he derived the error functions more concisely than Patel and Ehmann.

Another calibration technique was suggested by Zhuang and Roth [34] who proposed an idea: by fixing one leg at a time and moving the other five legs during measurement process, one is able to compute kinematic parameters one leg at a time. This approach requires relatively little computation. However, the identified parameters may not be optimal because: (1) The measurable workspace is small because of the restricted motion pattern of the manipulator; (2) Kinematic parameters of individual links are computed separately, therefore, the coupling effects among the legs are not fully explored; and (3) The model used did not include all the kinematic parameters of the platform because they assumed the joints were perfect.

Once the error model has been completed, the next step for kinematic calibration is the measurement. An external measurement device has to be used for performing this task. This device measures the position and orientation errors of the platform shown in Equation 2-5. Soons [35] developed a computer-aided experimental design technique for the configuration selection that improves the condition of error parameter identification.

Since the observed errors are the linear combination of the error components that are shown in Equation 2-5, the least-squares method is used to identify the error parameters simultaneously.

In addition to the hexapod machine, Maurine and Dombre [36] presented a calibration procedure for a 4-DOF parallel robot. They used an inexpensive laser displacement sensor installed on the robot platform to measure an external grid pattern and several cylinders placed in a circle on a work table. They compared the errors between the values calculated from kinematic model and the values from measurement. The least-squares method then was used for identifying the error parameters. Wallack and Mazon [37] used a calibration peg and multiple crossbeam sensors on a 4-DOF robot to identify the rotation axis and translation axis.

Group 5: Self-Calibration

As we mentioned earlier, when the kinematic calibration needs an external measurement device, this process will require experienced operators and be very time consuming. Thus, the self-calibration techniques are an attractive alternative. This technique just needs some redundant sensors or kinematic constraints and moving the machine to different configurations, then the error parameters can be identified. Though the self-calibration can be simply performed, only a few papers have been published at this time.

Zhuang and Liu [38] installed several redundant sensors on the U-joints of a Stewart platform based machine, and identified the 30 error parameters. The idea is to adjust the nominal values to minimize the difference between the measured values from redundant sensors and the calculated values from the forward and inverse kinematic

models. Nahvi, Hollerbach and Hayward [15] presented an autonomous kinematic calibration method for a 3-DOF shoulder joint parallel robot. They used the features of the redundant kinematics that form multiple closed loops, thus, adding up all vector components in each closed loop should yield a zero vector. If the nominal parameters are incorrect, however, the closed loop vector summation will yield a residual error vector. The kinematic parameters, then, are identified by minimizing the residual vectors. They applied the smallest singular value along with the condition number of the identification Jacobian as the pose selection strategy that yields a maximum observability of the parameters. Hollerbach and Lokhorst [39] used the same idea in [15] and presented experimental results on the parameter identification of a RSI 6-DOF hand controller, a two-loop parallel mechanism comprised of three 6-DOF arms with potentiometers on the first joint of each arm.

2.3 Conclusion

Based on the above review, if the self-calibration technique is not adopted, then expensive special instrumentation is required to perform the parameter identification for the HCMM. Even if the instrumentation is available, specially trained technicians are needed to make the measurements. Large data collection times are required to measure the parametric errors of machines. The cost and difficulty of the external-artifact based method prevents them from being used to re-calibrate frequently. In contrast, the self-calibration technique is less expensive, faster, and easier to operate. It allows the machine to be re-calibrated more frequently. Hence, it would be a better alternative to identify the parametric errors of the HCMM by a self-calibration technique.

CHAPTER 3

MODELING, MEASUREMENT AND IDENTIFICATION

As mentioned earlier, the laser interferometric displacement measurement system is installed in each of the six struts and measures the length changes of each strut. However, in order to calculate the coordinates of the probe of the HCMM, it is necessary to know the absolute length of each strut and the distance between the three base spheres. The nominal lengths could be obtained by using a conventional linear measurement device such as a scale. However, to find the kinematic parameter values with sufficient accuracy, a calibration procedure is necessary.

The process of kinematic calibration consists of the modeling, measurement, and identification steps. Modeling refers to the choice of a functional relationship between the kinematic parameters and the resulting poses of the center rod of the HCMM. The model selected should account for all the factors considered to be significant in contributing to HCMM accuracy.

Physical data are then collected from moving the center rod into different poses. This data set contains information relating the input of the model (the reading of strut displacements) to the output of the model (the center rod length).

The mathematical process of using the data collected to identify the parameters of the model is the third step in calibration. It is important to make the identification process fast and accurate. In this chapter we will describe these three calibration processes.

3.1 Kinematic Modeling

The first step in any calibration procedure is to obtain a valid kinematic model. The purpose is to relate the outputs of joint displacement to the manipulator pose. There are two basic forms that any kinematic model may take. The forward model computes the manipulator pose from the given joint displacement readings. The inverse model, on the other hand, is used to find the set of joint displacements when a manipulator pose is given. When we formulate the kinematic model of the HCMM, the following assumptions are made:

1. The spherical joints produce perfect spherical motion and the centers of the reference spheres are their exact rotation centers.
2. No noticeable thermal effect occurs.

The World Coordinate System Assignment

We define a fixed world coordinate system, to which all coordinate-dependent kinematic parameters are referred. In general it can be placed anywhere in space. A principle for placing this coordinate system is not to introduce any redundant kinematic parameters. In this case the origin of the coordinate system is placed on one of the base sphere centers, BS1, as shown in Figure 3-1.

The x axis lies along a line connecting two base sphere centers. The plane passing through the centers of three base spheres is chosen as x-y plane. The z axis is along the normal direction of the x-y plane. The BS2 has coordinate of $(r, 0, 0)$ and BS3 is located at $(b, h, 0)$. Therefore, in this coordinate system setup, a total of nine parameters are required to determine the coordinates of the upper and lower sphere centers, P_{up} and P_{low} .

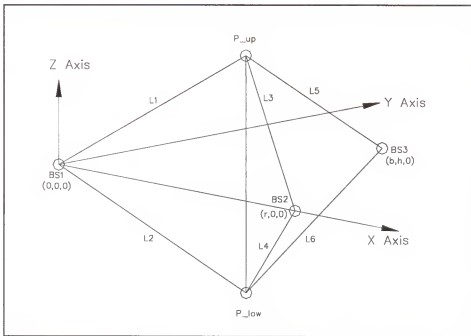


Figure 3-1 The HCMM coordinate system

Forward Kinematic Model

The constant center rod length provides the kinematic chain which constrains the motion of the apexes of the two tetrahedrons. Its length is defined as the distance between the two sphere centers. If the locations of the three base spheres and the absolute length of each strut are given, the unique position and orientation of the center rod can be determined.

Because of the telescoping strut design, each of the six struts may change its length to satisfy the kinematic constraint when the center rod is moved from one position to the other. We define the “length change” as the length difference between the initial and the current configuration. For the i th configuration, the strut length is the sum of the

initial (or starting) length and its length change at the current configuration. Let's say the k th strut, with its initial length of $a(k)$, has a length change of $S(k, i)$ at the i th configuration. At this instance its absolute length is expressed as:

$$\begin{aligned} l(k, i) &= a(k) + S(k, i) \\ \text{where} \\ k &= 1, \dots, 6 \\ i &= 1, \dots, m \end{aligned} \tag{3-1}$$

From the above expression it is noted that the initial length of $a(k)$ is a constant value and the length change of $S(k, i)$ will vary from configuration to configuration. The centers of the upper and lower spheres, P_{up} and P_{low} , can be obtained from Equations 3-2 to 3-7.

$$X_u(i) = \frac{l^2(1, i) - l^2(3, i) + r^2}{2r} \tag{3-2}$$

$$Y_u(i) = \frac{l^2(3, i) - l^2(5, i) + 2X_u(i)[r - b] - [r^2 - b^2 - h^2]}{2h} \tag{3-3}$$

$$Z_u(i) = \sqrt{l^2(1, i) - X_u^2(i) - Y_u^2(i)} \tag{3-4}$$

$$X_l(i) = \frac{l^2(2, i) - l^2(4, i) + r^2}{2r} \tag{3-5}$$

$$Y_l(i) = \frac{l^2(4, i) - l^2(6, i) + 2X_l(i)[r - b] - [r^2 - b^2 - h^2]}{2h} \tag{3-6}$$

$$Z_l(i) = -\sqrt{l^2(2, i) - X_l^2(i) - Y_l^2(i)} \tag{3-7}$$

Therefore, the center rod length can be calculated as:

$$L_c = \sqrt{[X_u(i) - X_l(i)]^2 + [Y_u(i) - Y_l(i)]^2 + [Z_u(i) - Z_l(i)]^2} \tag{3-8}$$

Inverse Kinematic Model

In the forward kinematic model the strut displacements are treated as inputs. The HCMM controller, on the other hand, may receive a desired center rod pose as the input and must compute the joint displacements necessary to achieve this pose. In other words, the inverse kinematic model is required for use in the controller.

Because of the simple geometry of our machine, the inverse model can be easily obtained as the following,

$$S(1) = \sqrt{X_u^2 + Y_u^2 + Z_u^2} - a(1) \quad (3-9)$$

$$S(2) = \sqrt{X_l^2 + Y_l^2 + Z_l^2} - a(2) \quad (3-10)$$

$$S(3) = \sqrt{(X_u - r)^2 + Y_u^2 + Z_u^2} - a(3) \quad (3-11)$$

$$S(4) = \sqrt{(X_l - r)^2 + Y_l^2 + Z_l^2} - a(4) \quad (3-12)$$

$$S(5) = \sqrt{(X_u - b)^2 + (Y_u - h)^2 + Z_u^2} - a(5) \quad (3-13)$$

$$S(6) = \sqrt{(X_l - b)^2 + (Y_l - h)^2 + Z_l^2} - a(6) \quad (3-14)$$

3.2 Measurement

The fixed length center rod and the closed loop kinematics of the HCMM provide a very useful feature in the calibration procedure. Unlike the conventional calibration technique, one can use the kinematic constraints and the displacement reading of each of the struts to perform the kinematic calibration. Therefore, this calibration procedure is called “self-calibration” since no external measurement device is required.

For the calibration of a conventional CMM, the measurement process is time consuming, laborious, and prone to human error. In contrast, the measurement process for HCMM is simply moving the center rod to a number of different positions within its work volume, and recording the displacement reading in each strut. Thus one can collect data very easily. However, it is necessary to minimize the number of measurement, because we assume that there is no thermal effect during the calibration process. Taking too many measurements could create more heat released by the actuator and cause significant thermal deformation in the structure.

We will show that the self-calibration process is very sensitive to the level of measurement noise. The measurement noise may include the modeling imperfection or measurement error from the laser interferometer. To eliminate or minimize the effect owing to measurement noise, then, becomes one of the most difficult problems in the parameter identification. In fact, it is impossible to include every possible error source in a kinematic model or to completely eliminate the measurement error. When the unmodeled error sources and measurement error exist, it becomes impossible to obtain the exact values of the parameters used in the model. In general, the magnitude of the noise itself is quite small, but its effect on the estimation accuracy may be rather significant. To minimize the effects of the inevitable noise on the results of estimation, the selection of measurement configurations may become important. The selection of the optimal measurement configuration for calibration will be discussed in a later chapter.

Error Sources

As we have mentioned the self-calibration method is very sensitive to the measurement noise (or error), it is necessary to realize and analyze the error sources and

to reduce their magnitude during the design and manufacturing stages. The error sources could be (1) the displacement measurement error of the laser interferometer (2) the imperfections of the spherical joint and the spheres (3) the thermal deformation of the structure. A detailed description on the error sources will be discussed in Chapter 7.

3.3 Identification

The mathematical process of using the data collected to identify the parameters of the model is the third step in the calibration. Because of the incorrect nominal values, measurement noise and modeling error, the calculated center rod length from the model would not have the same value at each pose. If the true center rod length, Lc_{true} , could be obtained, the residual equation of the center rod could be presented by Equation 3-15.

$$\delta Lc_i = Lc_{true} - \hat{Lc}_i \quad (3-15)$$

where \hat{Lc}_i is the predicted center rod length calculated by the model at the i th configuration. Thus the kinematic parameters can be obtained by adjusting their values to minimize the residual of the center rod length. However, in order to implement this scheme it is necessary to know the true center rod length, or at least the length that is precise enough for the calibration purposes. It will be a difficult problem to find a measurement device and technique that can be performed quickly and easily to give us a sufficiently accurate value for the center rod length.

Another identification algorithm to substitute Equation 3-15 can be written as follows:

$$\delta Lc_{ij} = \hat{Lc}_i - \hat{Lc}_j \quad (3-16)$$

The \hat{Lc}_i and \hat{Lc}_j are the calculated center rod lengths in i th and j th configurations respectively. We call the δLc_{ij} the *relative residual* of the center rod length. Using Equations 3-1 to 3-8, the relative residual may be rewritten as

$$\delta Lc_{ij} = f(\underline{a}, r, b, h, \underline{S}_i) - f(\underline{a}, r, b, h, \underline{S}_j) \quad (3-17)$$

where \underline{S}_i is a set of strut displacements associated with configuration i . Equation 3-17 is a feasible algorithm, but to perform the mathematical identification would be very computationally intensive. For instance by taking m configurations, will generate

$\frac{m \times (m - 1)}{2}$ relative residual equations which is 1225 for $m = 50$. To solve such large

residual equation would require long computation times. Therefore, a modified algorithm called *reference residual* is used in the HCMM calibration procedure. It is represented as follows:

$$e_i = Lc_r^2 - \hat{Lc}_i^2 \quad (3-18)$$

where Lc_r is an assigned value which is an approximate guess. It is not necessary for this value to be known exactly and it will be treated as the tenth kinematic parameter which needs to be identified. The objective is then to find a set of parameters including the Lc_r to minimize the reference residual, e_i .

Least-Squares Method

Our goal is to find the optimal parameters that minimize the reference residual. There are many optimization techniques one can use. One technique is to find a set of parameters that minimize the sum of the absolute reference residual which is expressed in Equation 3-18.

$$\text{Minimize} \sum_{i=1}^m |e_i| \quad (3-19)$$

A gradient search may be used for finding the unknown parameters. But this method is not popular because it is computationally demanding and mathematically intractable. On the other hand, from our literature review, the least-squares method was seen as the most popular. It has two big advantages. First, large errors are heavily penalized. The other advantage is mathematical tractability. The formula giving the least-squares estimates is obtained by quite simple matrix algebra, and the estimates are computed as the solution to a set of linear equations. Moreover, the properties of the estimates are relatively easy to analyze. The least-squares method can be expressed as

$$\text{Minimize} \sum_{i=1}^m e_i^2 \quad (3-20)$$

Linearized Least-Squares Method (Gauss-Newton's Method)

Since Equation 3-18 is highly non-linear, one method to solve it is to linearize this equation. At the i th configuration of HCMM, by using the Taylor expansion, Equation 3-21 can be written as

$$\begin{aligned} e_i &= e_i \Big|_{A_0} + \frac{\partial e_i}{\partial a_1} \Big|_{A_0} \Delta a_1 + \cdots + \frac{\partial e_i}{\partial a_6} \Big|_{A_0} \Delta a_6 + \frac{\partial e_i}{\partial r} \Big|_{A_0} \Delta r + \frac{\partial e_i}{\partial b} \Big|_{A_0} \Delta b \\ &\quad + \frac{\partial e_i}{\partial h} \Big|_{A_0} \Delta h + \frac{\partial e_i}{\partial Lc_r} \Big|_{A_0} \Delta Lc_r + \text{higher order terms} \end{aligned} \quad (3-21)$$

where vector A_0 is the nominal value for parameters $\{a_1, \dots, a_6, r, b, h, Lc_r\}^T$.

Suppose that the center rod is placed into m poses, this provides a vector of e which is written as

$$\begin{pmatrix} e_1 \\ e_2 \\ \vdots \\ e_m \end{pmatrix}_{|A_0} = \begin{pmatrix} e_1 \\ e_2 \\ \vdots \\ e_m \end{pmatrix} + \begin{bmatrix} \frac{\partial e_1}{\partial a_1} & \dots & \frac{\partial e_1}{\partial r} & \frac{\partial e_1}{\partial b} & \frac{\partial e_1}{\partial h} & \frac{\partial e_1}{\partial Lc_r} \\ \vdots & & \vdots & \vdots & \vdots & \vdots \\ \vdots & & \vdots & \vdots & \vdots & \vdots \\ \frac{\partial e_m}{\partial a_1} & \dots & \frac{\partial e_m}{\partial r} & \frac{\partial e_m}{\partial b} & \frac{\partial e_m}{\partial h} & \frac{\partial e_m}{\partial Lc_r} \end{bmatrix}_{|A_0} \begin{pmatrix} \Delta a_1 \\ \vdots \\ \Delta a_6 \\ \Delta r \\ \Delta b \\ \Delta h \\ \Delta Lc_r \end{pmatrix} \\ + \text{higher order terms} \quad (3-22)$$

or

$$E = E_o + J\Delta A + \text{higher order terms} \quad (3-23)$$

$$\text{where } J = \begin{bmatrix} \frac{\partial e_1}{\partial a_1} & \dots & \frac{\partial e_1}{\partial r} & \frac{\partial e_1}{\partial b} & \frac{\partial e_1}{\partial h} & \frac{\partial e_1}{\partial Lc_r} \\ \vdots & & \vdots & \vdots & \vdots & \vdots \\ \vdots & & \vdots & \vdots & \vdots & \vdots \\ \frac{\partial e_m}{\partial a_1} & \dots & \frac{\partial e_m}{\partial r} & \frac{\partial e_m}{\partial b} & \frac{\partial e_m}{\partial h} & \frac{\partial e_m}{\partial Lc_r} \end{bmatrix}_{|A_0} \quad \Delta A = \begin{pmatrix} \Delta a_1 \\ \vdots \\ \Delta a_6 \\ \Delta r \\ \Delta b \\ \Delta h \\ \Delta Lc_r \end{pmatrix}$$

The values of E_o and J are evaluated at A_o . The J matrix is referred as the Jacobian matrix. If the nominal values of A_o are close enough to the true values, the higher order terms in Equation 3-23 then can be ignored. In this case the reference residual can be written as

$$E = E_o + J\Delta A \quad (3-24)$$

Therefore, the objective function of Equation 3-20 can be rewritten as

$$\text{Minimize } f = (E_o + J\Delta A)^T (E_o + J\Delta A) \quad (3-25)$$

This performance criterion is quadratic in the elements of ΔA . The minimum value of f is obtained when

$$\frac{\partial f}{\partial \Delta A} = 0 \quad (3-26)$$

together with the condition that at the value of ΔA that satisfies Equation 3-26, the

Hessian matrix of f is positive semidefinite:

$$\frac{\partial^2 f}{\partial \Delta A^2} \geq 0 \quad (3-27)$$

To differentiate f , the following matrix derivation formulas are used:

$$\frac{\partial}{\partial \underline{a}} (\underline{a}^T H \underline{e}) = H \underline{e} \quad (3-28)$$

$$\frac{\partial}{\partial \underline{a}} (\underline{e}^T H \underline{a}) = H^T \underline{e} \quad (3-29)$$

$$\frac{\partial}{\partial \underline{a}} (\underline{a}^T H \underline{a}) = (H + H^T) \underline{a} \quad (3-30)$$

where H is any square matrix and \underline{a} and \underline{e} are vectors.

Differentiating Equation 3-25 and substituting into the condition given in Equation 3-26 yields

$$\frac{\partial f}{\partial \Delta A} = -2J^T E_o + (J^T J + J^T J)\Delta A = 0 \quad (3-31)$$

which yields

$$\Delta A = (J^T J)^{-1} J^T E_o \quad (3-32)$$

During each iteration the guess parameter is updated as

$$A_{new} = A_{old} + \Delta A \quad (3-33)$$

This procedure is iterated until the largest value in vector A is less than the desired tolerance. This method also is referred to as the “*Gauss-Newton*” method or the *iterative linear least-squares* method. The flow chart of linearized least-squares method is shown in Figure 3-2.

Gradient Method

Without linearizing the non-linear least-square equation, there are still several optimization methods which can be used. One may try the gradient method. The iterative technique is used for finding the optimal parameters. Let \underline{a}_j denote the estimate of the optimal solution at the beginning of j th iteration. The j th iteration consists of the computation of a search vector \underline{p}_j from which the new estimate \underline{a}_{j+1} is obtained according to

$$\underline{a}_{j+1} = \underline{a}_j + \alpha_j \underline{p}_j \quad (3-34)$$

If the value of \underline{p}_j equals to the negative of the gradient of the objective in j th iteration, this is called the *steepest descent direction*. In general the choice of vector \underline{p}_j is not necessary to along the direction of steepest decent. According Newton's method the search vector \underline{p}_j is chosen by

$$\underline{p}_j = H_j^{-1} \underline{g}_j \quad (3-35)$$

where H_j and \underline{g}_j are the Hessian matrix and gradient of the objective function in j th iteration. They can be expressed in matrix form as

$$\underline{g}_j = -2J^T \underline{e}_j \quad (3-36)$$

$$H_j = 2J_j^T J_j + 2Q_j \quad (3-37)$$

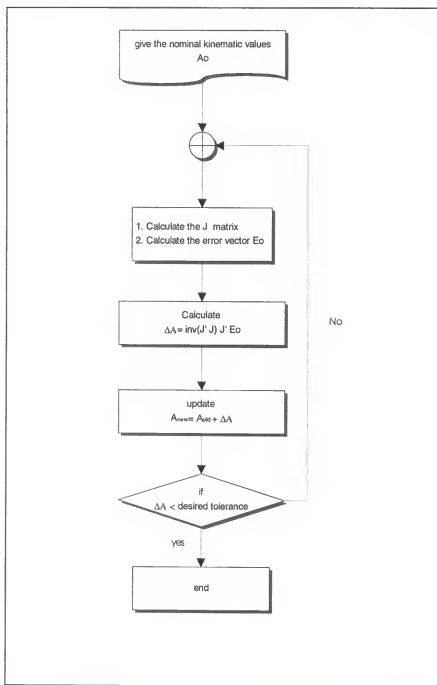


Figure 3-2 Flow chart for linearized least-squares method

where J is the Jacobian matrix in j th iteration. e_j is the objective evaluated at $\underline{a} = \underline{a}_j$. Q_j is the value of

$$Q_j = \sum_{i=1}^m e_i (\nabla^2 [e_i]) \quad (3-38)$$

Substituting Equation 3-36 and 3-37 into Equation 3-35 we obtain

$$p_j = (J_j^T J_j + Q_j)^{-1} J_j^T e_j \quad (3-39)$$

In Equation 3-34 if the estimate parameter is close to the true values, the Q_j is small enough to be ignored. Also assuming the $\alpha_j = 1$, then the identification algorithm reduces to the linearized least-squares method or the Gauss-Newton method.

Levenberg-Marquardt (LM) Method

The Gauss-Newton algorithm breaks down at the singularities of the identification Jacobian and converges very slowly near such singularities. Therefore, the LM method is introduced as an improvement to the Gauss-Newton method. The technique is designed to overcome problems related to singularity of the matrix $J^T J$. The idea is to modify Equation 3-39 by adding a time varying nonnegative scalar coefficient, μ_j , as follows:

$$p_j = (J_j^T J_j + \mu_j I)^{-1} J_j^T e_j \quad (3-40)$$

where I is an identity matrix.

The value μ_j is initially set to some positive value (say, $\mu_j = 0.01$). At the beginning of each iteration, μ_j , is reduced by a factor of k (say, $k = 10$) in attempt to push the algorithm closer to the Gauss-Newton method. If, for the chosen value of μ_j , no reduction in the objective function is achieved, the value of μ_j is increased by the factor k . For more detailed description for selection of μ_j and k is provided by Scales [40].

3.4 Conclusion

In this chapter we developed a self-calibration algorithm that is feasible for the identification of the HCMM parameters. The idea for the self-calibration is to introduce a kinematic constraint so that the HCMM can be calibrated without adopting any external measurement device. The center rod length can be treated as a new parameter and its value is not necessary known. The optimal kinematic parameter values can be obtained by applying the least-squares method to reduce the reference residual of the center rod.

CHAPTER 4 MEASUREMENT STRATEGY

The most notable feature of a self-calibration technique is that no external measurement device is needed. By moving the center rod into a number of poses and recording the displacement data of each strut, one can determine the kinematic parameters of the mechanism. However, this self-calibration technique is very sensitive to the level of measurement noise. If the measurement noise is too big, the calibration results may be very poor.

The measurement noise may include the modeling imperfection or measurement error from the laser interferometer. To eliminate or minimize the effect owing to measurement noise, then, becomes one of the most difficult problems in the parameter identification. In fact, it is impossible to include every possible error source in a kinematic model or to completely eliminate the measurement error. When the unmodeled error sources and measurement exist, it becomes impossible to obtain the exact values of the parameters used in the model. In general, the magnitude of the noise itself is quite small, but its effect on the estimation accuracy may be rather significant. For example, in some HCMM configuration, center rod length errors are so insensitive to the error parameters that the unmodeled error sources become the main causes of the center rod length error. When the center rod length error calculated from these configurations, the estimation result will obviously be poor. We want the effect of measurement error and unmodeled errors to be less significant to the determination of error parameters,

consequently a better estimation of parameters will be expected. Therefore, to minimize the effects of the inevitable noise on the results of estimation, the selection of measurement configurations becomes very important.

Many researchers have proposed a variety of observability indices to quantify the goodness of pose selection. These indices are based on the singular value decomposition (SVD) of Jacobian matrix of the differential kinematics. These indices are (1) condition number (2) observation index (3) smallest singular value (4) noise amplification index. Since the condition number is the most widely used index for configuration selection, we choose the condition number as the index to quantify the goodness of pose selection. The following section will show how the condition number is derived. For more information on the other observability indices, one can obtain it from Appendix A.

Condition Number

Before starting any description on the condition number, it is better to introduce the matrix norms and the SVD. An induced matrix norm for square matrix A is defined as

$$\|A\| = \max \left(\frac{\|AX\|}{\|X\|} \quad \text{for } X \neq 0 \right) \quad (4-1)$$

which satisfies all the following conditions that define the norm in general

$$(1) \|A\| \geq 0, \|A\| = 0 \text{ if and only if } A = 0 \quad (4-2)$$

$$(2) \|aA\| = |a|\|A\| \quad (4-3)$$

$$(3) \|A + B\| \leq \|A\| + \|B\| \quad (4-4)$$

$$(4) \|AB\| \leq \|A\|\|B\| \quad (4-5)$$

Depending on which vector norm is used we will see different norm values. For a n -dimension vector \underline{x} with real elements the most common norms are 1-norm, 2-norm, and infinity-norm as follows:

$$\|\underline{x}\|_1 = \sum_{i=1}^n |x_i| \quad (4-6)$$

$$\|\underline{x}\|_2 = \left(\sum_{i=1}^n |x_i|^2 \right)^{\frac{1}{2}} \quad (4-7)$$

$$\|\underline{x}\|_\infty = \max |x_i| \text{ for } 1 \leq i \leq n \quad (4-8)$$

One can show the 1-norm produces the maximum column norm for the induced matrix norm in Equation 4-1. 2-norm gives the largest singular value of A which also is the largest eigenvalue of $A^T A$. The infinity norm yields the maximum row sum. The 1-norm and ∞ -norm can be written as follows:

$$\|A\|_1 = \max \left\{ \sum_{i=1}^n |a_{ij}| \text{ for } 1 \leq j \leq n \right\} \quad (4-9)$$

$$\|A\|_\infty = \max \left\{ \sum_{j=1}^n |a_{ij}| \text{ for } 1 \leq i \leq n \right\} \quad (4-10)$$

Next the SVD will be defined. For a $m \times n$ matrix A with $m \geq n$ (this assumption is made for convenience only; all the results will also hold if $m < n$), there is a singular value decomposition as

$$A = U \Sigma Q^T \quad (4-11)$$

where

$$\Sigma = \begin{pmatrix} \Sigma & 0 \\ 0 & 0 \end{pmatrix}_{m \times n} \quad (4-12)$$

U is a $m \times m$ matrix, Σ is $r \times r$ diagonal matrix whose diagonal entities are non-zero singular values $\sigma_1 \geq \sigma_2 \geq \dots \geq \sigma_r \geq 0$, and Q is $n \times n$ matrix. The U and Q are orthonormal matrices. The columns in U are the left singular vectors of matrix A and the columns in Q are the right singular vectors of A . If A is nonsingular or full rank matrix, then r equals to n . In this case Σ can be expressed as

$$\Sigma = \begin{pmatrix} \sigma_1 & 0 & 0 & \cdots & 0 \\ 0 & \sigma_2 & 0 & \cdots & 0 \\ 0 & 0 & \ddots & \cdots & 0 \\ \vdots & \vdots & \vdots & \ddots & \vdots \\ 0 & 0 & \cdots & \cdots & \sigma_n \\ 0 & 0 & 0 & \cdots & 0 \\ \vdots & \vdots & \vdots & \cdots & \vdots \\ 0 & 0 & 0 & \cdots & 0 \end{pmatrix}_{m \times n} \quad (4-13)$$

More detail about how to derive the SVD can be obtained from Klema and Laub [40] and Leon [41].

After the matrix norm and SVD have been introduced, we start to analyze the numerical sensitivity of the least-squares identification problem. Let A be a nonsingular matrix of order n and consider the system $A\underline{x} = \underline{b}$. The vector \underline{b} corresponds to the measured data and as such is subject to uncertainty. The matrix A is related to the measurement configuration and the system model and also is subject to errors. Thus:

$$\underline{x} + \delta \underline{x} = (A + \delta A)^{-1} (\underline{b} + \delta \underline{b}) \quad (4-14)$$

where the solution error $\delta \underline{x}$ reflects the sensitivity of the identification algorithm to errors in the model and the data characterized in Equation 4-14 as δA and $\delta \underline{b}$.

Assume first that $\delta A = 0$ but $\delta \underline{b} \neq 0$. Then

$$\|\delta \underline{x}\| \leq \|A^{-1}\| \|\delta \underline{b}\| \quad (4-15)$$

Similar to Equation 4-15 one may write

$$\|\underline{b}\| \leq \|A\| \|\underline{x}\| \quad (4-16)$$

Combining Equations 4-15 and 4-16 and assume that $\underline{b} \neq 0$, we find that

$$\frac{\|\delta \underline{x}\|}{\|\underline{x}\|} \leq \|A\| \|A^{-1}\| \frac{\|\delta \underline{b}\|}{\|\underline{b}\|} \quad (4-17)$$

Also from Equation 4-14, assume that $\delta A = 0$. We have

$$\delta \underline{b} = A \delta \underline{x} \quad (4-18)$$

We may write the inequality equation as

$$\|\delta \underline{b}\| \leq \|A\| \|\delta \underline{x}\| \quad (4-19)$$

From the system equation $A \underline{x} = \underline{b}$, we have

$$\|\underline{x}\| \leq \|A^{-1}\| \|\underline{b}\| \quad (4-20)$$

Combining Equation 4-19 and 4-20, we find that

$$\frac{1}{\|A\| \|A^{-1}\|} \frac{\|\delta \underline{b}\|}{\|\underline{b}\|} \leq \frac{\|\delta \underline{x}\|}{\|\underline{x}\|} \quad (4-21)$$

From Equation 4-17 and 4-21, we may write that

$$\frac{1}{\|A\| \|A^{-1}\|} \frac{\|\delta \underline{b}\|}{\|\underline{b}\|} \leq \frac{\|\delta \underline{x}\|}{\|\underline{x}\|} \leq \|A\| \|A^{-1}\| \frac{\|\delta \underline{b}\|}{\|\underline{b}\|} \quad (4-22)$$

The number $\|A\| \|A^{-1}\|$ is called the *condition number* of A and will be denoted by $\text{cond}(A)$. Thus:

$$\frac{1}{\text{cond}(A)} \frac{\|\delta b\|}{\|b\|} \leq \frac{\|\delta x\|}{\|x\|} \leq \text{cond}(A) \frac{\|\delta b\|}{\|b\|} \quad (4-23)$$

The inequality Equation 4-23 related the size of relative error $\frac{\|\delta x\|}{\|x\|}$ to the relative residual $\frac{\|\delta b\|}{\|b\|}$.

If the condition number is close to 1, the relative error and the relative residual will be close in magnitude. If the condition number is large, the relative error could be many times as large as the relative residual. The condition number depends on the particular vector norm that is used. For example, for the 2-norm we find that $\text{cond}(A)$ is simply the largest singular value of A divided by the smallest singular value of A where matrix A is not necessarily a square matrix. The proof can be obtained from Leon [42].

Assuming next that $\delta A \neq 0$ but $\delta b = 0$ in Equation 4-14, one gets

$$x + \delta x = (A + \delta A)^{-1} b \quad (4-24)$$

Substitute $x = A^{-1}b$ into Equation 4-24 and rearrange the equation, one obtains

$$\delta x = ((A + \delta A)^{-1} - A^{-1})b \quad (4-25)$$

Use the matrix identity

$$B^{-1} - A^{-1} = A^{-1}(A - B)B^{-1} \quad (4-26)$$

One gets

$$\delta x = A^{-1}\delta A(A + \delta A)^{-1}b \quad (4-27)$$

which equals

$$\delta x = A^{-1}\delta A(x + \delta x) \quad (4-28)$$

Thus, we have

$$\|\delta \underline{x}\| \leq \|A^{-1}\| \|\delta A\| \|\underline{x} + \delta \underline{x}\| \quad (4-29)$$

or

$$\frac{\|\delta \underline{x}\|}{\|\underline{x} + \delta \underline{x}\|} \leq \|A\| \|A^{-1}\| \frac{\|\delta A\|}{\|A\|} \quad (4-30)$$

Similar to Equation 4-17 estimate error $\delta \underline{x}$ is bounded by the matrix error ratio $\|\delta A\| / \|A\|$ multiplied by the condition number. Therefore, the condition number provides the upper boundary of the estimation error in relation to the matrix error induced by the parameter errors and measurement noise.

Most the least-squares problems are overdetermined problems which means that the matrix is not a square matrix but a rectangular matrix. The condition number still is applicable for this case. One can treat the matrix inverse of A as a Pseudoinverse matrix which is $A^+ = Q\Sigma^+U^T$ so that the condition number derivation process from Equation 4-14 to 4-30 is still valid.

CHAPTER 5 CALIBRATION SIMULATION

In the previous chapter we introduced three important calibration steps which give us the basic calibration concept. We also presented the observation indices that provide us a reference for choosing proper HCMM poses. After outlining these fundamentals, several questions then are raised: How best to select measurement configurations or what is the best measurement strategy? How many poses do we need to reach the desired accuracy? What is the effect of measurement accuracy and noise? Will the quality of the initial estimate of parameters be a factor in calibration accuracy? In order to obtain these answers a series of computer-based mathematical simulations have been performed. A simplified HCMM model is shown in Figure 5-1. Ten kinematic parameters which determine the initial configuration are shown in Table 5-1. The maximum and minimum strut length are 52 and 32 inches, respectively.

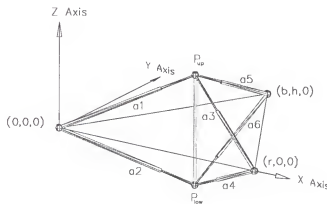


Figure 5-1 The HCMM model

Table 5-1 Initial kinematic parameters

						unit: inch
a_1	a_2	a_3	a_4	a_5	a_6	
43.10642755	43.10642755	43.10642755	43.10642755	43.10642755	43.10642755	
	r	b	h	L_c		
	68.233	34.1165	59.09151137	35		

5.1 Simulation Setup and Environment

The flowchart for the calibration simulations is shown in Figure 5-2. The approach taken during the course of the identification simulations was as follows. The measurement strategy and number of poses were decided first. The initial HCMM configuration was given as shown in Table 5-1. The center rod motion then was created by using the observation strategy (see Section 5-2). The HCMM reverse kinematic model then was applied to these center rod positions to generate the strut length change data, followed by a check of the strut displacements to ensure all the motions are within the working space of the HCMM. The strut length changes and actual center rod position coordinates for each poses then were saved in a file, with 14 place decimal accuracy. A uniformly distributed random noise of measurement was superimposed on the strut length changes before saving to the data file.

The programs to generate measurement data and to implement the least-squares identification method were written and ran in MATLAB on a Windows 95 based personal computer. When the calibration procedure was completed, the lower sphere position at each pose was estimated by applying the identified kinematic parameters and the data of the stored strut length changes in the forward kinematic model. The lower sphere

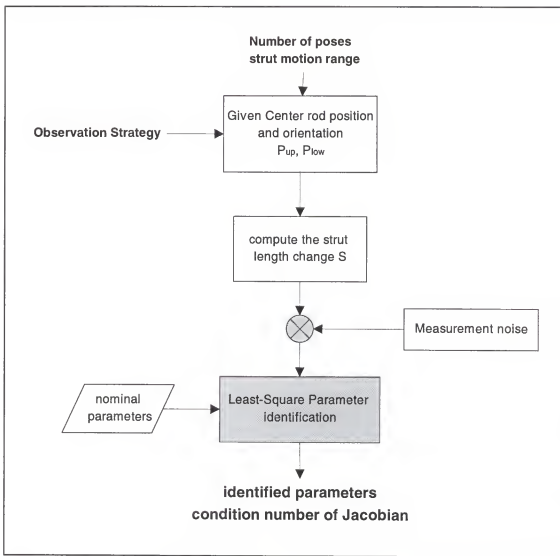


Figure 5-2 Flowchart for calibration simulation

position errors were determined by comparing these estimated lower sphere positions and the stored exact lower sphere positions.

The symbols used in the simulation results table are as follows. The number of poses is “ m .” The error value used for the ten nominal parameters in the HCMM model is “ δA .” The measurement uncertainty is represented by Un which is assumed as uniform distribution with zero mean. The measurement strategy types are “*Strg*.” After the calibration procedure is completed, the identified parameter errors $\delta a_1, \dots, \delta a_6, \delta r, \delta b, \delta h$, and δL_c are represented as “ δA_{ms} ” which is found by taking the root mean square of all ten parameter errors. The charged CPU time for execution is “ t_{cpu} .” The condition number of the identification Jacobian is “*Cond(J)*.”

In our iterative least-squares algorithm each entity in the Jacobian matrix was calculated analytically by taking the partial derivative of objective function Equation 3-25. The iterative procedure was terminated when the maximum value in the parameter update vector, ΔA , became less than 10^{-12} inch.

5.2 Measurement Strategy

Several measurement strategies have been examined through the computer simulation. The number of poses was chosen as $m=200$ for all the strategies. A noise level $Un=10\mu$ inch was superimposed on the length change before that data was stored. A initial guess error $\delta A=0.5$ inch was added to each of the exact parameter values. The first strategy type is called “straight line motion.” The center rod was moved along a straight line with a unit vector (0.6674, 0.6674, 0.3304) and was kept in constant

orientation during the movement. The strut length changes were stored at every 0.075 inch interval along the center rod travel. The changes in length are shown in Figure 5-3.

A 200×10 Jacobian matrix was formed by the pose set. Since there is a linear relationship between the HCMM configurations, this measurement strategy is not sufficient to create a Jacobian matrix where the rank of J is less than 10. It is not identifiable in the computer simulation.

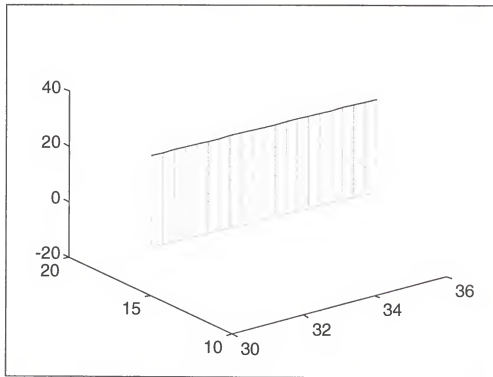


Figure 5-3 Straight line motion

The second strategy is called "2D circular motion," in which the locus of the center rod forms a 10 inch diameter cylinder. Meanwhile the center rod was kept at the same z height and parallel to the z axis. The strategy is shown in Figure 5-4. The same input conditions as strategy 1 were used in the computer simulation.

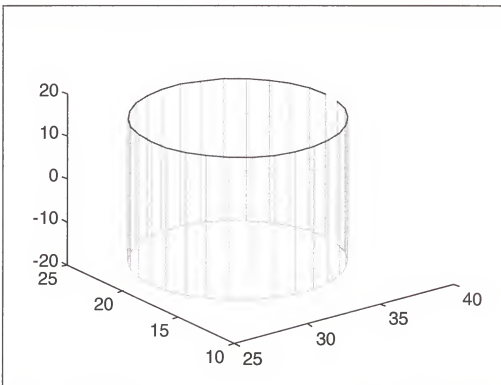


Figure 5-4 2D circular motion

Since the upper and lower spheres only move in the x and y direction, some kinematic parameters will be linearly dependent on others. Thus the rank of the Jacobian matrix from this measurement strategy would be non-full. Consequently the parameters are not identifiable by using this strategy.

The first two strategies only involve linear or planar motion. Even the 200 poses used could not provide enough information for identification. Thus a squared sine wave motion in the z direction was added to the 2D circular motion, where the center rod moved up and down following the curve $z_i = 13 \times (\sin(\theta_i))^2$. Therefore this third measurement strategy is called “3D sine wave circular motion”, shown in Figure 5-5.

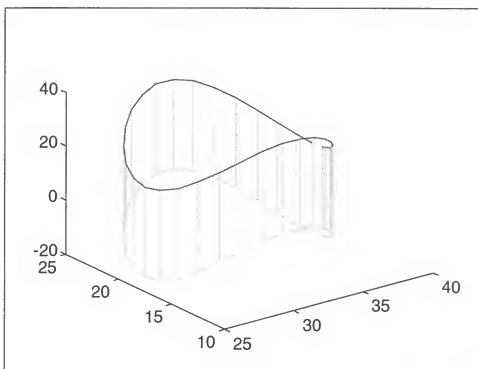


Figure 5-5 3D sine wave circular motion

The same input conditions as strategy 1 were used in this computer simulation.

The identified parameter error δA_{rms} is 0.00238 inch. The parameter error is still so big that this strategy would not be adopted.

In the first three strategies the center rod was kept parallel to the z axis. The forth measurement strategy is designed to change the center rod orientation during data collection. The center rod was tilted 45 degrees from z axis. Then it followed the same motion type as the third strategy. Therefore, the center rod orientation will vary from position to position. This motion is then called “tilted 3D sine wave circular motion,” as shown in Figure 5-6. The same input conditions were used here as in the other three strategies. The identified parameter error δA_{rms} is 0.00210 inch, which is still in the same error level as the third strategy.

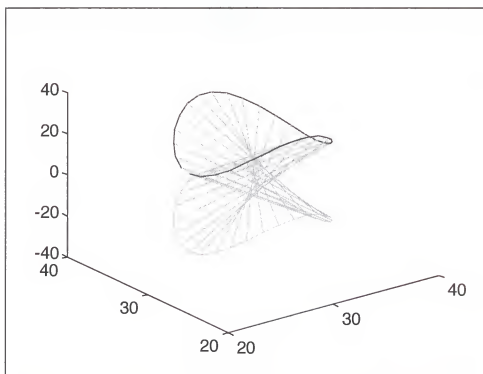


Figure 5-6 Tilted 3D sine wave circular wave motion

The last measurement strategy was called “random motion strategy” as shown in Figure 5-7. Each time the center rod was moved to a different position and orientation randomly. Since there is no clear relationship between the 200 configurations, this measurement strategy provided sufficient exciting for the identification matrix. This can be seen from the calibration result which identified the parameters with error as of $\delta A_{rms} = 71\mu$ inch. The result also shows a smaller condition number compared with the other four strategies. The comparison of all the five strategies is listed in Table 5-2.

Table 5-2 Comparison of measurement strategies

	Strg 1	Strg 2	Strg 3	Strg 4	Strg 5
δA_{rms}	not identifiable	not identifiable	$2378 \mu \text{ inch}$	$2100 \mu \text{ inch}$	$71 \mu \text{ inch}$
cond(J)	ill condition	ill condition	11540	12917	430
m=200	noise-10u-10uin	initial 8A=0.5"			

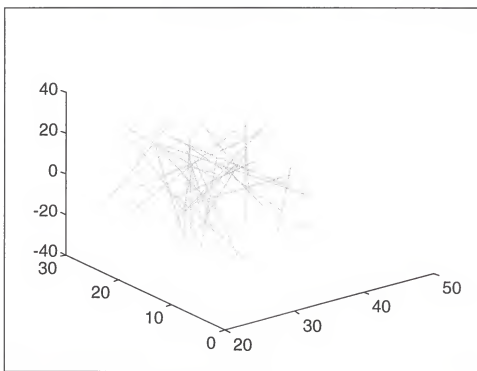


Figure 5-7 Random motion

5.3 The Effect of Linear Displacement Measurement Error on Sphere Position

As we know the linear displacement measurement in a strut is performed by the laser interferometer system. In this section we will investigate how much the linear displacement measurement error will affect on the accuracy of sphere position if the true initial kinematic parameter values are known. In keeping with the conventions of mechanical metrology, the measurement error should be treated as an unknown value. It should be described as the “measurement uncertainty” instead of using the word “error.” The measurement uncertainty could exhibit any distribution pattern including normal distribution or uniform distribution. If no statistically valid description could be determined for this measurement uncertainty, a Type B uniform measurement error distribution could be assumed (see Taylor [42]). Because we do not have the statistically

described information for the laser interferometer error, the Type B uniform measurement error is assumed and will be used in our remaining simulation.

In the simulation, an arbitrary HCMM configuration was chosen from within the work volume of the machine. If the linear displacement measurements were subjected to uniformly distributed random error over the range of $(-Un, +Un)$, the absolute strut length error will be the same as the linear displacement measurements because the true initial strut length was assumed to be known. Thirty thousand different configurations were examined ,then the sphere position error in each configuration were calculated and recorded. The averaged position error in each of the X,Y, and Z directions was calculated by taking the mean of all position errors. The uncertainty “ σ_{ij} ” associated with the position error is found by taking the standard deviation of the position errors. The symbol “ i ” in “ σ_{ij} ” represents the direction (X,Y,or Z), and “ j ” represents the sphere (upper or lower). Keeping the same pose but doubling the uncertainty level the position error was then calculated again. Five noise levels were tested. It is interesting to find that the distribution of the position error in 30000 configurations resulted in a normal distribution in each direction for each sphere. The mean value of the position error was on the order of 10^{-8} inch in all the directions which is so small that position error can be treated as an unbiased normal distribution. The position uncertainties of the spheres under different levels of linear displacement measurement error are listed and plotted in Table 5-3 and Figure 5-8. It was found that the position accuracy is linearly dependent on the linear displacement measurement uncertainty. It also can be observed that positional uncertainty in the X or Y direction is approximately half of the measurement uncertainty level, and in the Z direction has the same order of magnitude as the measurement

uncertainty level. The small residual variances in the position error when U_n is 0 are attributed to computational error in the computer simulation.

Table 5-3 The effect of strut length error on sphere position

U_n (inch)	σ_{xu} (inch)	σ_{yu} (inch)	σ_{zu} (inch)	σ_{xl} (inch)	σ_{yl} (inch)	σ_{zl} (inch)
0	3.9×10^{-15}	3.6×10^{-15}	1.2×10^{-14}	3.7×10^{-15}	3.9×10^{-15}	1.2×10^{-14}
$-5\mu \sim 5\mu$	2.6μ	2.6μ	5.4μ	2.6μ	2.6μ	5.6μ
$-10\mu \sim 10\mu$	5.2μ	5.2μ	10.6μ	5.2μ	5.2μ	11.1μ
$-20\mu \sim 20\mu$	10.2μ	10.2μ	22.0μ	10.2μ	10.2μ	22.4μ
$-40\mu \sim 40\mu$	20.8μ	20.6μ	44.6μ	20.4μ	20.6μ	45.3μ

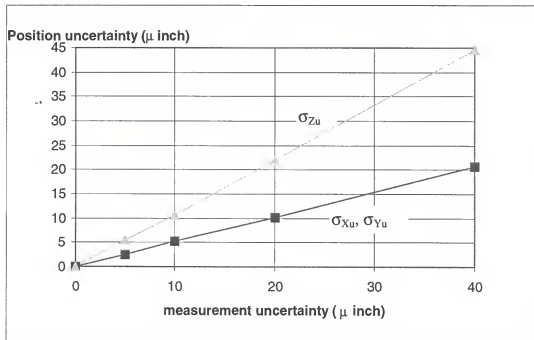


Figure 5-8 The effect of strut displacement measurement error on sphere position

5.4 The Effect of Measurement Uncertainty on Calibration Results

In the previous section we assumed that the true initial kinematic parameter values are known, and, discussed the influence of the strut displacement measurement uncertainty on the positioning uncertainty of the spheres. However, in reality the exact

values of the kinematic parameters are unknown and, therefore, the exact sphere position is impossible to determine. Thus an identification procedure is needed to provided the most accurate parameter value. The following test is designed to determine the effect of the strut displacement measurement noise on the kinematic parameter identification process. To control the experimental factor, the poses used in parameter calibration procedure will be fixed. The only variable left is the magnitude of the measurement uncertainty level Un . Thirty poses were generated by using strategy 5. Uniformly distributed random noise with magnitude Un was then superimposed on the strut length changes to simulate the measurement uncertainty. The approximate or nominal parameter values may be obtained by simply using a tape measure. In this simulation a 0.5 inch initial parameter error “ δA ” was added to each of the ten true parameters of the HCMM as the nominal parameter values for least-squares algorithm. After the calibration procedure was completed, the root mean square value of the ten kinematic parameter errors was stored as “ δA_{ms} .” The position errors in upper and lower spheres also were recorded “ δP .”

In order to evaluate the effect of noise magnitude on sphere position estimation, five hundred simulations were performed. Each simulation run used the same poses and noise magnitude. The results were different for each simulation because the randomly generated noise was different each time. The simulation flowchart is shown in Figure 5-9.

The relationship between strut displacement measurement uncertainty and the calibration results then could be addressed by statistical means. From Table 5-4 and Figure 5-10 it can be observed that when the measurement uncertainty level was doubled, the calibration errors also doubled. This test also shows that the parameter values could

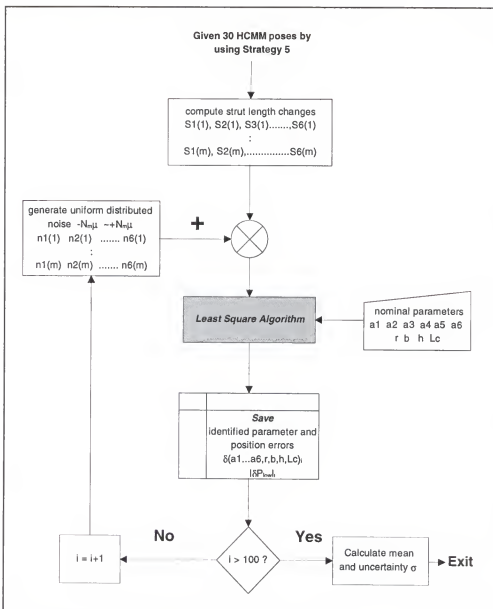


Figure 5-9 Flowchart for finding the relation between the strut displacement measurement uncertainty and calibration results

Table 5-4 Calibration results subjected to different strut displacement measurement uncertainty level

meas. Uncert. Un	mean of δA_{rms}	$\sigma_{\delta A}$	mean of cond(J)	$\sigma_{Cond(J)}$	Unit: inch
0	2.31×10^{-13}	1.85×10^{-20}	453.53	4.10×10^{-3}	
-5μ-5μ	74.7μ	31.8μ	453.53	4.98×10^{-3}	
-10μ-10μ	152μ	66.4μ	453.53	5.00×10^{-3}	
-20μ-20μ	302μ	131μ	453.53	7.63×10^{-3}	
-40μ-40μ	619μ	280μ	453.53	1.40×10^{-2}	
Un	σ_{xu}	σ_{yu}	σ_{zu}	σ_{zl}	σ_{yl}
0	2.78×10^{-13}	6.76×10^{-14}	3.16×10^{-14}	2.77×10^{-13}	6.94×10^{-13}
-5μ-5μ	76μ	20.8μ	10μ	77μ	24.1μ
-10μ-10μ	150μ	42.8μ	19μ	154μ	51.5μ
-20μ-20μ	316μ	89.3μ	40.7μ	317μ	100μ
-40μ-40μ	638μ	178μ	82μ	648μ	200μ

unique pose set m=30 N=500 times initial $\delta A = 0.5''$

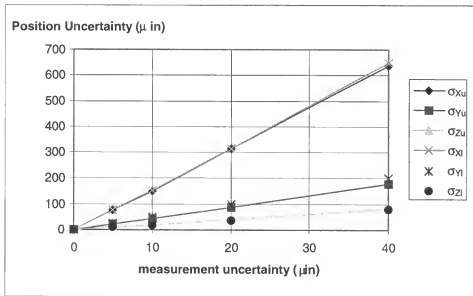


Figure 5-10 The effect of the strut displacement measurement error on the calibration results (Unique pose set, Cond=453, $\delta A=0.5''$, N=500 simulations)

be identified to nearly their true values if no measurement error was applied. But once the measurement error was introduced, it became impossible to obtain the exact parameter values.

By using the same calibration poses only a slight increase was observed in condition number when the measurement uncertainty went up. This shows that the condition number was mainly determined by the selected poses. It also can be observed from Figure 5-10 that both of the upper and lower spheres in the Z-direction have the smallest positional uncertainty. The X-direction has the largest positional uncertainty. Why does this occur? To explain this phenomena, we trace back to the calibration method. The objective function of the self-calibration algorithm is to find a set of parameters such that the center rod length has the minimum deviation in all the configurations. After we performed the calibration, the least squares method found an optimal set of parameters that made the deviation in the center rod length the smallest. As we know, the center rod length is derived from a set of equations, Equation 3-2 to Equation 3-8. All the ten kinematic parameters are necessary to compute the center rod length deviation. However, the X-coordinate is the first equation in the series of equations used to obtain the center rod length. It only uses four of the ten kinematic parameters as shown in Equation 3-2 and Equation 3-5. The search procedure does not find the four parameters which yield the best estimate for the X coordinate, but rather the center rod length with the least deviation. In contrast, the Z coordinate is the final equation in the series. Six parameters are needed to compute each Z-coordinate. Furthermore, since the center rod orientation never deviates more than 30° from the vertical, the center rod length is more strongly dependent on the Z coordinate of the

spheres than it is on the X and Y coordinates. Therefore, it can be expected that Z has the smallest uncertainty level after calibration.

It should be noted that a calibration using different calibration pose sets could produce a different uncertainty level in the resulting estimation of the ten kinematic parameters.

5.5 The Effect of Pose Selections on Calibration Results

Each pose set has a unique sensitivity level for the measurement noise, such that using a different pose set would yield different calibration results. To determine the noise sensitivity of a pose set, a widely used index is the condition number of the Jacobian matrix J . In the previous simulation the identical pose set was used to find the relationship between measurement uncertainty and calibration results. In order to understand the effect of pose set selection on the calibration results, a thousand calibration simulations were performed. For each simulation a pose set consisting of 30 poses was generated by using a random selection strategy. The flowchart of this simulation is shown in Figure 5-11.

The calibration results for $U_n = \pm 10\mu$ inch are shown in Figure 5-12. Each circle point in Figure 5-12 represents a simulation result of δA_{rms} . Each pose set is associated with its condition number which represents its sensitivity level to noise.

One can observe from the simulation results that a pose set with smaller condition number does not guarantee that the calibration results will be better than the pose set with higher condition number. However, comparing the upper boundaries of condition numbers, one can see the trend that the pose sets with smaller condition numbers have

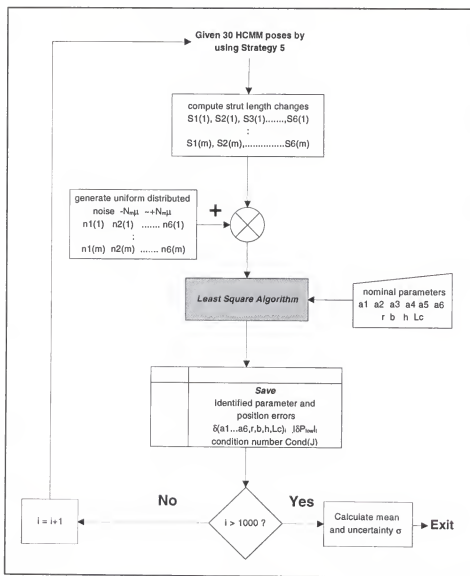


Figure 5-11 Flowchart of calibration simulation designed for understanding the effect of pose selection on the calibration results

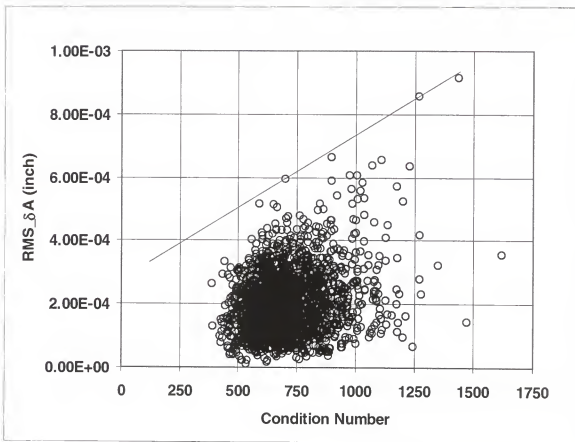


Figure 5-12 Calibration results and the corresponding condition number for each pose set ($m=30$ poses, $U_n=\pm 10\mu$ inch, $N=1000$ simulations)

smaller upper bound in position errors. If we draw a straight line above all the points in Figure 5-12, we can see the trend. A more detailed discussion of this issue will be described in Section 5-7.

From the above simulation we found that δA_{rms} varies from 10.4μ inch (cond=531) to 916μ inch (cond=1430). However, for a randomly selected pose set the calibration result has a large possibility of being located in the region of the mean value from 1000 simulation results. Thus we choose to use the mean value and its standard deviation of the 1000 simulation results to represent the overall calibration results. This

simulation was repeated for different levels of measurement uncertainty. The results are listed in Table 5-5.

Table 5-5 The relation between the strut displacement measurement uncertainty and calibration results

meas. uncert. Un	mean of δA_{rms}	$\sigma_{\delta A_{rms}}$	mean of $Cond(J)$	Unit: inch $\sigma_{Cond(J)}$
0	3.24×10^{-13}	2.37×10^{-20}	713	150.4
$-5\mu \sim 5\mu$	104μ	52.9μ	712	154.4
$-10\mu \sim 10\mu$	206μ	101μ	710	148.8
$-20\mu \sim 20\mu$	426μ	206μ	715	146.2
$-40\mu \sim 40\mu$	817μ	395μ	707	148.3

m=30 poses

N=1000 times

initial $\delta A = 0.5$

This result is similar to the previous section's result in that the overall calibration results are linearly dependent on the measurement uncertainty. These results also show that in the absence of measurement uncertainty, the parameters could be exactly identified as long as its Jacobian matrix is not ill conditioned.

5.6 The Effect of Number of Poses on the Calibration Results

To investigate the importance of the number of poses to the calibration results, these calibrations are separated into five groups with m=30, 50, 100, 200, and 300 poses respectively. The measurement uncertainty is assumed to be $\pm 10 \mu\text{in}$ for each of the five cases, and the initial nominal parameter error is 0.5 inch for all parameters. For the cases of m=30, 50 and 100 poses a total of 2000 simulations for each group were performed. The poses in each simulation are regenerated by using strategy 5. For the cases of m=200 and 300, a total of 1000 simulations were performed.

The results shown in Table 5-6 demonstrate that with an increasing number of poses in the calibration procedure, a decreasing condition number will result. Thus better

calibration results can be expected. It also can be observed that when the number of poses is more than 200, the improvement in calibration result is minimal.

Table 5-6 The Effect of number of poses

no. of poses (m)	mean of δA_{rms}	$\sigma_{\delta A_{rms}}$	mean of cond(J)	$\sigma_{Cond(J)}$	CPU time(sec)
30	206 μ	101 μ	710.1	148.8	0.86
50	143 μ	66.5 μ	566.8	87.6	1.56
100	100 μ	44.0 μ	481.3	58.1	2.90
200	71.6 μ	32.2 μ	436.4	41	5.86
300	59.2 μ	26.1 μ	417.0	35.5	9.31

Strategy: 5

Un= $\pm 10\mu$ in

initial $\delta A=0.5''$

CPU: Pentium 200

The diamond line in Figure 5-13 shows the mean of δA_{rms} from the calibration simulation results, and the square line shows the error amount after adding the standard deviation to the mean position error. If the measurement uncertainty is within $\pm 10 \mu$ in and the pose set is randomly selected, it can be expected that the calibration result in δA_{rms} will have a 68.27% chance of falling below the square line. The maximum δA_{rms} from each of the 2000 simulations were recorded as the local upper bound. This bound gives us a general idea that most of the calibration results will not exceed these values.

Figure 5-14 shows the relation between the condition number and the number of poses used in the calibration. The more poses which are used in the calibration, the smaller the deviation in the condition number. Thus, the condition number is gradually losing its ability in determine the goodness of a pose set when the number of poses is greater than 200. This phenomena will be discussed in the next section.

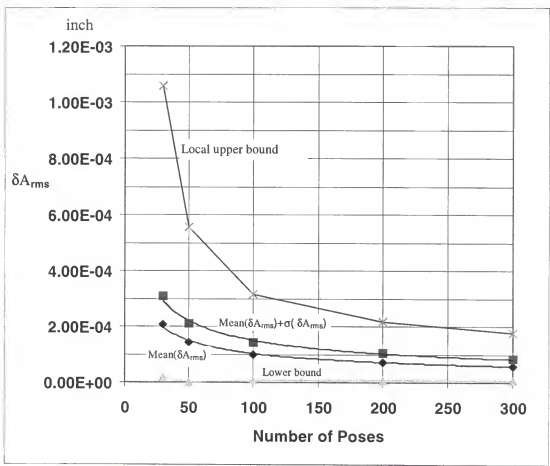


Figure 5-13 Parameter error vs number of poses (Un= ± 10 m inch)

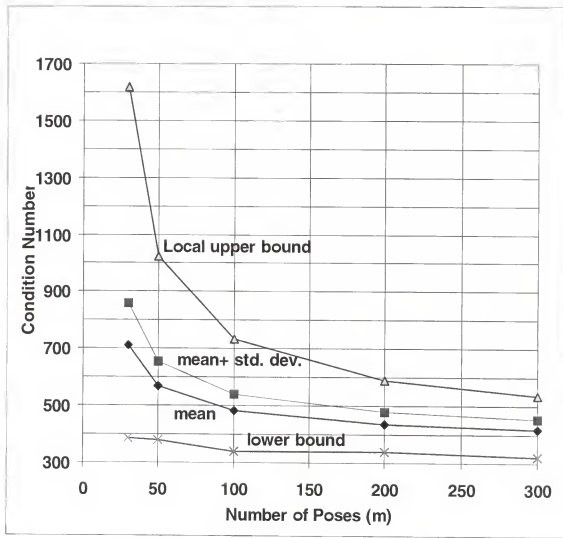


Figure 5-14 Condition Number vs. Number of Poses

5.7 The Sensitivity Analysis on Condition Number

In previous sections we observed from the simulation results that a pose set with smaller condition number does not guarantee that the calibration result will be better than the pose set with higher condition number. We also observed that the more poses which were used by the calibration routine, the smaller the deviation in the condition number. In this section we will investigate how the condition number can help us in selecting a pose set that will have a better chance to obtain good calibration results, and the limit to the condition number's usefulness.

According to the magnitude of the condition number, we selected several groups of pose sets. Each group contains two to three pose sets, and each pose set in the same group contains 30 poses with condition number which varies in range ± 5 . For each pose set 300 calibration simulations were performed as shown in Figure 5-9. In each simulation, a uniformly distributed measurement uncertainty of $\pm 10 \mu\text{in}$ was superimposed on the strut length changes, and the initial parameter error was 0.5 inch for all the ten kinematic parameters. Each of the calibration simulation results was represented as a circle as shown in Figure 5-15. The calibration results in each group were represented in a statistical manner as listed in Table 5-7 and plotted in Figure 5-16.

To verify the accuracy of the statistical representation for condition number, we performed ten thousand calibration simulations. In each simulation, we arbitrarily selected 30 poses and applied the same noise level and initial parameter errors as in the above simulations. The accuracy of the statistical representation was verified by plotting the ten thousand simulation results on top of Figure 5-16 as shown in Figure 5-17.

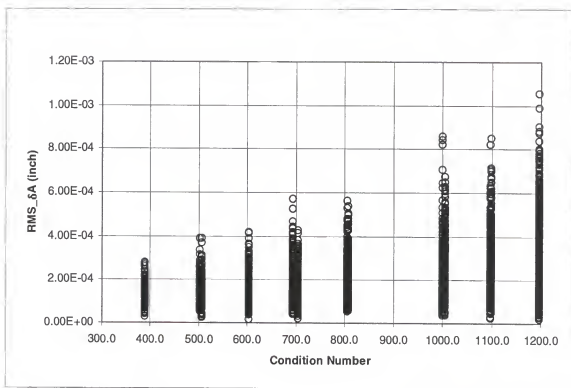


Figure 5-15 Test of condition number

Table 5-7 Statistical representation for condition number

condition Number	mean of δA _{rms}	std. dev. δA _{rms}	minimum δA _{rms}	maximum δA _{rms}	unit: μ inch
388	145	59	29.0	281	
504	160	70	24.2	391	
602	169	85	18.0	461	
699	192	96	21.4	537	
805	220	103	32.5	728	
1003	262	144	35.0	859	
1098	278	142	16.1	894	
1203	296	165	20.5	1060	

m=30

initial δA=0.5"

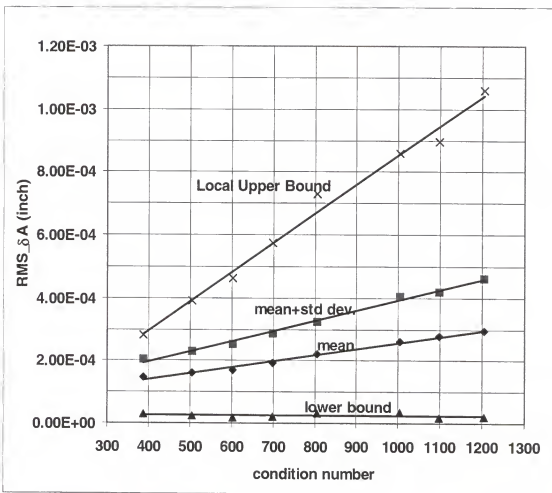


Figure 5-16 The statistical representation for condition number

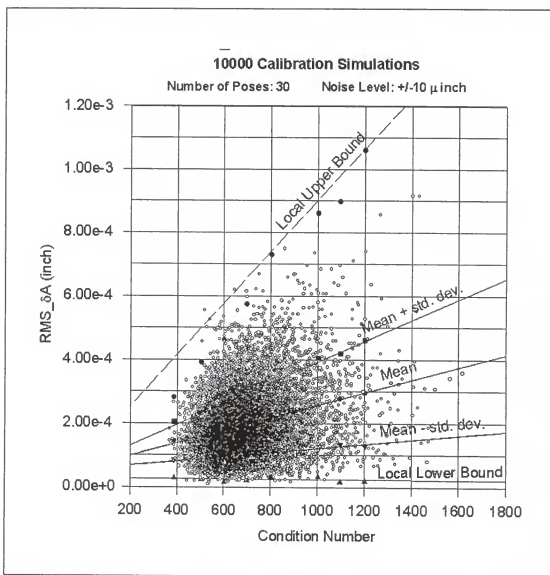


Figure 5-17 Verification of the statistical representation for condition number

Figure 5-17 to Figure 5-19 show the statistical representations for the calibration simulation results by using different numbers of poses in the calibration. It can be observed that more poses used in the calibration resulting in a smaller scattering zone for the calibration results. The comparison of the condition number sensitivity is shown in Figure 5-20. Each line in Figure 5-20 is the mean statistical line for $m=30, 50, 100$, and 200 . At $m=30$, a pose set with a smaller condition number will statistically have better calibration results than a pose set with a higher condition number. But, for the case of $m=200$, a pose set with a smaller condition number does not mean it will have better calibration results than a pose set with a higher condition number. Therefore, we realize that condition number loses its sensitivity when more poses are used in calibration.

To choose an optimal pose set with 30 poses, we performed ten thousand calibration simulations and used the condition number as our searching index. The best pose set we found has a condition number of 388. Another best pose set with 50 poses also was found using the same method which has a condition number of 347. These two best pose sets are listed in the Appendix B.

5.8 The Effect of Nominal Value on the Calibration Results

To facilitate a numerical solution method, the nonlinear least-squares equation is linearized at its nominal values. Therefore, it is necessary to understand the effect of the nominal parameter error on the calibration results. Three pose sets were tested. Each pose set includes thirty poses selected by strategy 5. The nominal parameter errors were increased from zero to more than three inches. Table 5-8 shows the calibration results were identical as long as the least-squares objective function does not diverge. The

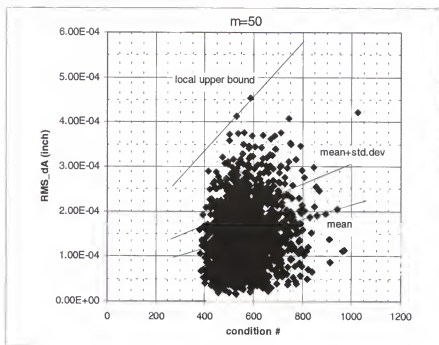


Figure 5-17 Statistical representation for calibration simulation results ($m=50$)

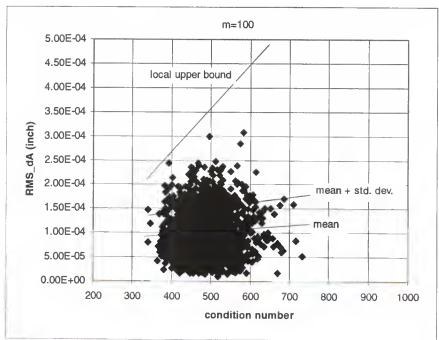


Figure 5-18 Statistical representation for calibration simulation results ($m=100$)

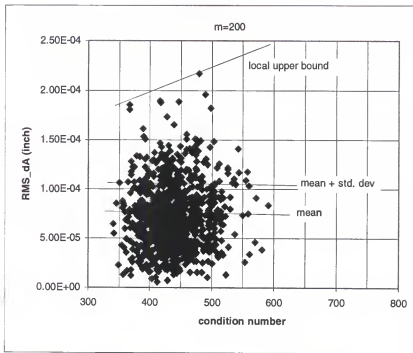


Figure 5-19 Statistical representation for calibration simulation results ($m=200$)

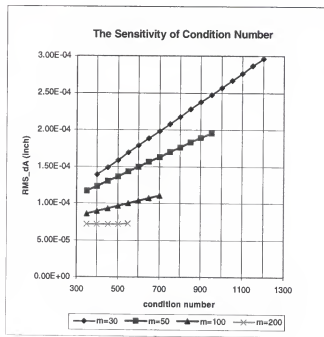


Figure 5-20 Sensitivity of the condition number

divergence will happen when the parameter errors are large enough to cause Equation 3-4 or Equation 3-7 to become a complex number. The divergence can be avoided by choosing a more accurate nominal parameter value or by selecting a different pose in which the complex number does not appear in the objective function. However, in all cases where the objective function does in fact converge, the calibration result will not be affected by the initial nominal parameter error.

Table 5-8 The effect of initial nominal value error

initial nominal parameter error	pose set #1 δA_{rms}	pose set #2 δA_{rms}	pose set #3 δA_{rms}	unit: in
0	173.8 μ	144.2 μ	193.6 μ	
1	173.8 μ	144.2 μ	193.6 μ	
1.5	173.8 μ	144.2 μ	193.6 μ	
2	173.8 μ	144.2 μ	193.6 μ	
2.5	173.8 μ	144.2 μ	193.6 μ	
3	173.8 μ	diverge	diverge	
above 3	diverge	diverge	diverge	strategy: 5
	m=30	Un= $\pm 10 \mu$ in		

5.9 The Comparison of Identification Methods

As mentioned earlier, many methods can be used to solve for the nonlinear least-squares problem. The two most widely used methods are the linearized least-squares method and the Levenberg-Marquardt method (LM method) which is a non-linear method, or a modification of Newton's method. The simulations were run in MATLAB under Windows 95 on a Pentium 200 personal computer. Table 5-9 shows the comparison of these two solution methods. Both the linearized and the non-linear method (LM method) gave almost identical calibration results under the same conditions. This table takes twelve cases of increasing numbers of poses and compares the CPU time

taken by the two methods. The linearized method is seven to twelve times faster than the non-linear LM method. At 200 poses the linear method takes about six seconds, while the LM method takes more than 48 seconds of CPU time.

Table 5-9 The comparison of two identification methods

		Linearized method	LM method		
		t_{cpu} (sec)	δA_{rms} (μm)	t_{cpu} (sec)	δA_{rms} (μm)
m=30	test 1	0.86	193.606	7.8	193.606
	test 2	0.82	188.715	7.8	188.727
	test 3	0.88	253.861	8.41	253.861
m=50	test 1	1.76	101.831	13.35	101.843
	test 2	1.15	88.579	10.82	88.582
	test 3	1.16	107.816	14.01	107.822
m=100	test 1	2.69	34.585	26.47	34.585
	test 2	2.67	83.623	19.61	83.619
	test 3	3.06	47.473	21.26	98.731
m=200	test 1	5.43	39.840	55.3	39.840
	test 2	5.64	33.7	54.82	33.698
	test 3	6.21	44.089	48.17	44.087

5.10 Discussion

The kinematic parameters can be exactly identified only in the theoretical case which has no displacement measurement error and modeling error. When measurement uncertainty exist it is impossible for one to determine the true parameter values.

A good measurement strategy will improve the quality of the parametric identification results. In some cases, the parameters are unidentifiable from a given pose set, such as the straight line or circular motion. The best measurement strategy of those tested is random selection. Furthermore, it has been found that not all of the pose sets selected from the random strategy obtained acceptable calibration results. A good calibration result should be obtained when the pose set is least sensitive to strut

displacement measurement noise. From simulation, it shows that the calibration results are linearly decreased with the increase of the strut displacement measurement uncertainty.

It has been shown that increasing the number of poses and reducing the measurement error are two methods to improve the calibration quality. In general, the quality of initial nominal parameter guesses will not affect the identification result. When the number of poses are limited to less than 200, a significant factor that will improve the calibration quality is the pose set selection. Thus, the condition number of the identification matrix can be used as an important indicator during the selection of the poses. The condition number computed from the experiment can be used to refer back to the simulation tables and estimate the quality of the pose set, and suggest a level of confidence in parameter identification.

CHAPTER 6

THERMAL EFFECTS

From the previous chapter, it is known that the self-calibration method is very sensitive to the measurement error of the strut linear displacement. When the environmental temperature varies, the components in the HCMM will exhibit a change in their dimensions. Though the whole calibration procedure is assumed to be completed in a very short time period, the thermal effect inevitably will have some affect on the accuracy of the linear displacement measurement in each strut. Thus, to investigate the thermally induced error of the linear displacement measurement in a single strut is one objective of this chapter. The self-calibration method is based on the center rod remaining a constant length during the calibration operation period. Since the center rod will experience thermally induced changes, qualification of the thermal effect on the center rod is a second objective of this chapter.

The coordinates of a probe are obtained by knowing the absolute lengths of the six struts and the three base sphere distances. If these lengths are not corrected when the thermal effect occurs, the length errors will propagate through the probe coordinate calculations and cause errors in the measured position of the probe. Thus, understanding the thermal deformation in each component is another objective of this chapter. Furthermore, thermal effects may increase over time. Thus, to determine the time period beyond which the HCMM needs to be re-calibrated, when the thermal uncertainty may have exceeded the allowable tolerance is included.

Since the actuator is used to control the motion of the strut, it must generate some heat during its operation. To investigate if the generated heat in a motor will cause a significant effect in the measurement error of the strut length is the last subject in this chapter.

Assumptions must be made before any thermal analysis is undertaken. As we know the net thermal effect can be represented as the combination of effects from three distinct mode of heat transfer: conduction, convection, and radiation. We do not expect there to be any high temperature heat sources nearby or in contact with the HCMM. Therefore, for simplicity in the thermal analysis, we assume the effect of radiation between the environment and the HCMM can be ignored. The only thermal effect on the HCMM considered in this chapter is the natural convection between the ambient atmosphere and the surface of the HCMM. We also assume that the ambient temperature is uniformly distributed throughout the environment, such that the ambient temperature is considered to be a function of time only.

6.1 Thermally Sensitive Components

The absolute length of a strut is measured from the base sphere center to the moving sphere center. Strut components include two reference spheres, shoulder, actuator, ball screw, and the pin followers. The components and the associated dimensions of a strut are shown in Figure 6-1. In a strut, the laser interferometer system will detect a length change from its emitter to the retroreflector. However, the thermal growth in the components which is not covered by the laser path will not be detected.

This unmeasured thermal growth, then, will be treated as a noise or measurement error in the strut length.

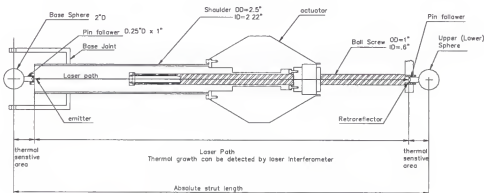


Figure 6-1 The thermal sensitive components in a strut

The center rod, as shown in Figure 6-2 contains three different material elements: reference spheres, joint holder, and fiberglass tube. When the ambient temperature changes, the center rod will change its length so that the constant center rod length assumption will be violated. Understanding the thermal response of the current center rod design will help us in designing a new center rod if the redesign is necessary.



Figure 6-2 The center rod

Because the base spheres are fixed on the triangle frame as shown in Figure 6-3, any thermal growth in the triangle frame, will cause the distance between the base spheres to change. If the thermal growth is not corrected from the nominal values, it will

propagate to increase the uncertainty of the calculated probe coordinates. Symmetry prevents the triangle frame from being distorted when it is subjected to an environmental temperature change. Thus, equal thermal growth rate is assumed for the thermal effect analysis.

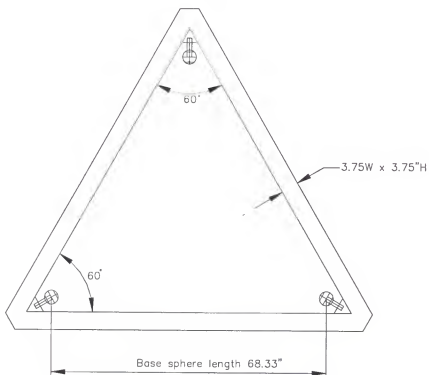


Figure 6-3 The triangle frame

The supporting frame is another component that needs to be considered. From Figure 6-4, one can observe that any thermal growth in the columns will make the triangle frame move up or down. Therefore any relative position changes between the world coordinate system and the granite table will be directly added onto the measurement error in the Z-direction, but not through the error propagation procedure.

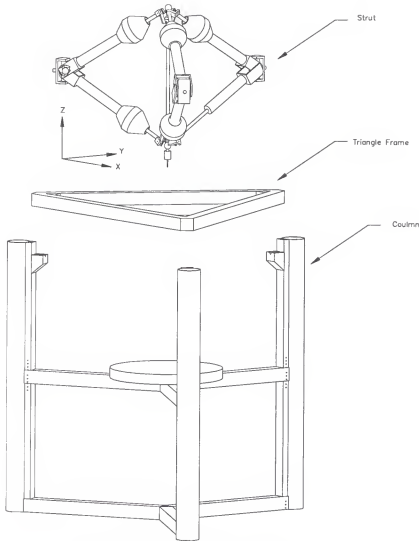


Figure 6-4 The HCMM assembly

6.2 The Thermal Response in The Sensitive Components

For a shop floor with conventional heating or cooling systems, the ambient temperature could be idealized as shown in

Figure 6-5. The temperature variation range and its cycle frequency will depend on the setup of the heating or cooling systems. In this case, it is important to know the thermal response of the HCMM components under typical ambient variation.

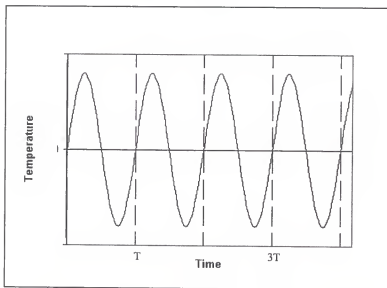


Figure 6-5 The temperature variation in a shop floor

Review of Heat Transfer

To analyze the thermal response, according to Incropera and DeWitt [43], first we check the *Biot number* of a solid component in its thermal model. The Biot number is a dimensionless group and is defined as shown in Equation 6.1.

$$Bi = \frac{h_c L_s}{k} \quad (6-1)$$

The h_c is the thermal convection coefficient between the air and the surface of the solid component. The L_s is the characteristic length which is defined as the ratio of the solid volume to surface area, $L_s = V/A_s$. The k is the thermal conductivity of the solid. For a Biot number which is much less than 1.0, the thermal model can be treated as a *lumped system*. In the lumped system model it is assumed that the temperature distribution within the solid at any instant is sufficiently uniform that the temperature of the solid can be considered to be a function of time only. For a the Biot number less 0.1, the assumption of uniform temperature distribution has an error less than 5 percent.

For a lumped system the energy equation for heat transfer in the solid may be stated as : (*rate of heat flow into the solid of volume V through boundary surfaces A*) = (*rate of increase of internal energy of the solid of volume V*). By writing the appropriate mathematical expression for each of these terms, it becomes

$$h_c A_s [T_\infty - T(t)] = \rho V c \frac{dT(t)}{dt} \quad (6-2)$$

where ρ = kg/m³ is the density of the solid, c = (J/(kg. °C)) is the specific heat of materials. V is its volume, A_s is its surface area. T_∞ is the ambient temperature.

To solve Equation 6-2 we must specify the temperature of the body at a particular time. If we assume that the temperature of the body at an initial time, $t=0$, is known to be T_0 , we say that the initial condition for Equation 6-2 is $\theta_0 = T_0 - T_\infty$ at $t = 0$, and $\theta(t) = T(t) - T_\infty$. The solution to Equation 6-2 is

$$\frac{\theta(t)}{\theta_0} = e^{-(k_c A_s / \rho V c)t} \quad (6-3)$$

Equation 6-3 can be rewritten as

$$\frac{\theta(t)}{\theta_o} = e^{-t/\tau} \quad (6-4)$$

where τ represents thermal time constant of the solid, and its value is

$$\tau = \frac{\rho V c}{h_c A_s} \quad (6-5)$$

When the environmental temperature is known, the temperature in the solid component can be estimated by using Equation 6-4. For instance, a steel ball with a uniform temperature of T_o is suddenly moved into a room where the air temperature is well maintained at T_∞ all the time. The time required for the steel ball to rise 63.2% of the temperature difference between the air and steel ball initial temperature is called the time constant, as shown in Figure 6-4(a). The temperature of the steel ball at time t can be estimated using Equation 6-4, and can be written as

$$T(t) = T_\infty + (T_o - T_\infty)e^{-t/\tau} \quad (6-6)$$

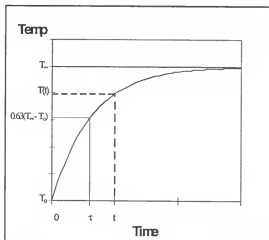


Figure 6-4(a) The thermal response subjected to a step input

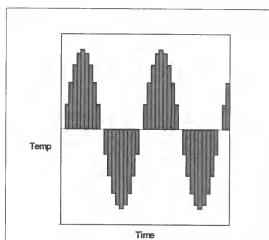


Figure 6-6(b) Discretized the sinusoid curve

For an environment with a sinusoidally varying temperature, the temperature curve can be discretized by dividing the time into several small steps. During each time step the air temperature is assumed to remain constant, as shown in Figure 6-4(b). Thus, Equation 6-6 can be applied in this case and rewritten as

$$T_{n+1} = T_{air(n+1)} + (T_n - T_{air(n+1)})e^{-\frac{\Delta t}{\tau}} \quad (6-7)$$

where n is an integer starting from 0. Δt is the time interval of a step.

Once the temperature of the solid is obtained, the thermal growth of the solid can be calculated by the following formula

$$\Delta L = \alpha \times L \times \Delta T \quad (6-8)$$

where α is the thermal expansion coefficient of the solid, L is the length of the solid in the thermal growth direction, and ΔT is the temperature change of the solid from the initial temperature.

Lumped System and Thermal Time Constant

To verify if the lumped system model is applicable on the HCMM's thermally sensitive components, and furthermore to obtain the time constant of each component, the physical properties of each component in HCMM have to be obtained first. The listed physical property of a material in different reference handbooks show different values if its exact chemical formulation is not available. The physical properties shown in Table 6-1 are the average values taking from different reference resources [43-46]. For instance, for stainless steel, the uncertainty range is about 2% for density (ρ), 10% for thermal conductivity (k), 8% for specific heat (c), and 10% for the thermal expansion coefficient(α). Here we take the average from the available data in different resources.

The uncertainty level for aluminum is about 2% for density (ρ), 20% for thermal conductivity (k), 10% for specific heat (c), and 2% for the thermal expansion coefficient (α). The material properties for fiberglass tube is not available from the handbooks mentioned in above. Its thermal expansion coefficient is obtained through a simple experiment. A small section of fiberglass tube of 0.12616m was measured at 25°C. Then it was placed in a freezer for a long time such that its temperature was close to the freezer's temperature, 0°C. The fiberglass tube was measured again, and its length was 0.12604m. If the fiberglass tube is assumed to have the same temperature as the freezer, its thermal expansion coefficient can be calculated as:

$$\alpha = \frac{\Delta L}{L \times \Delta T} = \frac{120 \times 10^{-6} m}{0.12604 m \times 25^\circ C} = 38 \times 10^{-6} /^\circ C$$

Table 6-1 Physical properties of the HCMM components

	base sphere ballscrew pin follower	triangle frame cylinder column	strut shoulder	center rod
material	stainless steel	cast steel	aluminum	fiberglass
density ρ (kg/m ³)	7750	7700	2750	Not Available
thermal conductivity k @ 300°K (W/m/ °C)	17.5	43	190	Not Available
specific heat c (J/kg/ °C)	500	440	900	Not Available
thermal expansion coefficient α	$16 \times 10^{-6} /^\circ C$ (or $8.9 \times 10^{-6} /^\circ F$)	$14 \times 10^{-6} /^\circ C$ (or $7.8 \times 10^{-6} /^\circ F$)	$23.5 \times 10^{-6} /^\circ C$ (or $13 \times 10^{-6} /^\circ F$)	$38 \times 10^{-6} /^\circ C$ (or $22.2 \times 10^{-6} /^\circ F$)

The Biot number was first checked for verifying the lumped system model, and its values for each thermally sensitive component is listed in Table 6-2. It has to be noted

that the value of convection coefficient of h_c is dependent on the type of fluid and the environmental conditions, such as the flow speed of the fluid over the surface of the solid. In general, for a given shop floor heating or cooling system, the natural convection coefficient (h_c) is between 10 and 25 $\text{W/m}^2/\text{°C}$. Here we assume $h_c=15 \text{ W/m}^2/\text{°C}$ for the case study in this chapter. Since the Biot number for all the components are far less 0.1, the lumped system model will be applied.

Table 6-2 The Biot number of each thermally sensitive component

	$h_c (\text{W/m}^2/\text{°C})$	$L_s (\text{m})$	$k (\text{W/m}/\text{°C})$	$Bi = h_c \times L_s / k$
sphere	15	$r/3=0.00847$	17.5	0.0073
pin follower	15	$r/2=0.00159$	17.5	0.0016
triangle frame	15	$w/4=0.0238$	43	0.0083
cylinder column	15	$r/2=0.04286$	43	0.0149

For a lumped system, the solution for transient thermal convection can be obtained from Equation 6-6. Equation 6-6 tells us that the temperature at any moment in a solid component is a function of its initial temperature, its thermal time constant, and the ambient temperature. The thermal time constant of a solid component will determine the quickness of the system in reaching equilibrium. From Figure 6-5(a) we may observe that a component with small time constant can quickly reach equilibrium with ambient temperature. Therefore, a small thermal time constant component can follow the ambient temperature more closely than a component with large time constant if the ambient is under a dynamic temperature variation. This phenomena will be demonstrated later during the case study. Since the thermal time constant is such an important parameter for determining the thermal response of a solid in a dynamic environment, followed by the

Biot number, the time constant of each component is then estimated by using Equation 6-5.

- The time constant for reference spheres:

$$\tau_{sphere} = \frac{\rho Vc}{h_c A_s} = \frac{7750 \times \frac{4}{3} \pi r^3 \times 500}{15 \times 4 \pi r^2} = 2187.2 \text{ seconds} = 36.45 \text{ minutes}$$

- The time constant for pin followers:

$$\tau_{follower} = \frac{\rho Vc}{h_c A_s} = \frac{7750 \times \pi r^2 L \times 500}{15 \times 2 \pi r L} = 410.1 \text{ seconds} = 6.84 \text{ minutes}$$

- The time constant for triangle frame:

$$\tau_{triangle} = \frac{\rho Vc}{h_c A_s} = \frac{7700 \times w^2 L \times 440}{15 \times 4 w L} = 5378.5 \text{ seconds} = 89.6 \text{ minutes}$$

- The time constant for column cylinder:

$$\tau_{column} = \frac{\rho Vc}{h_c A_s} = \frac{7700 \times (\pi r_o^2 - \pi r_i^2) L \times 440}{15 \times 2 \pi r_o L} = 2032.9 \text{ seconds} = 33.88 \text{ minutes}$$

Because most of the physical properties for fiberglass tube are not available, its time constant has to be obtained in another manner. In addition, because of the uncertainty existing in the listed physical properties, it will be better if we can verify the theoretic thermal time constant values for all components. In order to obtain the time constant for fiberglass tube and to verify the theoretical time constant value for other components, several thermal experiments have been performed.

Time Constant Verification

If the ambient temperature and the temperature on the solid component can be measured, the thermal time constant of the solid can be evaluated by using Equation 6-7. Thus we performed this experiment by measuring the ambient temperature in the

metrology laboratory where the HCMM was located. At the same time, the temperatures on the surfaces of the solids also were recorded. The thermistors used as the temperature sensors have a measurement resolution of 0.01°C . One thermal sensor was used to measure the ambient temperature. The surface temperature of solid components are taken by averaging the three thermal sensors which were placed at different surface locations. The recorded temperatures for different components are plotted in Figure 6-7 to Figure 6-9. The thermal time constant for each solid component was then evaluated by using Equation 6-7. From Equation 6-7, the temperature of the solid was estimated by plugging in the measured ambient temperature (T_{air}) and guessing a time constant (τ). The time step (Δt) in Equation 6-7 is the time interval used to record the ambient temperature which is 0.5 minute in the experiments. If the assumed time constant is close to the true value, the calculated temperature will be close to the measured temperature in the solid. By using visual comparison, the approximate time constants are 38, 85, and 35 minutes for reference sphere, triangle frame, and supporting column respectively. Comparing the experimental time constant values with the theoretical values, the difference are within 5%. We then have the confidence to use the values of the theoretical time constant for the later analysis.

When we estimated the time constant for fiberglass tube, it was assumed that the thermal system is a lumped system. Therefore, the method mentioned above can be applied. The time constant for the fiberglass tube was estimated to be 6.8 minutes as shown in Figure 6-10.

Because the pin follower was not available when the experiment was taken, its time constant could not verified.

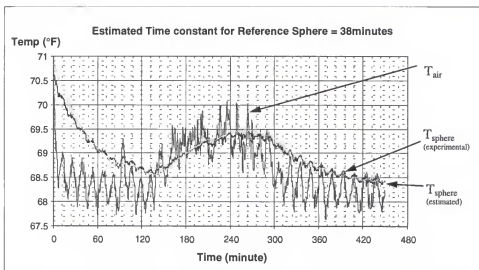


Figure 6-7 Time constant estimation for Reference Sphere

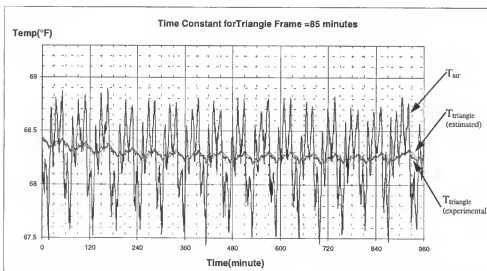


Figure 6-8 Time constant estimation for triangle frame

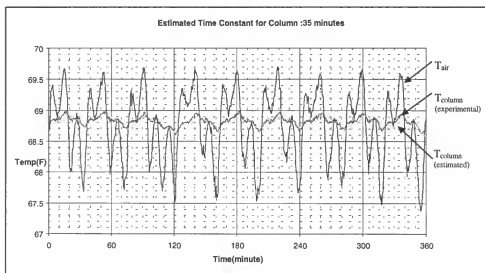


Figure 6-9 Time constant estimation for column

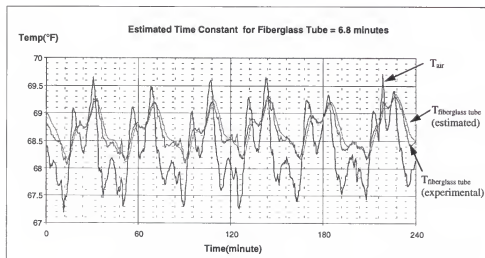


Figure 6-10 Time constant estimation for fiberglass tube

Thermal Response Under Different Thermal Cycle

Several simulations have been performed to help us understand the temperature relationship between the ambient and the thermally sensitive components of the HCMM. In our simulations, it was assumed that the initial temperature in each component is the same as the ambient. The ambient temperature then varied in a sinusoidal manner which is written as:

$$T_{air}(t) = T_o \pm \frac{D}{2} \sin\left(\frac{2\pi t}{P}\right) \quad (6-9)$$

where T_o is the initial ambient temperature, P is the temperature cycling period, and D is the amplitude of temperature variation. If the ambient temperature variation amplitude (D) and cycling period (P) are given, the temperature in each component at any moment can be calculated by using Equation 6-7. Figure 6-11 to Figure 6-14 show some of the simulation results in which the ambient is under different cycling frequency. It can be observed from these four figures that the faster the thermal cycle in ambient temperature the smaller the temperature change in solid components. This phenomena gives us the reason why in a good metrology laboratory the air temperature cycle frequency is often very fast (for instance one cycle per minute). Another conclusion which can be made for the thermally sensitive components is that the larger the time constant the smaller the temperature variation in their body.

Thermal Growth

The maximum temperature variation in a solid component can be obtained if the ambient temperature frequency and its variation amplitude (D) are given. These results are tabulated and plotted in Table 6-3 and Figure 6-15. In Table 6-3 the values given are

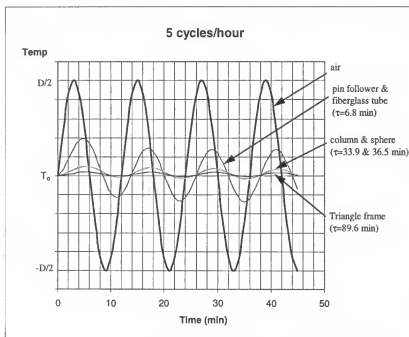


Figure 6-11 Temperature variation for 5 cycle/hour

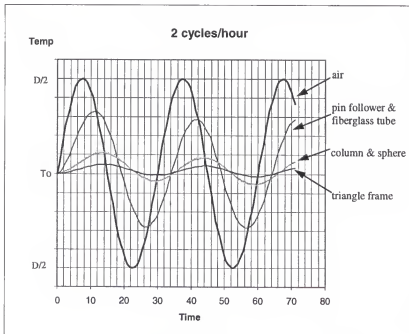


Figure 6-12 Temperature variation for 2 cycle/hour

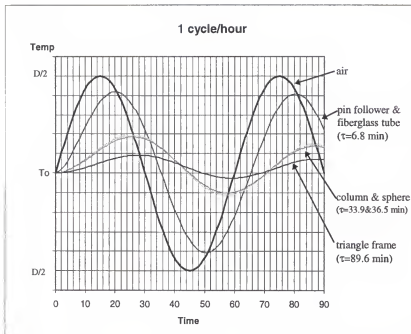


Figure 6-13 Temperature variation for 1 cycle/hour

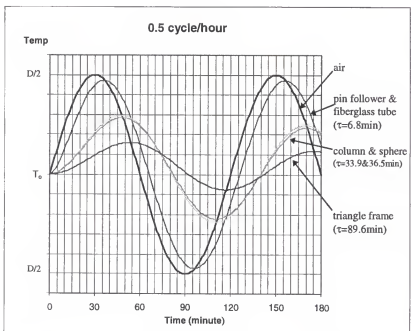


Figure 6-14 Temperature variation for 0.5 cycle/hour

Table 6-3 The maximum temperature change in components for different air temperature frequency

Temp. freq. (cycle/hr)	max(ΔT) (pin follower, fiberglass tube)	max(ΔT) (column)	max(ΔT) (sphere)	max(ΔT) (triangle frame)	Unit: °F
5	0.3067	0.0595	0.0551	0.0216	
2	0.6115	0.1561	0.1447	0.0567	
1.5	0.7466	0.2339	0.2178	0.0867	
1	0.8256	0.3072	0.2867	0.1171	
0.5	0.9429	0.5331	0.5070	0.2359	
0.25	0.9846	0.7668	0.7451	0.4352	

The values are based on the maximum ambient temperature variation, $D=1^{\circ}\text{F}$

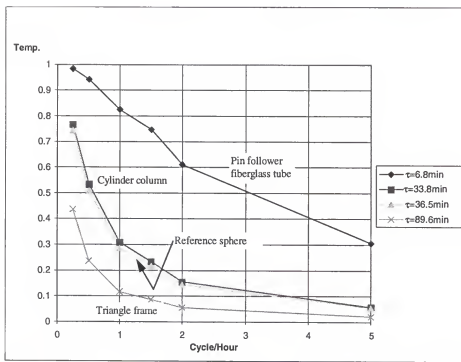


Figure 6-15 The maximum temperature change in components for different air temperature frequency

normalized against a value of $D=1^{\circ}\text{F}$. The number found in the table then, multiplied by the actual value of maximum ambient temperature variation, $D(^{\circ}\text{F})$, will give the maximum temperature for the respective components. If we assume that the temperature change in components exhibits a linear relationship with time, though this is not quite correct, the temperature rate of change in each component can be obtained by taking the maximum temperature change in the component divided by the time period of a half temperature cycle. These temperature rates of change are listed and plotted in Table 6-4 and Figure 6-16.

The maximum length change in components can be obtained by converting the maximum temperature change values in Table 6-3 by using the thermal expansion equation, Equation 6-8. The lengths or diameter used in thermal expansion calculation for fiberglass tube, pin follower, reference sphere, triangle frame, and supporting column are 33", 1", 2", 68.33" and 33.46" respectively. The thermal expansion coefficient for each component can be obtained from Table 6-1. By solving the thermal expansion equation, we have the maximum length changes in components, and their values are listed and plotted in Table 6-5 and Figure 6-17. Similarly the length changing rate in each component can be obtained by converting the values of temperature rate of change listed in Table 6-4. After performing the thermal expansion conversion, the length rate of change is tabulated in Table 6-6 and plotted in Figure 6-18.

Time Period Determination for Re-Calibration or Finishing a Part Measurement

The values of the maximum length change and the length growth rate provides us with valuable information for determining how fast we have to finish a part measurement or

how often the HCMM has to be re-calibrated before the thermal effect exceeds the allowable value.

For instance, the HCMM is placed in the metrology laboratory has an ambient temperature variation of 1.4°F and the frequency of 2 cycles per hour. If the maximum allowable thermal growth in length for the triangle frame and the supporting column is $43\mu\text{ inch}$ for each, we want to understand how long it may take for the triangle frame or the supporting column to growth more than $43\mu\text{ inch}$, such that the re-calibration process has to be performed or a part measurement has to be finished. In this case, from Table 6-5 we found the maximum length change in the triangle frame is $42.14\mu\text{ inch}$. This tells us that the length change in the triangle frame during the whole operation period will remain in the allowable range. Therefore, the re-calibration process is not necessary to for this component. For the supporting column, its maximum length change will be $56.84\mu\text{ inch}$ which is more than the allowable thermal growth of $43\mu\text{ inch}$. To find the time period for the supporting column to growth to $43\mu\text{ inch}$, one can use the length growth rate listed in Table 6-6. It will be found that the thermal growth rate in the supporting column is $3.81\mu\text{ inch/min}$ (i.e. $1.4^{\circ}\text{F} \times 2.72\mu\text{ inch/min} / ^{\circ}\text{F}$). Therefore, the time period for the supporting column to grow to $43\mu\text{ inch}$ will be 11.3 minutes. A part measurement operation therefore has to be finished in 11.3 minute. This limited operational time may be a problem for users of the HCMM. This problem can be improved by putting a thermal isolator around the surface of the supporting column which will reduce the temperature variation range inside the column, or by filling sand into the hollowed column cylinder which may increase the thermal time constant.

Table 6-4 The temperature rate of change in each component for different air temperature frequency

thermal cycle (cycle/hr)	ΔT (pin follower fiberglass tube)	ΔT (column)	ΔT (sphere)	ΔT (triangle frame)	Unit: °F/min
5	0.05111	0.00992	0.00918	0.00359	
2	0.04077	0.01041	0.00965	0.00378	
1.5	0.03318	0.01040	0.00968	0.00385	
1	0.02752	0.01024	0.00956	0.00390	
0.5	0.01572	0.00888	0.00845	0.00393	
0.25	0.00821	0.00639	0.00621	0.00363	

The values are based on the amplitude of air temperature variation, $D=1^{\circ}\text{F}$

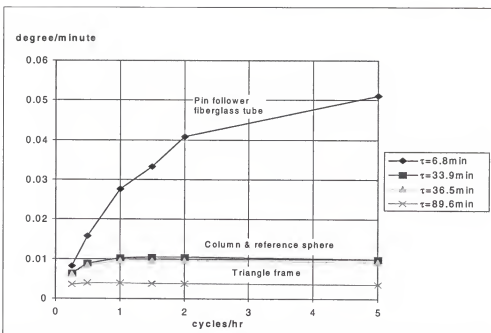


Figure 6-16 The temperature rate of change in each component for different air temperature frequency

Table 6-5 The maximum length change in components for different air temperature frequency

thermal cycle (cycle/hr)	max(ΔL) pin follower	max(ΔL) fiberglass tube	max(ΔL) column	max(ΔL) sphere	max(ΔL) triangle frame	unit: μ inch
5	2.7	231.64	15.5	1.0	11.5	
2	5.4	425.98	40.6	2.6	30.1	
1.5	6.6	520.09	60.9	3.8	46.1	
1	7.3	575.13	80.0	5.0	62.2	
0.5	8.4	656.86	138.7	9.0	125.4	
0.25	8.8	685.92	199.6	13.2	231.3	

The values are based on the amplitude of air temperature variation, $D=1^{\circ}\text{F}$

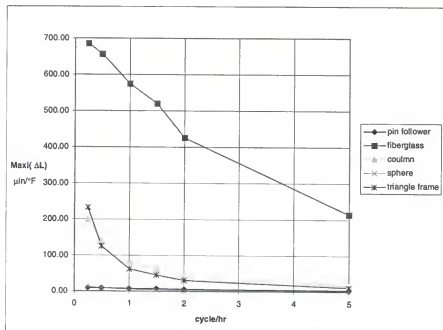


Figure 6-17 The maximum thermal growth in components for different thermal cycle with air temperature variation of 1°F

Table 6-6 The length growth rate in components for different thermal cycle rates

thermal cycle (cycle/hr)	Unit: μ inch/min				
	ΔL (pin follower)	ΔL (fiberglass tube)	ΔL (column)	ΔL (sphere)	ΔL (triangle frame)
5	0.45	35.61	2.59	0.16	1.92
2	0.36	28.40	2.72	0.18	2.01
1.5	0.30	23.12	2.71	0.18	2.05
1	0.24	19.17	2.67	0.18	2.08
0.5	0.14	10.95	2.32	0.16	2.10
0.25	0.07	5.72	1.67	0.12	1.93

The values are based on the amplitude of air temperature variation, $D=1^{\circ}\text{F}$

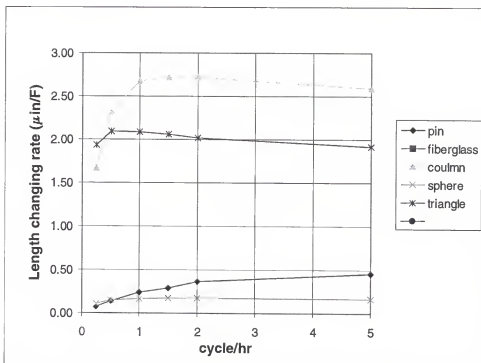


Figure 6-18 The length rate of change in components for different thermal cycle rates

The maximum Allowable Calibration Period

In the opposite way, if the allowable thermal errors in the strut length and in center rod length have been specified, one can determine the maximum allowable time period during a calibration process must be completed. It can be determined by choosing the smaller one from the following two time periods:

$$Time_{strut} = \frac{\text{allowable } \Delta L_{strut}}{\text{Strut length changing rate}}$$

$$Time_{center} = \frac{\text{allowable } \Delta L_{center\ rod}}{\text{Center rod length changing rate}}$$

For the thermal environment mentioned above, if the maximum allowable thermal error for the unsensed region in strut is 4μ inch and for the center rod length error is 20μ inch. Then the maximum allowable calibration time will be the shorter one from the following two values

$$Time_{strut} = 4\mu"/[1.4^{\circ}\text{F} \times (0.36 \times 2 + 0.18) \mu"/^{\circ}\text{F} \cdot \text{min}] = 3.17 \text{ minutes}$$

$$Time_{center\ rod} = 20\mu/[1.4^{\circ}\text{F} \times (28.40 + 0.18) \mu"/^{\circ}\text{F} \cdot \text{min}] = 30 \text{ seconds}$$

In this case the maximum allowable time period for completing a calibration procedure is 30 seconds. This time period could be too short for us to finish a calibration procedure. To prolong the time period, we suggest changing the fiberglass tube into a material that has the smallest possible thermal expansion coefficient such as Zerodur.

6.3 The Effect of the Heat Generated in Actuators

The actuators are expected to have a performance of the maximum acceleration of 64.4ft/sec^2 (or 2G's), a maximum linear speed of 20 in/sec (or 0.5m/sec), and a maximum expected load, according Mevoli [4], of 150lb (or 667N). It is known that a motor will

generate heat during operation due to the friction and electronic resistance. Thus, through heat conduction, the heat in the actuator will be transmitted to the ballscrew and the shoulder. Let us consider an extreme HCMM operation case: A constant strut extension speed of 20 in/sec (0.5m/sec) was maintained over the travel range, and the actuator was subjected to an axial load of 150lb (667N) during the entire process. Before the actuator started to function, the whole strut system had the same temperature as the ambient. Here the ambient temperature is assumed to be constant during the whole operation process. For this analysis, we assume that the motor loses 33% of its power into heat and only uses its 67% of the power to generate the strut motion. In this section we will investigate that how heat inside the motor will be transmitted to the pin followers, and result in their length changing.

A power of 333.5 Watts (N.m/sec), which is the axial load multiplied by the strut speed, has to be consumed to complete the required motion. From our assumption a heat rate of 167.5 Watts will be generated in the motor. To evaluate the temperature (or the heat) at the end of ballscrew or strut, a finite element method was used. The finite element (FE) model is made as shown in Figure 6-19. Because of the symmetric geometry in the strut, we only consider half of our investigating region. Since there is no temperature gradient along the symmetry line, the boundary condition along this symmetry line is treated as if it is insulated. Thermal convection is considered between the strut surface and the ambient, and its convection coefficient (h_c) is assumed to be 15 W/m²/°C. The transient analysis, then, was performed from time t=0 to t=20 minutes by using a commercially available FE software COSMOS/M.

The resulting temperature distributions for time=1 minute and time=20 minutes are plotted in Figure 6-20 and Figure 6-21. It can be observed that the temperature inside the motor is raised nearly by 12 °C after 20 minute's operation. The temperature history at each end of the ballscrew and the shoulder are shown in Figure 6-22 and Figure 6-23 respectively. Because the thermal convection occurred between the air and the surface of the strut, it can be expected that most of the transmitted heat from the motor will be dissipated into air before it reaches the end of the ballscrew or shoulder.

It can be observed that there is almost no temperature raise within the first four minutes. This implies that the motor's heat will not affect the pin followers length change during the calibration process if this process can be completed in 4 minutes.

6.4 Conclusion

The thermal environment is such a complicated issue that it is difficult to predict what the ambient temperature would be. In this chapter we provide a methodology for evaluating the allowable time period before the HCMM needs to be re-calibrated or a part measurement has to be finished, and how long a calibration process can last. This method is based on knowledge of the environmental conditions. In order to have this information, it is required to monitor the ambient temperature in the working area.

We also suggest to change some design parameters in the supporting column and the center rod so that the machine operation time and the calibration processing time can be prolonged.

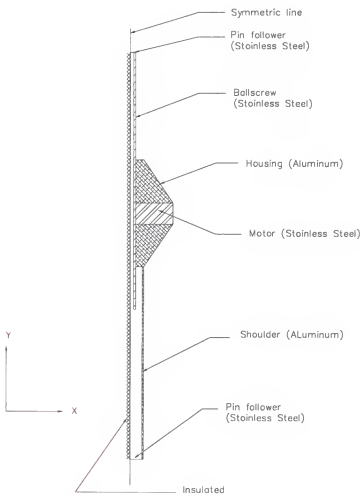


Figure 6-19 The finite element model for a strut

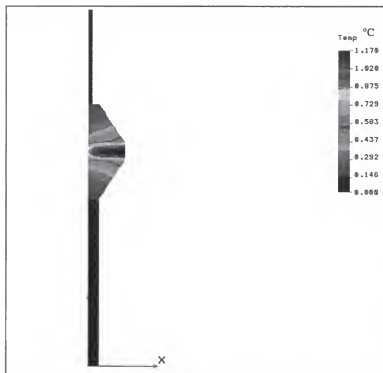


Figure 6-20 The temperature distribution in strut after the motor actuates for 1 minute

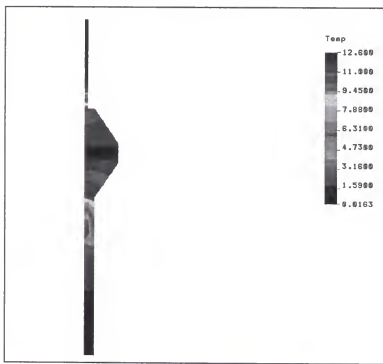


Figure 6-21 The temperature distribution in the strut when motor actuates for 20 minutes.

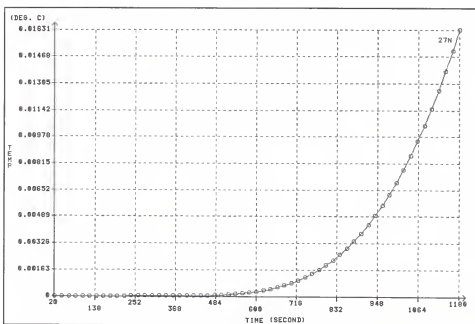


Figure 6-22 The temperature history at the end of ballscrew

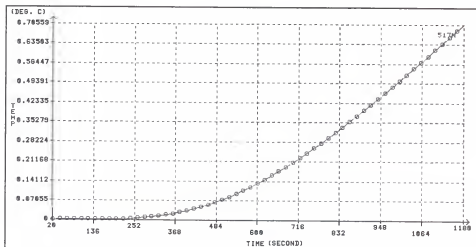


Figure 6-23 The temperature history at the end of the shoulder

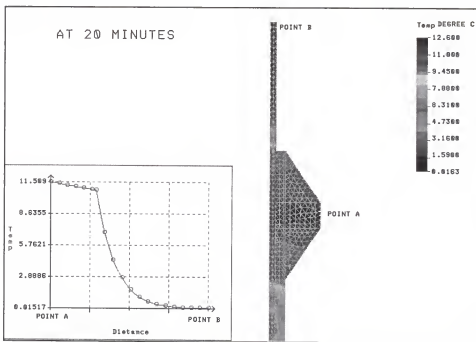


Figure 6-24 The temperature distribution along the ballscrew at $t=20$ minutes

CHAPTER 7

HCMM MEASUREMENT UNCERTAINTY ANALYSIS

In this chapter we will identify the error sources that will affect the HCMM measurement accuracy, and investigate how the error sources propagate through the mathematical model of the HCMM system to assess how they impact the probe coordinate calculations and cause errors in the measured position of the probe.

Figure 7-1 sketches the major sources that affect the determination of the probe coordinates. Three major error sources will be discussed in this chapter: linear displacement measurement error, calibration error, and thermal error. Other error sources such as the probe alignment error and the errors due to structural vibration will not be included in our investigation, since they are beyond the scope of this research.

7.1 Error Sources In Strut Displacement Measurement

Four major error sources are considered to be the contributors for the strut linear displacement measurement error:

1. Laser interferometer error
2. Spherical joint imperfection
3. Reference sphere imperfection
4. Thermal growth in the pin followers and spheres

7.1.1 Laser Interferometer Error

Three major error contributors for the laser interferometer measurement uncertainty are identified as follows,

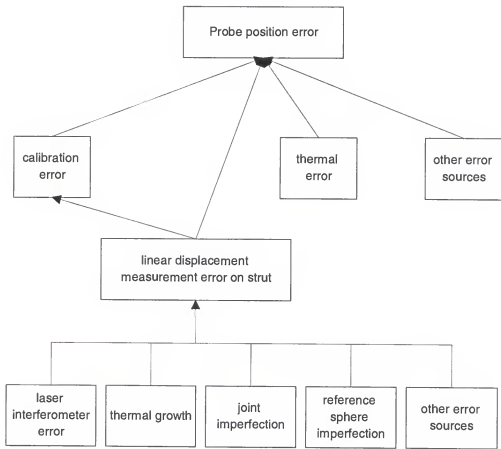


Figure 7-1 The error sources that affect the probe position determination

1. Optical component rotation
2. Refractive index error and environmental effects
3. Laser stability and intrinsic factor

Optical Component Rotation

This error comes from misalignment of the laser beam with the extension direction as a result of the rotation of the emitter and retroreflector at either end of the strut. The rotation of the optics is caused by compliance in the bearings and flexure (sag) of the strut tubes due to gravity. Figure 7-1 illustrates the optical component rotation error. According to the analysis of Mevoli [4], the strut designer, this error is between 0~2.4 μ inch (0.06245 μ m).

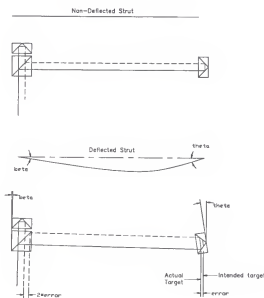


Figure 7-2 Optical component rotation error

Refractive Index Error and Environmental Effects

Temperature, pressure, humidity, and gas composition affect the refractive index of light in the measurement area. Changes in the refractive index cause a cumulative

error over the path of measurement beam. Because the vacuum system will be installed on the HCMM the strut will be evacuated. The environmental effect will be dramatically reduced. We estimate that the uncertainty caused by the refractive index error and environmental will be below the range of $\pm 1\mu\text{in}$.

Laser Stability and Intrinsic Factors

The stability of the wave length, the electrical noise error in the phase detector, and the optical components (the surface finish effects and coating property variations on the polarization beamsplitter) are inherent in all heterodyne interferometry systems. The magnitudes however are unique to particular laser systems. For the Zygō Axiom 2/20 laser system, these errors are in the range of $\pm 0.63\mu\text{ inch}$.

7.2.2 Spherical Joint Imperfection

The strut length is defined as the length between the base sphere center to the moving sphere center. If the slide motion is not parallel to the line between the two spheres, the measured strut displacement will not be correct. This error is caused by the imperfection of the spherical joint. Because of the manufacturing tolerances on joint components, installation error, and the joint deflection caused by the static or dynamic load, the spherical joint inevitably will be off center during the spherical motion. Figure 7-3 shows the linear displacement measurement error, $R-R'$, caused by the joint offset of (b,h) in the X and Y directions from the perfect joint point. To calculate the measurement error, four assumptions are made: (1) the pin follower is aligned with the laser beam, (2) the end face of the pin follower is always tangent to the reference sphere, (3) reference sphere is perfect sphere, (4) the end face of pin follower is perpendicular to its axial direction.

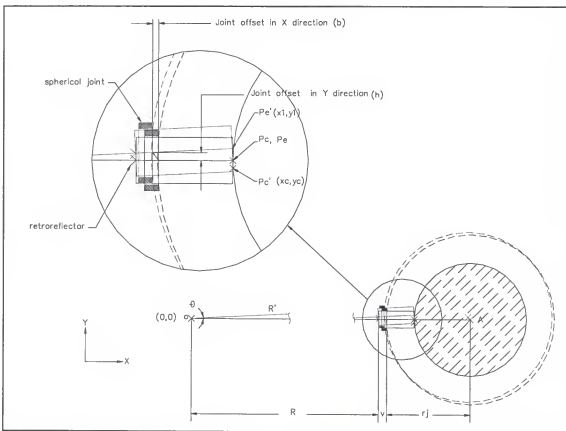


Figure 7-3 Spherical joint imperfection

The notations show in Figure 7-3 are defined as:

- O: The center of base sphere.
- R: The distance between base sphere center to retroreflector (without joint offset).
- R': The distance between base sphere center to retroreflector (with joint offset).
- r_j: The spherical joint radius
- v: The distance from spherical joint to retroreflector.
- P_c: The contact point of the pin follower on the sphere (without joint offset).
- P_{c'}: The contact point of the pin follower on the sphere (with joint offset). Its coordinate is (x_c,y_c).
- P_e: the point that the extended laser beam hits on the end face of the pin follower (without joint offset).
- P_{e'}: the point that the extended laser beam hits on the end face of the pin follower (with joint offset). Its coordinate is (x₁,y₁)

- b: The joint offset in the x direction
- h: The joint offset in the y direction.
- r: The radius of the sphere.

To find the locations of Pe' and Pc', the following four geometrical constraints are used

1. Line equation for OPe' :

$$\tan \theta = \frac{h}{R + v - b} = \frac{y_1}{x_1} \quad (7-1)$$

2. Line equation for Pe'Pc' :

$$\tan(\theta + 90^\circ) = \frac{y_1 - y_c}{x_1 - x_c} \quad (7-2)$$

3. Radius of sphere:

$$r = \sqrt{(R + v + rj - x_c)^2 + y_c^2} \quad (7-3)$$

4. Line Pe'Pc' tangents to sphere:

$$(R + v + rj - x_1)^2 + y_1^2 = \left\{ (x_1 - x_c)^2 + (y_1 - y_c)^2 \right\} + r^2 \quad (7-4)$$

For the case R=41", rj=1.5", v=0.5", r=1", b=0.03", h=0.03", the coordinates of Pc' and Pe' can be found by using Equations 7-1 to 7-4, and their locations are (42.00000026, -0.0007234147) and (41.99997779, 0.0303394976) respectively. Thus the linear displacement measurement error (R-R') caused by the joint offset of (0.03", 0.03") will be 11.26 μ inch. At different joint offset magnitudes the linear displacement measurement errors are calculated and listed in Table 7-1. From Table 7-1 it can be observed that the major measurement error is caused by the joint offset in the Y-direction (the direction normal to the line which passes through the two sphere centers). The relationship between the joint offset in Y-direction and the measurement error is plotted in Figure 7-4.

For the spherical joints we built, the measured maximum joint offset in the radial direction of the strut is 0.002 inch according to the experiments of Yeager [47]. Thus we

can very safely assume that the measurement uncertainty caused by the joint offset will be less than $0.62\mu\text{in}$ ($0.31\mu\text{in}$ for each joint).

Table 7-1 The linear displacement error caused by joint offset

joint offset (b,h) (inch)	linear displacement measure error (inch)
(0.005, 0.005)	3.10E-07
(0 , 0.005)	3.10E-07
(0.01, 0.01)	1.25E-06
(0 , 0.01)	1.25E-06
(0.03, 0.03)	1.13E-05
(0 , 0.03)	1.124E-05
(0.05, 0.05)	3.13E-05
(0 , 0.05)	3.12E-05
(0.1, 0.1)	1.25E-04
(0 , 0.1)	1.2485E-04

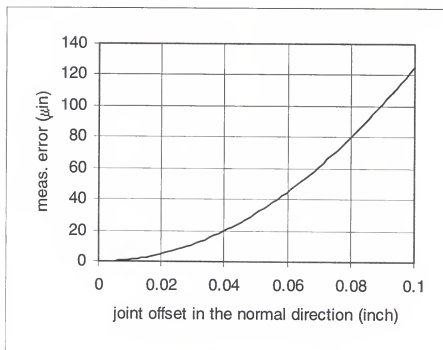


Figure 7-4 The measurement error caused by joint offset

7.1.3 Reference Sphere Imperfection

The reference sphere is similar to a master gage in that it provides a constant reference length (i.e. radius) from its surface to center. The imperfections of form (sphericity) of this sphere will cause uncertainty on the reference length. For the HCMM the Grade 8 spheres with sphericity of $8 \mu\text{in}$ were used. The sphericity is defined as the radius difference between the maximum inscribed and the minimum circumscribed spheres (as shown in Figure 7-5). The maximum reference length deviation could be $8 \mu\text{in}$. However, the region used as a reference is in an area of 60° angle, we assume the reference length deviation in this contact region will be within $\pm 4 \mu\text{in}$.

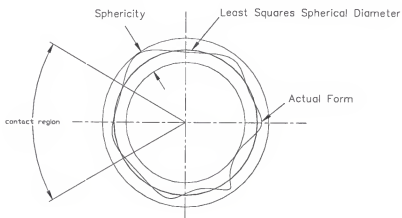


Figure 7-5 The sphericity of a sphere

7.1.4 Thermal Error

In a strut, the laser interferometer system will detect a length change from its emitter to the retroreflector, as shown in Figure 6-1. However, the thermal growth in the components (pin followers and spheres) which is not covered by the laser path will not be detected. The unmeasured thermal growth, then, will be treated as measurement error in

the strut length. The environment in which the HCMM is located has an ambient temperature frequency of 2 cycles per hour and a maximum variation amplitude of 1.4°F. From Table 6-6, the thermal growth for the unsensed region will be within $\pm 1.26 \mu\text{in}/\text{min}$ ($1.4 \times (2 \times 0.36 + 0.18)$).

Table 7-2 error sources encountered for strut linear displacement measurement

	error sources		range of error (μin)
1	Laser interferometer	Optical component rotation	0~2.4
2		Deadpath and environmental effects	-1~+1
3		Laser stability and intrinsic factor	-0.63~+0.63
4	Spherical joint imperfection		-0.62~0.62
5	Reference sphere imperfection		-8~+8
6	Thermal growth in pin followers and spheres in 1 minute		-1.26~+1.26
Error summary			-11.51~13.91

7.2 The Combined Standard Uncertainty

Suppose a measurand of interest F is related to n independent quantities x_i , $i = 1, \dots, n$. The measurand of interest F can be written as

$$F = f(x_1, \dots, x_n) \quad (7-5)$$

To determine F , the quantities x_i may be directly measured or simply estimated; in either case our state of knowledge of these quantities is described by a set of probability distributions with associated variances $\sigma_{x_i}^2$. The positive square root of these variances are called “*standard uncertainty*” of the quantities x_i . Using the Taylor expansion, the measurand of interest F can be rewritten as

$$F = F_o + \sum_{i=1}^n \frac{\partial f}{\partial x_i} \Delta x_i + \text{higher order terms} \quad (7-6)$$

where the F_o is the nominal value of F , which is obtained by plugging the nominal values of x_i into Equation 7-5. If the nominal values of x_i are close enough to true values, the higher order terms can be ignored. Thus, the error associated with the F_o can be rewritten as

$$F - F_o = \Delta F = \sum_{i=1}^n \frac{\partial f}{\partial x_i} \Delta x_i \quad (7-7)$$

Since the error of each quantity, Δx_i , is a probability distribution, the measured error of interest F must be a probability distributed quantity. In order to evaluate the quantity of ΔF , the statistical method has to be used. The expected value for the quantity of $(\Delta F)^2$ can be written as

$$E[(\Delta F)^2] = E\left[\left(\sum_{i=1}^m \frac{\partial f}{\partial x_i} \Delta x_i\right)^2\right] \quad (7-8)$$

or

$$E[(\Delta F)^2] = \sum_{i=1}^m \left\{ \left(\frac{\partial f}{\partial x_i} \right)^2 \cdot E[(\Delta x_i)^2] \right\} + 2 \sum_{i=1}^{m-1} \sum_{j=i+1}^m \left\{ \left(\frac{\partial f}{\partial x_i} \frac{\partial f}{\partial x_j} \right) \cdot E[\Delta x_i \Delta x_j] \right\} \quad (7-9)$$

where the expectations of $E[(\Delta F)^2]$ and $E[\Delta x_i^2]$ are the variances of the quantities. The expectation of $E[\Delta x_i \Delta x_j]$ is the covariance of the quantities. Thus the “*combined standard uncertainty*” of F is given by taking the positive square root of

$$u_c(F) = \sqrt{\sum_{i=1}^m \left[\left(\frac{\partial f}{\partial x_i} \right)^2 \sigma_{x_i}^2 \right] + 2 \sum_{i=1}^{m-1} \sum_{j=i+1}^m \left[\left(\frac{\partial f}{\partial x_i} \frac{\partial f}{\partial x_j} \right) \cdot \text{Cov}(\Delta x_i \Delta x_j) \right]} \quad (7-10)$$

For the HCMM, if the standard uncertainty for each of the kinematic parameters is available, the combined standard uncertainties for upper and lower sphere positions can be estimated. For instance, the upper sphere at position i in the X-direction, $X_{up}(i)$, can be written as

$$X_{up}(i) = \frac{l^2(1, i) - l^2(3, i) + r^2}{2r} \quad (7-11)$$

The combined standard uncertainty for the coordinate of $X_{up}(i)$, then can be obtained by using Equation 7-10. It can be written as

$$u_c(X_{up}) = \left[\left(\frac{\partial X_{up}}{\partial l_1} \right)^2 \sigma_{l_1}^2 + \left(\frac{\partial X_{up}}{\partial l_3} \right)^2 \sigma_{l_3}^2 + \left(\frac{\partial X_{up}}{\partial r} \right)^2 \sigma_r^2 + 2 \frac{\partial X_{up}}{\partial l_1} \frac{\partial X_{up}}{\partial l_3} \text{cov}(\Delta l_1 \Delta l_3) + 2 \frac{\partial X_{up}}{\partial l_1} \frac{\partial X_{up}}{\partial l_r} \text{cov}(\Delta l_1 \Delta l_r) + 2 \frac{\partial X_{up}}{\partial l_3} \frac{\partial X_{up}}{\partial l_r} \text{cov}(\Delta l_3 \Delta l_r) \right]^{1/2} \quad (7-12)$$

or

$$u_c(X_{up}) = \left[\left(\frac{l_1}{r} \right)^2 \sigma_{l_1}^2 + \left(\frac{l_3}{r} \right)^2 \sigma_{l_3}^2 + \left(\frac{-(l_1^2 - l_3^2)}{2r^2} + \frac{1}{2} \right)^2 \sigma_r^2 + 2 \left(\frac{l_1 l_3}{r^2} \right) \text{cov}(\Delta l_1 \Delta l_3) + 2 \left(\frac{l_1}{r} \right) \left(\frac{-(l_1^2 - l_3^2)}{2r^2} + \frac{1}{2} \right) \text{cov}(\Delta l_1 \Delta r) + 2 \left(\frac{l_3}{r} \right) \left(\frac{-(l_1^2 - l_3^2)}{2r^2} + \frac{1}{2} \right) \text{cov}(\Delta l_3 \Delta r) \right]^{1/2} \quad (7-13)$$

From Equation 7-13, we can observe that the sphere position uncertainty is dependent on the sphere's location. At different location, the strut lengths will vary, thus the combined standard uncertainty of the spheres will be different.

To determine the probe position, first the probe orientation to the center rod and the offset length between the probe tip (stylus) and the lower sphere center has to be obtained. In a conventional CMM, a probe verification procedure has to be performed before the probe can be used to make measurement. For the HCMM this procedure also is necessary prior to the measurement operation. Since the probe verification is beyond the scope of our research, here we assume that the probe is aligned and parallel with the center rod, and the distance between its stylus and lower sphere center is known as L_p .

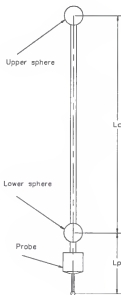


Figure 7-6 The center rod and probe

From Figure 7-6, the probe position can be expressed by the positional vector,

$$\vec{P}_{probe} = \vec{P}_{low} + L_p \cdot \frac{(\vec{P}_{low} - \vec{P}_{up})}{L_c} \quad (7-14)$$

where L_p is the length from the lower sphere center to the probe tip (stylus). L_c is the center rod length. Therefore, the X-coordinate of the probe can be written as

$$x_{probe} = x_{low} + L_p \frac{x_{low} - x_{up}}{Lc} = \left(1 + \frac{L_p}{Lc}\right) x_{low} - \frac{L_p}{Lc} x_{up} \quad (7-15)$$

Refer to Equation 7-7, the Δx_{probe} can be expressed as

$$\Delta x_{probe} = \left(1 + \frac{L_p}{Lc}\right) \sum_{i=1}^9 \left(\frac{\partial x_{low}}{\partial l_i} \Delta l_i \right) - \frac{L_p}{Lc} \sum_{i=1}^9 \left(\frac{\partial x_{up}}{\partial l_i} \Delta l_i \right) - \frac{L_p}{Lc^2} (x_{low} - x_{up}) \Delta Lc \quad (7-16)$$

where Δl_7 , Δl_8 , and Δl_9 equal to Δr , Δb , and Δh respectively. Considering the last term in Equation 7-1, if the center rod remains parallel to the Z axis (or normal to the granite table), the coordinates of X_{low} and X_{up} will be the same. Therefore, the last term can be eliminated. Equation 7-12 can be rewritten as

$$\Delta x_{probe} = \left(1 + \frac{L_p}{Lc}\right) \sum_{i=1}^9 \left(\frac{\partial x_{low}}{\partial l_i} \Delta l_i \right) - \frac{L_p}{Lc} \sum_{i=1}^9 \left(\frac{\partial x_{up}}{\partial l_i} \Delta l_i \right) \quad (7-17)$$

Thus, the variance of $(\Delta x_{probe})^2$ can be expressed as,

$$\begin{aligned} E[(\Delta x_{probe})^2] &= \left(1 + \frac{L_p}{Lc}\right)^2 U_c^2(x_{low}) + \left(\frac{L_p}{Lc}\right)^2 U_c^2(x_{up}) \\ &\quad - 2 \left\{ \left(1 + \frac{L_p}{Lc}\right) \frac{L_p}{Lc} \right\} \cdot E \left[\sum_{i=1}^9 \sum_{j=1}^9 \left(\frac{\partial x_{low}}{\partial l_i} \frac{\partial x_{up}}{\partial l_j} \Delta l_i \Delta l_j \right) \right] \end{aligned} \quad (7-18)$$

Therefore, the combined standard uncertainty for the probe position in the X direction can be obtained by taking the positive square root of Equation 7-18.

$$u_c(x_{probe}) = \sqrt{\left(\left(1 + \frac{L_p}{Lc}\right)^2 U_c^2(x_{low}) + \left(\frac{L_p}{Lc}\right)^2 U_c^2(x_{up}) \right.} \\ \left. - 2 \left\{ \left(1 + \frac{L_p}{Lc}\right) \frac{L_p}{Lc} \right\} \cdot E \left[\sum_{i=1}^9 \sum_{j=1}^9 \left(\frac{\partial x_{low}}{\partial l_i} \frac{\partial x_{up}}{\partial l_j} \Delta l_i \Delta l_j \right) \right] \right)} \quad (7-19)$$

The probe uncertainties in the Y and Z-directions can be obtained by replacing the character "X" in Equation 7-19 by "Y" or "Z". For our current HCMM design, the probe

length, L_p , is 5 inches and the center rod length is 35 inches. Therefore, from Equation 7-19, we can observe that the lower sphere position uncertainty will be the major contributor on the probe position uncertainty.

7.3 Probe Positional Uncertainty Due to Calibration Error

We performed two thousand calibration simulations by using the optimal pose set (30 poses) as listed in Appendix B. In each simulation, uniformly distributed noise (-11.51~+13.91 μ in) was superimposed on the exact strut linear displacement to simulate the measurement uncertainty. From the 2000 calibration simulation results, we plot the histograms of the identified kinematic parameter errors in Figure 7-7. It can be observed that the identified parameters are associated with an unbiased normal distribution error. To represent the standard uncertainty on each of the kinematic parameters, and to understand the covariance between the parameters, we performed the descriptive statistical data analysis by using the calibration simulation results. The variance and covariance of the kinematic parameters are listed in Table 7-3.

Table 7-3 The variance of identified parameters (m=30, optimal pose set)

	a1	a2	a3	a4	a5	a6	r	b	h
a1	2.07E-08	2.06E-08	-8.10E-09	-6.75E-09	-1.23E-09	-2.31E-09	1.24E-08	3.65E-08	4.58E-10
a2	2.06E-08	2.17E-08	-7.11E-09	-6.45E-09	1.59E-09	8.42E-11	1.30E-08	3.65E-08	3.58E-09
a3	-8.10E-09	-7.11E-09	4.48E-08	4.13E-08	-1.20E-08	-9.88E-09	3.43E-08	-3.74E-08	-5.54E-09
a4	-6.75E-09	-6.45E-09	4.13E-08	3.94E-08	-9.30E-09	-8.21E-09	3.25E-08	-3.43E-08	-3.51E-09
a5	-1.23E-09	1.59E-09	-1.20E-08	-9.30E-09	5.90E-08	5.37E-08	-1.69E-08	1.85E-09	6.08E-08
a6	-2.31E-09	8.42E-11	-9.88E-09	-8.21E-09	5.37E-08	4.99E-08	-1.61E-08	-6.66E-10	5.58E-08
r	1.24E-08	1.30E-08	3.43E-08	3.25E-08	-1.69E-08	-1.61E-08	4.50E-08	4.36E-10	-9.87E-09
b	3.65E-08	3.65E-08	-3.74E-08	-3.43E-08	1.85E-09	-6.66E-10	4.36E-10	7.86E-08	7.11E-10
h	4.58E-10	3.58E-09	-5.54E-09	-3.51E-09	6.08E-08	5.58E-08	-9.87E-09	7.11E-10	6.45E-08

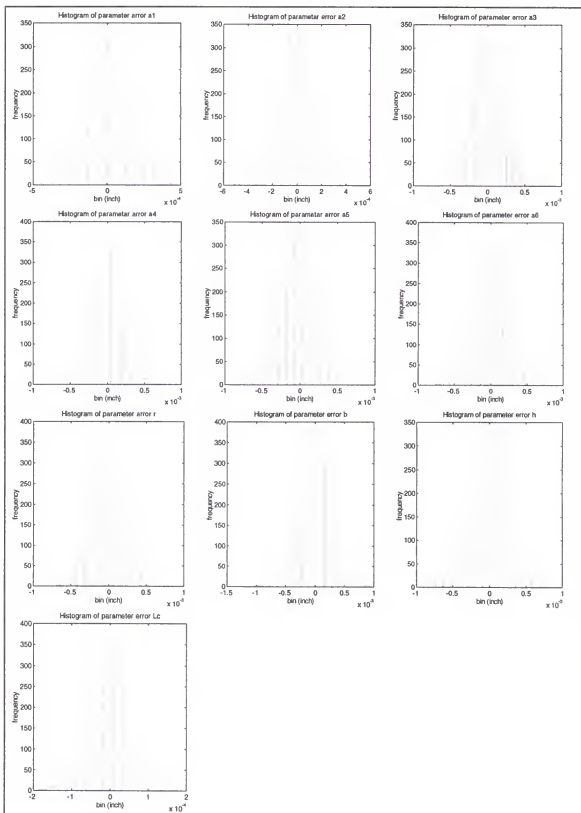


Figure 7-7 The histograms of identified parameter errors ($m=30$)

The variance and covariance in Table 7-3 provide us the necessary information for calculating the combined standard uncertainty for the probe position. As we know, the combined standard uncertainty will vary from configuration to configuration. When the center rod remains in parallel to the Z-axis, at each configuration the combined standard uncertainty for the probe can be obtained by using Equation 7-19. We searched the entire HCMM's work volume as shown in Figure 7-8, and found the maximum, minimum, and the mean positional uncertainties for the probe, as listed in Table 7-4. The combined standard uncertainties are plotted in Figure 7-9 where the probe remained in the plane of $Z=25$.

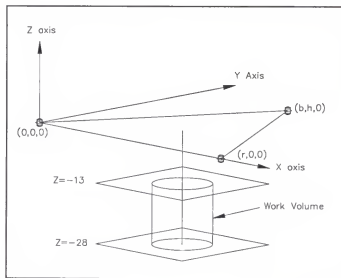


Figure 7-8 The HCMM work volume

Table 7-4 The probe positional uncertainty in the work volume due to the calibration error

	m=30			m=50		
	$u_c(\text{Probe}_x)$	$u_c(\text{Probe}_y)$	$u_c(\text{Probe}_z)$	$u_c(\text{Probe}_x)$	$u_c(\text{Probe}_y)$	$u_c(\text{Probe}_z)$
mean	166.4 μin	59.2 μin	33.9 μin	118.1 μin	46.8 μin	25.1 μin
maximum	190.3 μin	69.5 μin	45.0 μin	139.2 μin	63.9 μin	34.8 μin
minimum	147.4 μin	54.8 μin	27.4 μin	101.7 μin	39.2 μin	21.3 μin

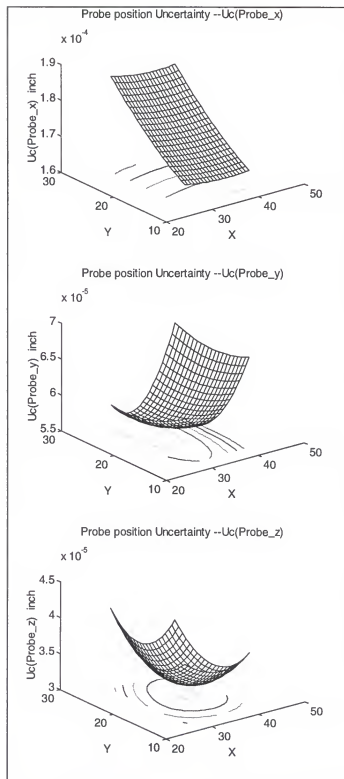


Figure 7-9 The combined standard uncertainty for probe at the level of $Z=-25$

Using the optimal pose set with 50 configurations, we repeated the above mentioned procedure, the probe's positional uncertainties in the work volume were obtained and listed in Table 7-4.

It can be observed from Table 7-4 that the Z-direction has the smallest positional uncertainty and the X-direction has the largest positional uncertainty. This results agree with the results that we have discussed in Section 5-4. For detailed explanation on this phenomena one can refer back to Section 5-4.

7.4 Probe Position Uncertainty Due to Thermal Error and Strut Displacement Measurement Error

In the metrology laboratory where the HCMM is placed, the environment has an ambient temperature variation of 1.4°F and the frequency of 2 cycles per hour (30 minutes a cycle). The maximum thermal growth of the triangle frame is $42.21 \mu\text{in}$. Thus the HCMM's kinematic parameter "r" will be subjected to a range of error within $\pm 42.21 \mu\text{in}$. For the default values, the parameters "b" and "h" will be $1/2$ and $\sqrt{3}/2$ times of the value of "r." For a uniformly distributed quantity within a range of $\pm D$, the standard uncertainty will be $D/\sqrt{3}$ (see Taylor [42]). Therefore, the variance for r , b , and h will be $(42.21 \times 10^{-6})^2 / 3$, $\left(42.21 \times 10^{-6} \times \frac{1}{2}\right)^2 / 3$, and $\left(42.21 \times 10^{-6} \times \frac{\sqrt{3}}{2}\right)^2 / 3$ respectively. Since the variations in r , b , and h are dependent on the ambient environment, these three parameters must be completely correlated with each other. The covariance between the (r, b) , (r, h) , and (b, h) then can be written as $\left(\frac{D}{\sqrt{3}} \times \frac{D}{2\sqrt{3}}\right)$, $\left(\frac{D}{\sqrt{3}} \times \frac{\sqrt{3}D}{2\sqrt{3}}\right)$, and $\left(\frac{D}{2\sqrt{3}} \times \frac{\sqrt{3}D}{2\sqrt{3}}\right)$ respectively, where D is the value of 42.21×10^{-6} . The strut linear displacement

measurement error has been discussed in Section 7-1. Here we will use the results in Table 7-2, except the value for thermal error in the pin followers and the spheres is $18.9 \mu\text{in}$ which is the maximum undetected thermal growth in the strut. The error range in the strut displacement measurement then will be within $\pm 31.55 \mu\text{in}$. Thus the standard uncertainty for each strut will be $31.55 \times 10^{-6} / \sqrt{3}$. Therefore, the variance for each strut will be 3.32×10^{-10} . Since there are many error sources which contributed to the strut displacement measurement, it will be very difficult to determine the correlation between struts. Though we know the correlation exists, the covariance between struts, for simplicity, was assumed to be zero which means the error in each strut is independent from the other. The zero covariance assumption between the base sphere length and the strut length was made for the same reason. The variance and covariance between the HCMM's kinematic parameters are then listed in Table 7-5.

Table 7-5 The variance and covariance between kinematic parameters

	l_1	l_2	l_3	l_4	l_5	l_6	r	b	h
l_1	3.32E-10	0	0	0	0	0	0	0	0
l_2	0	3.32E-10	0	0	0	0	0	0	0
l_3	0	0	3.32E-10	0	0	0	0	0	0
l_4	0	0	0	3.32E-10	0	0	0	0	0
l_5	0	0	0	0	3.32E-10	0	0	0	0
l_6	0	0	0	0	0	3.32E-10	0	0	0
r	0	0	0	0	0	0	5.939E-10	2.969E-10	5.143E-10
b	0	0	0	0	0	0	2.969E-10	1.485E-10	2.572E-10
h	0	0	0	0	0	0	5.143E-10	2.572E-10	4.454E-10

From Table 7-5 we have the necessary information for determining the probe's positional uncertainty. By using Equation 7-19, we searched the HCMM's work volume, and the maximum, minimum, and the mean positional uncertainties for the probe were listed in Table 7-6. We observed that the maximum positional uncertainty is in the Z-

direction. Unlike the results caused by the calibration error as shown in Table 7-4, the kinematic parameters in this case do not provide a special relationship to minimize the deviation for the center rod length. The Z-coordinate then accumulates the uncertainties from X- and Y-coordinate, thus in the Z-direction will have the largest positional uncertainty.

Table 7-6 The combined standard uncertainties for the probe position due to the thermal error and strut linear displacement measurement error

	$u_c(\text{Probe_x})$	$u_c(\text{Probe_y})$	$u_c(\text{Probe_z})$
mean	23.3 μin	20.3 μin	62.9 μin
maximum	26.5 μin	24.0 μin	99.6 μin
minimum	20.6 μin	17.1 μin	36.6 μin

In Figure 7-10 we observed that the probe's positional uncertainty in X-coordinate, $u_c(\text{probe_x})$, declines when the probe moves away from the Y-axis. To explain this phenomena, we have to refer back to the lower sphere positional uncertainty because the probe positional uncertainty is mainly determined by the uncertainty of the lower sphere. By modifying the Equation 7-13, the lower sphere positional uncertainty in X-coordinate can be written as

$$u_c(X_{\text{low}}) = \left[\left(\frac{l_2}{r} \right)^2 \sigma_{l_2}^2 + \left(\frac{l_4}{r} \right)^2 \sigma_{l_4}^2 + \left(\frac{-(l_2^2 - l_4^2)}{2r^2} + \frac{1}{2} \right)^2 \sigma_r^2 + 2 \left(\frac{l_2 l_4}{r^2} \right) \text{cov}(\Delta l_2 \Delta l_4) + 2 \left(\frac{l_4}{r} \right) \left(\frac{-(l_2^2 - l_4^2)}{2r^2} + \frac{1}{2} \right) \text{cov}(\Delta l_2 \Delta r) + 2 \left(\frac{l_4}{r} \right) \left(\frac{-(l_2^2 - l_4^2)}{2r^2} + \frac{1}{2} \right) \text{cov}(\Delta l_4 \Delta r) \right]^{1/2} \quad (7-20)$$

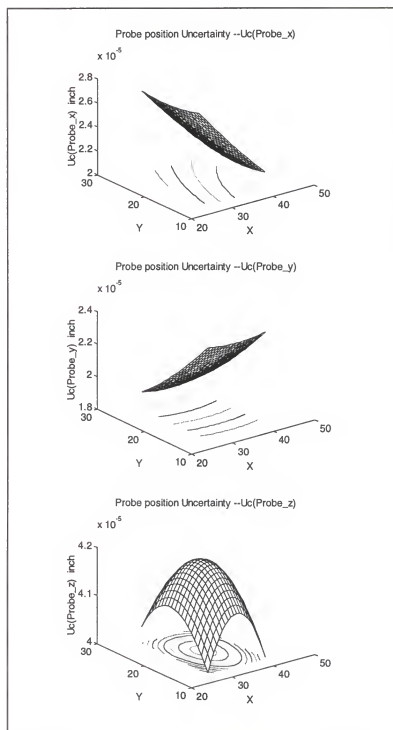


Figure 7-10 The combined standard uncertainty for probe due to the thermal error and strut displacement measurement error (the probe at the level of $Z=25$)

In Equation 7-20, the terms with covariance can be eliminated since there is no covariance between the parameters of l_2 , l_4 , and r . From Table 7-5 we know that $\sigma_{l_2}^2 = \sigma_{l_4}^2$ and $\sigma_r^2 = 1.79 \sigma_{l_2}^2$. Then, Equation 7-20 can be written as

$$u_c(X_{low}) = \left[\left(\frac{l_2}{r} \right)^2 \sigma_{l_2}^2 + \left(\frac{l_4}{r} \right)^2 \sigma_{l_2}^2 + 1.79 \left(\frac{(l_4^2 - l_2^2)}{2r^2} + \frac{1}{2} \right)^2 \sigma_{l_2}^2 \right]^{1/2} \quad (7-21)$$

Without the last term in Equation 7-21, one can observe that the combined standard uncertainty in the lower sphere in X-coordinate will show symmetry to the plane of $X=34.1$, as shown in Figure 7-11. When the last term in Equation 7-21 was considered, we observed that the closer the probe to the Y-axis, the larger the magnitude in the last term. This is the reason why we found the probe's positional uncertainty in the X-coordinate declines when the probe moves away from the Y-axis.

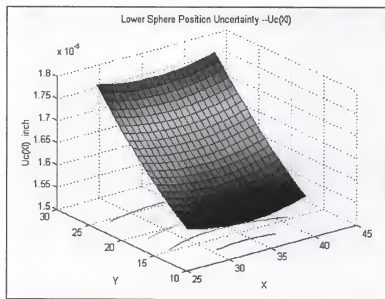


Figure 7-11 The lower sphere positional uncertainty without the last term in Equation 7-21

Probe Positional Uncertainty Due to Cylindrical Column

It is known that the thermal growth in the cylindrical column will be directly added onto the probe measurement error in the Z-direction, but not through the error propagation procedure. From Table 6-5, the maximum thermal growth in the column is 56.84 μin under the ambient temperature frequency of 2 hour per cycle and the variation amplitude of 1.4°F. Therefore, the standard uncertainty of the probe measurement in the Z-direction due to the thermal growth in the cylindrical column will be 32.81 μin .

7.5 The Overall Probe Positional Uncertainty

In the previous sections we investigated the probe positional uncertainty due to three major error sources. What would be the overall combined standard uncertainty for the probe? Here we will discuss two extreme cases:

1. These three sources of uncertainty are independent each other.
2. These three sources of uncertainty are hundred percent correlated.

For the first case the overall combined standard uncertainty can be obtained by taking the square root of the sum of the squares of each individual standard uncertainty (RSS) as shown in following equation:

$$U_c = \sqrt{u_1^2 + u_2^2 + u_3^2} \quad (7-22)$$

For the second case the combined standard uncertainty for the probe would be the sum of each individual standard uncertainty:

$$U_c = u_1 + u_2 + u_3 \quad (7-23)$$

As we know, the overall probe combined standard uncertainty must stay within the two boundaries. Thus, the overall combined standard uncertainty for the probe

position is determined by taking the average of RSS and the individual sum. In Table 7-7, we listed the worst case of each individual uncertainty sources. From Table 7-7 we observed that the probe Y-coordinate has the smallest positional uncertainty and the X coordinate has the largest uncertainty. To improve the probe's positional uncertainty, one can either improve the hardware so that calibration uncertainty could be reduced, or re-calibrate the kinematic parameter when the thermal growth is too big.

Table 7-7 The uncertainty budget for probe position

sources of uncertainty		$u_c(\text{Probe}_x)$ (μin)	$u_c(\text{Probe}_y)$ (μin)	$u_c(\text{Probe}_z)$ (μin)
1	Calibration (for $m=30$)	190.3	69.5	45
2	Thermal growth in triangle frame & strut linear displacement measurement	26.5	24	99.6
3	Thermal growth in cylindrical column	0	0	32.8
Sum		216.8	93.5	177.4
RSS		192.1	73.5	114.1
Average(Sum+RSS)		204.45	83.5	145.75

It has to be noted that the results shown in Table 7-7 is based on the worst case, operation in the metrology laboratory, and no re-calibration procedure. To obtain the probe's positional uncertainty for different ambient environments, one can follow the procedures we have performed from Sections 7-1 to 7-5.

CHAPTER 8 CONCLUSIONS AND FUTURE WORK

8.1 Conclusions

A self-calibration methodology for a hexapod coordinate measuring machine has been developed. It was found that the self-calibration technique is very sensitive to the strut linear displacement measurement noise. It has been shown that the calibration simulation results are linearly decreased with the increase of the strut displacement measurement uncertainty.

To minimize the effect of inevitable measurement noise on the results of estimation, the selection of measurement configuration becomes very important. Thus, the condition number was used to be the index to quantify the goodness of pose selection.

A procedure to determine the time period that the HCMM needs to be re-calibrated or a part measurement has to be completed has been demonstrated. The combined standard uncertainty analysis has been performed to evaluate the HCMM's measurement uncertainty.

8.2 Future Work

Several tasks will need to be continually performed in order to build a successful machine. First, the methodology for verifying the probe alignment has to be developed. This will avoid the error source come from the probe misalignment from the center rod.

Second, the methodology for verifying the HCMM accuracy needs to be established.

This procedure will be used to confirm the theoretical analysis results as shown in

Chapter 7. Third, improving the center rod design is necessary so that the thermal growth in the center rod during the calibration procedure can be minimized. Forth, the structural dynamic analysis has to be performed so that operation of the machine at the speed of its natural frequency can be avoided.

APPENDIX A OBSERVABILITY INDICES

Minimum Singular Values and Observability Index

For a closed loop kinematic like that of the HCMM, the linearized error function can be written as $\underline{e} = J\underline{a}$. From matrix norm basics one can derive the following ratio:

$$\sigma_r \leq \frac{\|\underline{e}\|}{\|\underline{a}\|} \leq \sigma_1$$

where σ_r and σ_1 are the minimum and maximum singular of matrix J . It is desired that small errors in \underline{a} will make a largest effect on the residual error function of \underline{e} . Thus we wish to make $\|\underline{e}\| / \|\underline{a}\|$ as big as possible. This implies that the bigger the smallest singular value σ_r , the larger the sensitivity.

From a geometrical point of view, if we assume that \underline{a} defines a hypersphere with a unit radius, then \underline{e} is a hyperellipsoid whose semi-axes are the singular values of J . Thus the geometric rationale is to make the volume of the hyperellipsoid as big as possible. Borm and Meng [14] prove that the volume is proportional to the value as follows:

$$obi = \frac{\sqrt{\sigma_1 \times \sigma_2 \times \dots \times \sigma_r}}{\sqrt{m}}$$

where obi is the observability index and m is the number of poses.

Noise amplification Index

This number is the combination of condition number and minimum singular value which is given as

$$O_n = \frac{\sigma_r}{\text{cond}(J)} = \frac{\sigma_r^2}{\sigma_1}$$

Nahvi and Hollerbach [16] claimed that this index is more sensitive than the other three indices.

APPENDIX B
OPTIMAL POSE SETS

The optimal pose set for m=30

pose	dl.1	dl.2	dl.3	dl.4	dl.5	dl.6
1	-1.56946870230964	-10.971187622721160	-2.03219403359106	8.38011305176563	1.092228684337549	5.610989699930111
2	4.9596780303644	-9.88087278766640	-1.90856620594539	0.74747908172604	5.36408638858184	2.97368696747244
3	5.46963677473694	-3.47953012504334	-5.02267994209825	-7.56143943316316	8.34989749511979	7.09434045081071
4	-4.88460533138849	0.15869601894187	0.34117086546460	-0.23407387336875	1.27650229509333	4.22854577225843
5	8.48317320550261	-10.0556978402160	-3.13154912848325	1.43194520022062	4.33248128857567	1.03278291368898
6	-9.88468867844206	8.8089664397806	3.24085012230277	1.959106171240848	7.689246192925	
7	3.821881851050831	3.101619934651	5.35384913165524	-7.4257149945168	8.626620176123711	-4.5803245258941
8	8.42812181185549	2.86802738971250	-3.33814113656550	4.55108459036442	-10.16708089048050	1.5949738663392961
9	-5.787024931330385	8.73675595290192	0.62925551664522	-4.09809144287130	-0.31906584948950	1.051042632583867
10	2.03619171424300	-0.62384536243574	-10.20789471749540	-0.09627120793218	5.07247127135578	5.98323020659436
11	-8.12420494030494	6.81750665028141	-2.97073069842498	8.813638919580021	4.33618861169826	-9.73526261976572
12	7.58816107610106	-8.05164591517488	4.77527305412185	0.08319528308532	5.82459931941524	-1.804443038854455
13	-5.95607727711694	4.6229833885360908	1.159282562338647	0.28555758875192	6.011245376252506	-7.651736667499232
14	4.52329793992280	2.63709121703837	-3.56411556134209	8.02609991641007	-9.32659103821127	4.218017996258408
15	-8.05746878996701	5.93709697344169	5.564117731468906	2.844586194824	5.660321961712908	2.93555130467421
16	-3.77605181120065	6.44773095657865	-10.69467347896400	7.7406102526470	5.82400124722320	3.08129017855333
17	-2.85958235277175	6.00275721641821	-1.5613240529987212	5.7416706079793	-5.39039248519100	6.07739022264775
18	-2.03071759085706	5.12584541598144	-4.40886029323822	0.11544928832099	3.931790824518818	-2.87450217323991
19	3.20945706397681	4.16454422464751	6.51458575073390	2.29774614873738	-6.75984483893489	-7.08894398788289
20	-9.48857889397843	6.08595412759256	8.43439009165903	-10.54521102115900	-3.99151581901780	6.49087008100819
21	-1.9641281725247	-5.04920979064054	6.55755606485388	4.927761819620496	-7.534459808868875	4.57352170572100
22	1.86185447852847	-2.19488186729972	8.48115405299761	-4.57714770578837	-1.53926652991373	-0.1051447457887
23	-2.85986628507582	4.38108496021906	-9.39128997442812	7.61519858552490	3.46252646855591	3.13012129823933
24	6.20330050718740	-5.12712815407925	2.48312002953296	6.77245340250087	-10.91473276111090	0.69267160655584
25	-5.24896564615081	1.08881985762799	0.70517240924951	-2.74559464882229	8.47674609954295	-2.13242066288339
26	-5.24898654960229	-8.66536517264430	8.845611928281651	6.6136019304121	4.57030554712891	-1.26593941470860
27	0.77092888355894	7.42023403083312	4.89324393425682	1.28326707261450	-2.67305260199416	-10.01080592186520

28	0.88856772878297	2.15925761815027	-3.70540370841393	-8.66801494663042	5.82325143604901	5.85225578705575
29	-6.45818579153963	0.55828260898742	-3.85749309524815	8.67798999723331	7.81920229219433	-8.92927540195881
30	-6.34366164072204	4.59944318532562	1.95372855074769	4.95232234251105	4.19399453622588	-10.78136233222780

The optimal pose set for m=50.

poses	dl_1	dl_2	dl_3	dl_4	dl_5	dl_6
1	8.48317320550261	-10.05569784020160	-3.13159192848325	1.43194520022062	4.33248128857567	1.03278291368898
2	-8.19483127257088	-9.88488867844206	8.808986643977606	3.24020512230277	1.95910617240848	7.68922465192825
3	3.82188188150831	3.10161197034651	3.538493921553524	-7.42574149945168	8.62620176123711	-4.5803245588491
4	8.42812181185549	2.86802738971250	-3.338141136555650	4.55108459036442	-10.16708089048050	1.59497386639262
5	-5.78702493133035	8.73675598290192	0.62925551664522	-4.09809144287130	-0.31906584948950	1.05104263258367
6	2.03619171424300	-6.62384536243574	-10.20789471749540	-0.09627120793218	5.07421712713578	5.9832302659436
7	-8.12420494030494	6.81806650281481	-2.9770369842498	8.61361985158021	4.33616861169826	-9.73526261976572
8	7.56816107610106	-8.05164591517488	4.7757237051412185	0.0831928308532	5.82459381941524	-1.8044303885445
9	-5.95607727771694	4.62983885360908	1.15928256233647	0.28555758575192	6.01124537625506	-7.65173664799232
10	4.5232979399260	2.63709121703837	-3.5641156134209	8.02609891641007	-9.32659103821127	4.21801996258408
11	-8.05746578396701	8.42019697344169	5.93117736146906	1.29456161518434	-5.66032196172908	2.93555130467421
12	-3.777605181120065	6.447730395657865	-10.69467347896400	7.74060102526470	5.8240124722320	3.08129017855335
13	-2.85658235327175	6.00275721641821	-1.5613240898987212	5.74167060079793	-5.39093248519100	6.07739022264775
14	-2.03071759088706	5.125684541599144	-4.408860929323822	0.11544928532099	3.93790824518818	-2.87450217323991
15	3.20945706297681	4.164442246751	6.51548611487329	-6.75984938448989	-7.08894398788289	
16	-9.48857889397843	1.08855412759256	8.434390091165903	-5.504521102115900	-3.99151581901780	6.49087008100819
17	-1.9641281732247	-5.04920979064054	6.55755606485388	4.92761819620496	-7.534459808868875	4.57352170572100
18	1.86185447852847	-2.19488186729972	8.48115405299761	-4.57714770578837	-1.53926629991373	-0.105144747557887
19	-2.83986628501582	4.3810849621906	-9.39128997442812	7.61519858352490	3.46252646855591	3.13012129823933
20	6.20330050718740	-5.12712815407925	2.48312002953296	6.77245340250087	-10.9147327611090	0.69267160655584
21	-5.24896564615081	1.088819885762799	0.70517240924951	-2.74559464682229	8.47674609954295	-2.132424066228839
22	-5.2890865496229	-8.66536517264430	8.84561193281651	6.61360193004121	4.57030554712891	-1.26593941470860
23	0.77092888358894	7.42023403083312	4.89324393425682	1.28332670261450	-2.6790526019944	-10.01080592186520
24	0.88856772878297	2.15925761815027	-3.70504370841393	-8.668014946633042	5.82325143604901	5.8522559787056575
25	-6.45818579153963	0.55828260898742	-3.85749309524815	8.67798999723331	7.81920229219433	-8.929275401956881
26	-6.34366164072204	4.5894318532562	1.95372855074769	4.9323234251105	4.193994536225588	-10.7813623222780
27	8.07134406279269	3.89176533205741	-4.49550053324507	-3.11058298346726	-9.15180105150676	8.26946821772319
28	3.52776552988953	-8.06813376009749	4.6556956383630	-2.26993273274031	7.74425712731755	-0.605455536474
29	-4.67803679649961	2.04924829575367	5.85988767683122	-2.0261641142842	-7.63015350792843	7.819791165670

30	-9.07720528116326	-2.9744425807187	3.55161015645608	0.53819167641183	6.833663737472377	2.58206512412164
31	2.77668656681032	5.74752960015673	0.88417827780889	0.70294246654680	-9.7816048963698	2.78008195944289
32	-5.403469011456801	-0.10351547240421	5.5892906907581	-3.82747839277994	2.38842040469847	1.28133555637011
33	3.12625551289600	1.533102311495756	2.8930944176257	5.92495400775656	-9.72748107450326	-1.31211912635332
34	3.63072758410258	-10.256882432649420	1.92378388716792	5.72847467031089	0.37846426266355	-0.03097871879673
35	2.82701545758787	4.34214457148986	-6.37218885295345	5.55554654032199	-0.79077763319096	-4.79185733858562
36	-3.05770222465052	4.114919288679959	8.72421866210792	-9.4648081251173	4.95892305048828	-2.69498285282097
37	8.63153761463146	7.626275381945874	4.4197706380865	2.16236655270415	-7.05795098162326	-10.70122299628240
38	5.94323671660205	4.1506350744626	-0.3132234930	5.39974327851020	-3.70179133202774	
39	7.33536491651963	-10.39933063535009	-5.233722767141232	5.23370825226119	0.98755634384496	0.56537104395559
40	8.63755876107611	2.41594481759633	-7.17743024750542	1.461732617191541	-6.76189362676866	5.21578708596460
41	-9.11627611583938	-0.45841624716430	0.32082982403950	8.128908898082425	8.21892784464591	-8.16057729696232
42	1.39365014816510	-5.458986868699441	3.65408371755573	7.43201462603341	-3.87113867329775	-1.91770255357801
43	-10.390533937162500	-9.96685270168080	6.8083234964649	8.70085003798033	8.65689099844832	1.38504721571907
44	-1.88208871021662	-4.00169401356191	-7.81890844824372	7.51455698100750	4.43387226645295	2.83984904446332
45	-10.154719010305400	5.38286875306210	-5.08911670352608	2.91407288606916	8.89005428053926	8.81853921140326
46	-1.62228832468382	5.84165269323344	2.55417586206644	-4.1077253120549	6.26596927049075	-7.703509090796327
47	-3.54087397374167	-10.0098244365190	-3.84324903921971	8.80301773740801	2.439722166296	8.32276477851142
48	2.79622408785244	1.206437312388636	4.25292753138987	0.72274362460670	-8.44782495434031	-0.0171875585477
49	6.227178458893	6.61100940330512	-6.10132692266399	-3.962428017723581	8.369719686860596	-7.97017229720518
50	5.69600865277603	7.60754807667913	2.41351133993192	-9.85748149821040	2.05639173101659	-3.10829053759198

APPENDIX C MATLAB COMMAND FILES

The Non-Linear Least-Squares Methods

```
%% 1. The objective is to calibrate the HCMM's kinematic parameters using a
%% linearized least-squares method.
%% 2. The Jacobian Matrix [J] was calculated by using the analytical deviation.
%% 3. The input information:
%%     x: the initial guess for kinematic parameters; size (1x10)
%%     m: number of poses used in calibration; size (1x1)
%%     s: the strut displacement data; size (6xm)
%% 4. The output data:
%%     a: the identified kinematic parameters; size (1x10)
%%     J: the Jacobian matrix; size (mx10)
```

```
function [a,J,jump]=hcmm_nls(x,m,s)

count=1;

n=length(x);

%%%% r=a(7) %%%
%%%% b=a(8) %%%
%%%% h=a(9) %%%
%%%% d=a(10) inital guess for center rod length%%%%

repeat=1;
stop=1;
err_old=1e10;

change_a5=0;
change_a6=0;
jump=0;

adpt1=1; adpt2=1;

while repeat ==1 %% preventing a negative in square root %%
a=x;
if change_a5==1
    a(5) = a(5)+0.2*adpt1; %increase a5 to prevent negative sqrt(-)
elseif change_a6==2
    a(6) = a(6)+0.2*adpt2;
end
change_a5= 0; change_a6=0;
```

```

while stop==1, %% stop iteration if max(abs(dphi)) < 1e-12 %%
if jump > 10 %% automatically adjust the initial values of a5 & a6 for 10 times
    repeat=0;
    stop=0;
    break
end
for k=1:m;

Xu(k)= ( (a(1)+s(1,k))^2-(a(3)+s(3,k))^2+a(7)^2)/(2*a(7));
Xi(k)= ( (a(2)+s(2,k))^2-(a(4)+s(4,k))^2+a(7)^2)/(2*a(7));
Yu(k)= ( (a(3)+s(3,k))^2 - (a(5)+s(5,k))^2 + 2*Xu(k)*(a(7)-a(8))-(a(7)^2-a(8)^2-a(9)^2)) / (2*a(9));
YI(k)= ( (a(4)+s(4,k))^2 - (a(6)+s(6,k))^2 + 2*Xi(k)*(a(7)-a(8))-(a(7)^2-a(8)^2-a(9)^2)) / (2*a(9));
adj11= (a(1)+s(1,k))^2 - Xu(k)^2 - Yu(k)^2 ;
adj21= (a(2)+s(2,k))^2 - Xi(k)^2 - YI(k)^2;
if adj11 > 0
    uuuuz=adj11;
else
    test1=adj11; %% →the following steps are used to automatically adjust the initial --- ↓
    change_a5=1; % values to prevent the negative value in the square root of Z
    adpt1=adpt1+1;
    err_old=1e10;
    jump=jump+1;
    break
end

if adj21 > 0
    lllz=adj21;
else
    test2=adj21;
    change_a6=2;
    adpt2=adpt2+1;
    err_old=1e10;
    jump=jump+1;%automatically adjust the initial value if negative values appear in adj11&2
    break % -----↑
end

Zu(k)= sqrt(uuuuz );
ZI(k)= -sqrt(lllz );
Lc(k)= sqrt( (Xu(k)-Xi(k))^2 + (Yu(k)-YI(k))^2 + (Zu(k)-ZI(k))^2);
F(k)=Lc(k)^2-a(10)^2;
errorF(k)= 0.-F(k);
end
if jump > 10
    repeat=0;
    stop=0;
    break
end
if change_a5 +change_a6 > 0
    break
end

err(count)=errorF*errorF'; % Objective value
a_old=a;
%% Take the derivative of F
for k=1:m

```

```

Xu_a1(k)=(a(1)+s(1,k))/a(7);
Xu_a2(k)=0;
Xu_a3(k)=-(a(3)+s(3,k))/a(7);
Xu_a4(k)=0;
Xu_a5(k)=0;
Xu_a6(k)=0;
Xu_r(k)=-0.5*((a(1)+s(1,k))^2-(a(3)+s(3,k))^2)/a(7)^2+0.5;
Xu_b(k)=0;
Xu_h(k)=0;

Xl_a1(k)=0;
Xl_a2(k)=(a(2)+s(2,k))/a(7);
Xl_a3(k)=0;
Xl_a4(k)=-(a(4)+s(4,k))/a(7);
Xl_a5(k)=0;
Xl_a6(k)=0;
Xl_r(k)=-0.5*((a(2)+s(2,k))^2-(a(4)+s(4,k))^2)/a(7)^2+0.5;
Xl_b(k)=0;
Xl_h(k)=0;

Yu_a1(k)=(a(7)-a(8))/a(9)*(Xu_a1(k));
Yu_a2(k)=0;
Yu_a3(k)=a(8)/a(9)*Xu_a3(k);
Yu_a4(k)=0;
Yu_a5(k)=-(a(5)+s(5,k))/a(9);
Yu_a6(k)=0;
Yu_r(k)=Xu(k)/a(9)-a(7)/a(9)+(a(7)-a(8))/a(9)*(Xu_r(k));
Yu_b(k)=-Xu(k)/a(9)+a(8)/a(9);
Yu_h(k)=-0.5*((a(3)+s(3,k))^2 - (a(5)+s(5,k))^2 + 2*Xu(k)*(a(7)-a(8))
               -(a(7)^2-a(8)^2))/a(9)^2+0.5;

Yl_a1(k)=0;
Yl_a2(k)=(a(7)-a(8))/a(9)*(Xl_a2(k));
Yl_a3(k)=0;
Yl_a4(k)=a(8)/a(9)*Xl_a4(k);
Yl_a5(k)=0;
Yl_a6(k)=-(a(6)+s(6,k))/a(9);
Yl_r(k)=Xl(k)/a(9) - a(7)/a(9) +(a(7)-a(8))/a(9)*(Xl_r(k));
Yl_b(k)=-Xl(k)/a(9)+a(8)/a(9);
Yl_h(k)=-0.5*((a(4)+s(4,k))^2 - (a(6)+s(6,k))^2 + 2*Xl(k)*(a(7)-a(8))
               -(a(7)^2-a(8)^2))/a(9)^2+0.5;

asxy(k)=1/sqrt((a(1)+s(1,k))^2-Xu(k)^2-Yu(k)^2);
Zu_a1(k)=((a(1)+s(1,k))-Xu(k)*Xu_a1(k)-Yu(k)*Yu_a1(k))*asxy(k);
Zu_a2(k)=0;
Zu_a3(k)=(-Xu(k)*Xu_a3(k)-Yu(k)*Yu_a3(k))*asxy(k);
Zu_a4(k)=0;
Zu_a5(k)=(-Yu(k)*Yu_a5(k))*asxy(k);
Zu_a6(k)=0;
Zu_r(k)=(-Xu(k)*Xu_r(k)-Yu(k)*Yu_r(k))*asxy(k);
Zu_b(k)=(-Yu(k)*Yu_b(k))*asxy(k);
Zu_h(k)=(-Yu(k)*Yu_h(k))*asxy(k);

asxYl(k)=-1/sqrt((a(2)+s(2,k))^2-Xl(k)^2-Yl(k)^2);
Zl_a1(k)=0;

```

```

Zl_a2(k)=((a(2)+s(2,k))-Xl(k)*Xl_a2(k)-Yl(k)*Yl_a2(k))*asxYl(k);
Zl_a3(k)=0;
Zl_a4(k)=(-Xl(k)*Xl_a4(k)-Yl(k)*Yl_a4(k))*asxYl(k);
Zl_a5(k)=0;
Zl_a6(k)=(-Yl(k)*Yl_a6(k))*asxYl(k);
Zl_r(k)=(-Xl(k)*Xl_r(k)-Yl(k)*Yl_r(k))*asxYl(k);
Zl_b(k)=(-Yl(k)*Yl_b(k))*asxYl(k);
Zl_h(k)=(-Yl(k)*Yl_h(k))*asxYl(k);

xyz(k)=1.0; % this term is for objective function F=Lce^2-a(10)^2
Xul(k)=Xu(k)-Xl(k); Yul(k)=Yu(k)-Yl(k); Zul(k)=Zu(k)-Zl(k);

Lce_a1(k)=(Xul(k)*(Xu_a1(k)-Xl_a1(k))+Yul(k)*(Yu_a1(k)
    -Yl_a1(k))+Zul(k)*(Zu_a1(k)-Zl_a1(k)))*xyz(k);
Lce_a2(k)=(Xul(k)*(Xu_a2(k)-Xl_a2(k))+Yul(k)*(Yu_a2(k)
    -Yl_a2(k))+Zul(k)*(Zu_a2(k)-Zl_a2(k)))*xyz(k);
Lce_a3(k)=(Xul(k)*(Xu_a3(k)-Xl_a3(k))+Yul(k)*(Yu_a3(k)
    -Yl_a3(k))+Zul(k)*(Zu_a3(k)-Zl_a3(k)))*xyz(k);
Lce_a4(k)=(Xul(k)*(Xu_a4(k)-Xl_a4(k))+Yul(k)*(Yu_a4(k)
    -Yl_a4(k))+Zul(k)*(Zu_a4(k)-Zl_a4(k)))*xyz(k);
Lce_a5(k)=(Xul(k)*(Xu_a5(k)-Xl_a5(k))+Yul(k)*(Yu_a5(k)
    -Yl_a5(k))+Zul(k)*(Zu_a5(k)-Zl_a5(k)))*xyz(k);
Lce_a6(k)=(Xul(k)*(Xu_a6(k)-Xl_a6(k))+Yul(k)*(Yu_a6(k)
    -Yl_a6(k))+Zul(k)*(Zu_a6(k)-Zl_a6(k)))*xyz(k);
Lce_r(k)=(Xul(k)*(Xu_r(k)-Xl_r(k))+Yul(k)*(Yu_r(k)-Yl_r(k))
    +Zul(k)*(Zu_r(k)-Zl_r(k)))*xyz(k);
Lce_b(k)=(Xul(k)*(Xu_b(k)-Xl_b(k))+Yul(k)*(Yu_b(k)-Yl_b(k))
    +Zul(k)*(Zu_b(k)-Zl_b(k)))*xyz(k);
Lce_h(k)=(Xul(k)*(Xu_h(k)-Xl_h(k))+Yul(k)*(Yu_h(k)-Yl_h(k))
    +Zul(k)*(Zu_h(k)-Zl_h(k)))*xyz(k);

f_a1(k)=2*Lce_a1(k);
f_a2(k)=2*Lce_a2(k);
f_a3(k)=2*Lce_a3(k);
f_a4(k)=2*Lce_a4(k);
f_a5(k)=2*Lce_a5(k);
f_a6(k)=2*Lce_a6(k);
f_r(k)=2*Lce_r(k);
f_b(k)=2*Lce_b(k);
f_h(k)=2*Lce_h(k);
f_Lct(k)=-2*a(10); %this term is for bjective function F=Lce^2-a(10)^2

end

J=[f_a1', f_a2', f_a3', f_a4', f_a5', f_a6', f_r', f_b', f_h', f_Lct']; % the Jacobian matrix

%%%% end derivation %%%

k1=cond(J); % condition number

if (k1) > 1e5 % if condition number > 1e5 , then terminate program
    disp(' condition number too big. (ill condition)');
    disp(' press CTR-C to terminate program');
end
%%%%% find increment %%%%

```

```
dphi=inv(J'*J)*J'*errorF';\n\na=a_old + dphi'; %% update initial parameters of a %%%\nmax(dphi);\nif max(abs(dphi)) < 1e-12 %% terminate iteration\nq=99999999999999\nstop=0;\nrepeat=0;\nelseif err_old < err(count) %% terminate iteration if the previous objective value is less than\nq=88888888888888 %% the current one.\nstop=0;\nrepeat=0;\nend\nerr_old=err(count);\nx=a;\ncount=count+1; %% count the iteration %%%\nend\nend
```

The Probe Positional Uncertainty Evaluation File

```
% File name: "hcm_uct.m"
% This program is to evaluate the HCMM's probe positional uncertainty
% Input files:
%   verif_p.dat: The probe positions where we want to evaluate the uncertainty. Matrix size
%   (m x 6)
%   verif_dl.dat: The strut displacement data at each probe position. Matrix size:(m x6)
%   covar_mtx.dat: The covariance between each kinematic parameters. Matrix size:(9 x 9)

clear
load verif_p.dat; % load the positional coordinates for evaluation;(Xu, Yu, Zu, XI, YI, ZI);size (mx6)
p1p2=verif_p'; % transpose into (6xm)

load verif_dl.dat; % load the strut displacement data; (dL1, dL2, dL3, dL4, dL5, dL6);size(mx6)
s=verif_dl'; % transpose the matrix into (6xm)

load covar_mtx.dat; % load the covariance between each parameters; see Table7-3 &7-5
cov_a=covar_mtx;

X(1:6)=43.10642755243507*ones(1,6);
X(7)=68.233; X(8)=X(7)/2; X(9)=X(8)*sqrt(3);

M=size(p1p2,2);
a=X;

Xu=p1p2(1,:);Yu=p1p2(2,:);Zu=p1p2(3,:);XI=p1p2(4,:);YI=p1p2(5,:);ZI=p1p2(6,:);
VarXu_old=0;

for k=1:M
    Xu_a1(k)=(a(1)+s(1,k))/a(7);
    Xu_a2(k)=0;
    Xu_a3(k)=-(a(3)+s(3,k))/a(7);
    Xu_a4(k)=0;
    Xu_a5(k)=0;
    Xu_a6(k)=0;
    Xu_r(k)=-0.5*((a(1)+s(1,k))^2-(a(3)+s(3,k))^2)/a(7)^2+0.5;
    Xu_b(k)=0;
    Xu_h(k)=0;

    XI_a1(k)=0;
    XI_a2(k)=(a(2)+s(2,k))/a(7);
    XI_a3(k)=0;
    XI_a4(k)=-(a(4)+s(4,k))/a(7);
    XI_a5(k)=0;
    XI_a6(k)=0;
    XI_r(k)=-0.5*((a(2)+s(2,k))^2-(a(4)+s(4,k))^2)/a(7)^2+0.5;
    XI_b(k)=0;
    XI_h(k)=0;

    Yu_a1(k)=(a(7)-a(8))/a(9)*(Xu_a1(k));

```

```

Yu_a2(k)=0;
Yu_a3(k)=-a(8)/a(9)*Xu_a3(k);
Yu_a4(k)=0;
Yu_a5(k)=-(a(5)+s(5,k))/a(9);
Yu_a6(k)=0;
Yu_r(k)=Xu(k)/a(9)-a(7)/a(9)+(a(7)-a(8))/a(9)*(Xu_r(k));
Yu_b(k)=-Xu(k)/a(9)+a(8)/a(9);
Yu_h(k)=-0.5*( (a(3)+s(3,k))^2 - (a(5)+s(5,k))^2 +2*Xu(k)*(a(7)-a(8))-(a(7)^2-a(8)^2) ) /a(9)^2+0.5;

Yl_a1(k)=0;
Yl_a2(k)=(a(7)-a(8))/a(9)*(Xl_a2(k));
Yl_a3(k)=0;
Yl_a4(k)=-a(8)/a(9)*Xl_a4(k);
Yl_a5(k)=0;
Yl_a6(k)=-(a(6)+s(6,k))/a(9);
Yl_r(k)=Xl(k)/a(9)-a(7)/a(9)+(a(7)-a(8))/a(9)*(Xl_r(k));
Yl_b(k)=-Xl(k)/a(9)+a(8)/a(9);
Yl_h(k)=-0.5*( (a(4)+s(4,k))^2 - (a(6)+s(6,k))^2 +2*Xl(k)*(a(7)-a(8))-(a(7)^2-a(8)^2) ) /a(9)^2+0.5;

asxy(k)=1/sqrt((a(1)+s(1,k))^2-Xu(k)^2-Yu(k)^2);
Zu_a1(k)=((a(1)+s(1,k))-Xu(k)*Xu_a1(k)-Yu(k)*Yu_a1(k))*asxy(k);
Zu_a2(k)=0;
Zu_a3(k)=(-Xu(k)*Xu_a3(k)-Yu(k)*Yu_a3(k))*asxy(k);
Zu_a4(k)=0;
Zu_a5(k)=(-Yu(k)*Yu_a5(k))*asxy(k);
Zu_a6(k)=0;
Zu_r(k)=(-Xu(k)*Xu_r(k)-Yu(k)*Yu_r(k))*asxy(k);
Zu_b(k)=(-Yu(k)*Yu_b(k))*asxy(k);
Zu_h(k)=(-Yu(k)*Yu_h(k))*asxy(k);

asxYl(k)=-1/sqrt((a(2)+s(2,k))^2-Xl(k)^2-Yl(k)^2);
Zl_a1(k)=0;
Zl_a2(k)=((a(2)+s(2,k))-Xl(k)*Xl_a2(k)-Yl(k)*Yl_a2(k))*asxYl(k);
Zl_a3(k)=0;
Zl_a4(k)=(-Xl(k)*Xl_a4(k)-Yl(k)*Yl_a4(k))*asxYl(k);
Zl_a5(k)=0;
Zl_a6(k)=(-Yl(k)*Yl_a6(k))*asxYl(k);
Zl_r(k)=(-Xl(k)*Xl_r(k)-Yl(k)*Yl_r(k))*asxYl(k);
Zl_b(k)=(-Yl(k)*Yl_b(k))*asxYl(k);
Zl_h(k)=(-Yl(k)*Yl_h(k))*asxYl(k);
xyzk=1/sqrt((Xu(k)-Xl(k))^2+(Yu(k)-Yl(k))^2+(Zu(k)-Zl(k))^2);
Xul(k)=Xu(k)-Xl(k); Yul(k)=Yu(k)-Yl(k); Zul(k)=Zu(k)-Zl(k);

Lc_a1(k)=(Xul(k)*(Xu_a1(k)-Xl_a1(k))+Yul(k)*(Yu_a1(k)-Yl_a1(k))+Zul(k)*(Zu_a1(k)-Zl_a1(k)))*xyz(k);
Lc_a2(k)=(Xul(k)*(Xu_a2(k)-Xl_a2(k))+Yul(k)*(Yu_a2(k)-Yl_a2(k))+Zul(k)*(Zu_a2(k)-Zl_a2(k)))*xyz(k);
Lc_a3(k)=(Xul(k)*(Xu_a3(k)-Xl_a3(k))+Yul(k)*(Yu_a3(k)-Yl_a3(k))+Zul(k)*(Zu_a3(k)-Zl_a3(k)))*xyz(k);
Lc_a4(k)=(Xul(k)*(Xu_a4(k)-Xl_a4(k))+Yul(k)*(Yu_a4(k)-Yl_a4(k))+Zul(k)*(Zu_a4(k)-Zl_a4(k)))*xyz(k);
Lc_a5(k)=(Xul(k)*(Xu_a5(k)-Xl_a5(k))+Yul(k)*(Yu_a5(k)-Yl_a5(k))+Zul(k)*(Zu_a5(k)-Zl_a5(k)))*xyz(k);
Lc_a6(k)=(Xul(k)*(Xu_a6(k)-Xl_a6(k))+Yul(k)*(Yu_a6(k)-Yl_a6(k))+Zul(k)*(Zu_a6(k)

```

```

-Zl_a6(k))*xyz(k);
Lc_r(k)=(Xul(k)*(Xu_r(k)-Xl_r(k))+Yul(k)*(Yu_r(k)-Yl_r(k))+Zul(k)*(Zu_r(k)
-Zl_r(k)))*xyz(k);
Lc_b(k)=(Xul(k)*(Xu_b(k)-Xl_b(k))+Yul(k)*(Yu_b(k)-Yl_b(k))+Zul(k)*(Zu_b(k)
-Zl_b(k)))*xyz(k);
Lc_h(k)=(Xul(k)*(Xu_h(k)-Xl_h(k))+Yul(k)*(Yu_h(k)-Yl_h(k))+Zul(k)*(Zu_h(k)
-Zl_h(k)))*xyz(k);
end

for k=1:M
VarXu_old=0;
VarYu_old=0;
VarZu_old=0;
VarXl_old=0;
VarYl_old=0;
VarZl_old=0;
VarLc_old=0;

U=[Xu_a1(k) Xu_a2(k) Xu_a3(k) Xu_a4(k) Xu_a5(k) Xu_a6(k) Xu_r(k) Xu_b(k) Xu_h(k)
Yu_a1(k) Yu_a2(k) Yu_a3(k) Yu_a4(k) Yu_a5(k) Yu_a6(k) Yu_r(k) Yu_b(k) Yu_h(k)
Zu_a1(k) Zu_a2(k) Zu_a3(k) Zu_a4(k) Zu_a5(k) Zu_a6(k) Zu_r(k) Zu_b(k) Zu_h(k)
Xl_a1(k) Xl_a2(k) Xl_a3(k) Xl_a4(k) Xl_a5(k) Xl_a6(k) Xl_r(k) Xl_b(k) Xl_h(k)
Yl_a1(k) Yl_a2(k) Yl_a3(k) Yl_a4(k) Yl_a5(k) Yl_a6(k) Yl_r(k) Yl_b(k) Yl_h(k)
Zl_a1(k) Zl_a2(k) Zl_a3(k) Zl_a4(k) Zl_a5(k) Zl_a6(k) Zl_r(k) Zl_b(k) Zl_h(k)
Lc_a1(k) Lc_a2(k) Lc_a3(k) Lc_a4(k) Lc_a5(k) Lc_a6(k) Lc_r(k) Lc_b(k) Lc_h(k)];

for i=1:size(U,2) %% see Equation 7-9 & 7-10 for calculating the variances
for j=1:size(U,2)
VarXu(k)=U(1,i)*U(1,j)*cov_a(i,j)+VarXu_old;
VarYu(k)=U(2,i)*U(2,j)*cov_a(i,j)+VarYu_old;
VarZu(k)=U(3,i)*U(3,j)*cov_a(i,j)+VarZu_old;
VarXu_old=VarXu(k);
VarYu_old=VarYu(k);
VarZu_old=VarZu(k);

VarXl(k)=U(4,i)*U(4,j)*cov_a(i,j)+VarXl_old;
VarYl(k)=U(5,i)*U(5,j)*cov_a(i,j)+VarYl_old;
VarZl(k)=U(6,i)*U(6,j)*cov_a(i,j)+VarZl_old;
VarXl_old=VarXl(k);
VarYl_old=VarYl(k);
VarZl_old=VarZl(k);

VarLc(k)=U(7,i)*U(7,j)*cov_a(i,j)+VarLc_old;
VarLc_old=VarLc(k);
end
end

VarpobsumX_old=0;
VarpobsumY_old=0;
VarpobsumZ_old=0;
for i=1:size(U,2)
for j=1:size(U,2)
VarpobsumX=U(1,i)*U(4,j)*cov_a(i,j)+VarpobsumX_old; %last term of Eqn.7-19
VarpobsumY=U(2,i)*U(5,j)*cov_a(i,j)+VarpobsumY_old;
VarpobsumZ=U(3,i)*U(6,j)*cov_a(i,j)+VarpobsumZ_old;
VarpobsumX_old=VarpobsumX;

```

```

VarpobsumY_old=VarpobsumY;
VarpobsumZ_old=VarpobsumZ;
end
end

Var_probe_X(k)=(1+5/35)^2*VarXl(k)+(5/35)^2*VarXu(k)-2*(1+5/35)*(5/35)*VarpobsumX;
Var_probe_Y(k)=(1+5/35)^2*VarYl(k)+(5/35)^2*VarYu(k)-2*(1+5/35)*(5/35)*VarpobsumY;
Var_probe_Z(k)=(1+5/35)^2*VarZl(k)+(5/35)^2*VarZu(k)-2*(1+5/35)*(5/35)*VarpobsumZ;

end

StdXu=sqrt(VarXu);
StdYu=sqrt(VarYu);
StdZu=sqrt(VarZu);
StdXl=sqrt(VarXl);
StdYl=sqrt(VarYl);
StdZl=sqrt(VarZl);

StdLc=sqrt(VarLc);

StdProbe_x=sqrt(Var_probe_X);
StdProbe_y=sqrt(Var_probe_Y);
StdProbe_z=sqrt(Var_probe_Z);

for i=1:M
    dPu(i)=sqrt(StdXu(i)^2+StdYu(i)^2+StdZu(i)^2);
    dPl(i)=sqrt(StdXl(i)^2+StdYl(i)^2+StdZl(i)^2);
    dProbe(i)=sqrt(StdProbe_x(i)^2+StdProbe_y(i)^2+StdProbe_z(i)^2);
end

% The following codes are used to plot the positional uncertainties graphics

k=1;
for i=1:size(p1p2,1)
    for j=1:size(p1p2,2)
        dd1(j,i)=StdXu(k);
        dd2(j,i)=StdYu(k);
        dd3(j,i)=StdZu(k);
        dd4(j,i)=StdLc(k);
        dd5(j,i)=StdXl(k);
        dd6(j,i)=StdYl(k);
        dd7(j,i)=StdZl(k);
        dd8(j,i)=StdProbe_x(k);
        dd9(j,i)=StdProbe_y(k);
        dd10(j,i)=StdProbe_z(k);
        k=k+1;
    end
end

for i=1:21----->change this value if the grid in Fig7-9 & 7-10 is not (21x21)
    XXu(i)=Xu(20*i+1);
end

for i=1:21 -----> change this value if the grid in Fig7-9 & 7-10 is not (21x21)
    YYu(i)=Yu(i);
end

```

```
figure(1)
surf(XXu,YYu,dd1)
xlabel('X')
ylabel('Y')
zlabel('Uc(Xu) inch')
title('Upper Sphere Position Uncertainty --Uc(Xu)')
figure(2)
surf(XXu,YYu,dd2)
xlabel('X')
ylabel('Y')
zlabel('Uc(Yu) inch')
title('Upper Sphere Position Uncertainty --Uc(Yu)')
figure(3)
surf(XXu,YYu,dd3)
xlabel('X')
ylabel('Y')
zlabel('Uc(Zu) inch')
title('Upper Sphere Position Uncertainty --Uc(Zu)')
figure(4)
surf(XXu,YYu,dd4)
xlabel('X')
ylabel('Y')
zlabel('Uc(Lc) inch')
%text(35,20,2.4e-5,'m=100 noise=+/-10e-6 inch')
title('Center Rod Length Uncertainty --Uc(Lc)')

figure(5)
surf(XXu,YYu,dd5)
xlabel('X')
ylabel('Y')
zlabel('Uc(Xl) inch')
title('Lower Sphere Position Uncertainty --Uc(Xl)')
figure(6)
surf(XXu,YYu,dd6)
xlabel('X')
ylabel('Y')
zlabel('Uc(Yl) inch')
title('Lower Sphere Position Uncertainty --Uc(Yl)')
figure(7)
surf(XXu,YYu,dd7)
xlabel('X')
ylabel('Y')
zlabel('Uc(Zl) inch')
title('Lower Sphere Position Uncertainty --Uc(Zl)')

figure(8)
surf(XXu,YYu,dd8)
xlabel('X')
ylabel('Y')
zlabel('Uc(Probe_x) inch')
title('Probe Position Uncertainty --Uc(Probe_x)')
figure(9)
surf(XXu,YYu,dd9)
xlabel('X')
ylabel('Y')
zlabel('Uc(Probe_y) inch')
```

```
title('Probe Position Uncertainty --Uc(Probe_y)')  
figure(10)  
surf(XXu,YYu,dd10)  
xlabel('X')  
ylabel('Y')  
zlabel('Uc(Probe_z) inch')  
title('Probe position Uncertainty --Uc(Probe_z)')
```

LIST OF REFERENCES

1. Jokiel, B., and Ziegert, J. C., "Development of a Parallel Architecture: Five-Axis Coordinate Measuring Machine," ASPE 1995 Annual Meeting Proceedings, pp.313-316.
2. Slocum, A. H., Precision Machine Design, Prentice Hall, Englewood Cliffs, New Jersey, 1992.
3. Jokiel, B., "Analysis of a Parallel Architecture Coordinate Measuring Machine," Master's Thesis, University of Florida, 1996.
4. Mevoli, M., "Design of a Servo Controlled Linear Actuator for a Hexapod Coordinate Measuring Machine," Master's Thesis, University of Florida, 1997.
5. Ziegert, J. C., and Mize, C. D., "Laser Ball Bar: A New Instrument for Machine Tool Metrology," Precision Engineering, Vol. 16, n4, 1994, pp. 259-267.
6. Kulkarni, R. B., "Design and Evaluation of a Technique to Find the Parametric Errors of a Numerically Controlled Machine Tool Using a Laser Ball Bar," Master's Thesis, University of Florida, 1996.
7. Donmez, A. "A General Metrology for Machine Tool Accuracy Enhancement: Theory, Application and Implementation," Ph.D. dissertation, Purdue University, 1985.
8. Mooring, B. W., "The Effect of Joint Axis Misalignment on Robot Positioning Accuracy," ASME, Proceeding of the 1983 International Computers in Engineering Conference and Exhibit, Chicago, IL, Vol. 2, 1983, pp. 151-155.
9. Craig, J. J., Introduction to Robotics: Mechanics and Control, Addison-Wesley Publishing Company, Inc., New York, 1989.
10. Mooring, B. W., Roth, Z. S. and Driels, M. R., Fundamentals of Manipulator Calibration, John Wiley & Sons, Inc., New York, 1991.
11. Driels, M. and Pathre, U., "Significance of Observation Strategy on the Robot Calibration Experiments," J. of Robotic Systems, Vol. 7, n2, 1990, pp.197-223.

12. Zhuang, H., Wang, K. and Roth, Z., "Optimal Selection of Measurement Configuration for Robot Calibration Using Simulated Annealing," Proceedings of the 1994 IEEE International Conference on Robotics and Automation, San Diego, CA, May 1994, pp. 393-398.
13. Zhuang, H., Wang, J. and Huang, W., "Optimal Planning of Robot Calibration Experiments by Genetic Algorithms," Proceedings of the 1996 IEEE International Conference on Robotics and Automation, Minneapolis, MN, April 1996, pp. 981-986.
14. Borm, J. H. and Meng, C. H., "Determination of optimal measurement configurations for robot calibration based on observability measure," International Journal of Robotics Research, Vol.10, n1, 1991, pp. 51-63.
15. Nahvi, A., Hollerbach, J. and Hayward V., "Calibration of a Parallel Robot Using Multiple Kinematic Closed Loops," Proceedings of the 1994 IEEE international Conferences on Robotics and Automation, San Diego, CA, May 1994, pp. 407-412.
16. Nahvi, A. and Hollerbach, J., "The Noise Amplification Index for Optimal Pose Selection in Robot Calibration," Proceedings of the 1996 IEEE International Conferences on Robotics and Automation, Minneapolis, MN, April 1996 pp. 647-654.
17. Kruth, J. P., Vanherck, L. and Jonge, L., "Self-Calibration Method and Software Error Correction for Three Dimensional Coordinate Measuring Machines Using Artifact Measurements," Journal of the International Measurement Confederation, Vol. 14, n2, 1994, pp.157-167.
18. Zhang, G. X. and Zang, Y. F., "A Method for Machine Geometry Calibration Using 1-D Ball Array," Annals of CIRP, Vol. 40, n1, 1991, pp. 519-522.
19. Belforte, B., "Coordinate Measuring Machines and Machine Tools Self-Calibration and Error Correction," Annals of CIRP, Vol. 36, 1987, pp. 359-364.
20. Pahk, H. J. and Burdekin, M., "Evaluation of the Effective Parametric Errors in Coordinate Measuring Machines Using the Locus of Stylus on the Horizontal Plane," Proc. Inst. Mech. Eng. Part B, Journal of Engineering Manufacture, Vol. 205, n B2, 1991, pp. 123-138.
21. Sartori, S. and Zhang, G.X., "Geometric Error Measurement and Compensation of Machine," CIRP annals, Vol. 44, n2, 1995, pp. 599-609
22. Bennett, D. J. and Hollerbach, J. M., "Autonomous Calibration of Single-Loop Closed Kinematic Chains Formed by Manipulators with Passive Endpoint Constraints," IEEE trans. Robotics and Automation, Vol. 7, 1991, pp. 597-606.

23. Khoshzaban, M., Sassani, F. and Lawrence, P. D., "Autonomous Kinematic Calibration of Industrial Hydraulic Manipulators," *Robotics and Manufacturing*, Vol. 4, 1992, pp. 577-584.
24. Zhuang, H., "A Self-Calibration Approach to Extrinsic Parameter Estimation of Stereo Cameras," *Robotics and Autonomous Systems*, Vol. 15, n3, 1995, pp. 189-197.
25. El-Khasawneh, B. S. and Ferreira, P. M., "On Using Parallel Manipulators as Machine Tools," *Transactions of NAMRI/SME*, Vol. 25, 1997, pp. 305-310.
26. Stewart, D., "A Platform with Six Degrees of Freedom," *Proceedings of Institution of Mechanical Engineering*, Vol. 180, Part 1, No. 15, 1965-66, pp. 371-386
27. Merlet, J. P., "An Algorithm for the Forward Kinematics of General 6 D.O.F. Parallel Manipulators," *Technical Report 1331*, INRIA, France, November 1990.
28. Raghavan, M., "The Stewart Platform of General Geometry Has 40 Configurations," *Advances in Design Automation*, Vol. 2, 1991, pp. 397-402.
29. Wang, J. and Masory, O., "On the Accuracy of a Stewart Platform - Part 1: The Effect of Manufacturing Tolerances," *Proceedings of the 1993 International Conference on Robotics and Automation*, Atlanta, GA, May 1993, pp. 114-120.
30. Wang, J., Masory, O., and Zhuang, H., "On the Accuracy of a Stewart Platform - Part II: Kinematic Calibration and Compensation," *Proceedings of the 1993 International Conference on Robotics and Automation*, Atlanta, GA, May 1993, pp. 725-731.
31. Ropponen, T. and Arai, T., "Accuracy Analysis of a Modified Stewart Platform Manipulator," *The proceedings of 1995 IEEE International Conference on Robotics and Automation*, Nagoya, Aichi, Japan May 1995, pp. 521-525.
32. Patel, A. J. and Ehmann, K. F., "Volumetric Error Analysis of a Stewart Platform Based Machine Tool," *CIRP Annals*, v46, n1, 1997, pp. 287-290.
33. Soons, J. A., "Error Analysis of a Hexapod Machine Tool," *Proceedings of the 3rd Lamdamap conference*, Huddersfield, UK, July 1997, pp. 347-358.
34. Zhuang, H. and Roth, Z., "Method for Kinematic Calibration of Stewart Platforms," *Journal of Robotic Systems*, Vol. 10, No. 3, 1993, pp. 391-405.
35. Soons, J. A. and Schellekens, P. H., "On the Calibration of Multi-Axis Machines Using Distance Measurements," *Proceedings International Symposium on Metrology and Quality Control in Production*, 1992, pp. 321-340.

36. Maurine, P. and Dombre, E., "A Calibration for the Parallel Robot Delta 4," Proceedings of the 1996 IEEE International Conference on Robotic and Automation, Minneapolis, MN, April 1996, pp. 975-980.
37. Wallack, A. S., Mazon, I., "Calibration of Four Degrees of Freedom Robotworld Modules," Proceedings of the 1996 IEEE International Conference on Robotics and Automation, Minneapolis, MN, April 1996, pp. 987-993.
38. Zhuang, H. and Liu, L., "Self-Calibration of a Class of Parallel Manipulators," Proceeding of the 1996 IEEE International Conference on Robotics and Automation, Minneapolis, MN, April 1996, pp. 994-999.
39. Hollerbach, J. M. and Lokhorst, D. M., "Closed-Loop Kinematic Calibration of the RSI 6-DOF Hand Controller," IEEE Transaction on Robotics and Automation, Vol. 11, No. 3, June 1995, pp. 352-359.
40. Klema, V. C. and Laub, A. J., "The Singular Value Decomposition: Its Computation and Some Application," IEEE Transaction on Automatic Control, Vol. AC-25, No. 2, April 1980, pp. 164-176.
41. Leon, S. J., Linear Algebra with Applications, 4th edition McMillian College Publish Company, New York.
42. Taylor, B.N., and Kuyatt, C.E., "Guidelines for Evaluating and Expressing the Uncertainty of NIST Measurement Result," NIST Technical Note 1297, 1994.
43. Incropera, F.P. and Dewitt, D., Fundamentals of Heat and Mass Transfer, 4th edition, John Wiley & Sons Inc., New York, 1996.
44. Structure Research & Analysis Corp., COSMOS/M- Basic FEA System User Guide, Version 1.71, May 1994.
45. Ozisik, M. N., Heat Transfer - A Basic Approach, McGraw-Hill, Inc., New York, 1985.
46. Swyt, D.A., "Uncertainties in Dimensional Measurements Made at Nonstandard Temperatures," J. of Research of NIST, Vol. 99, No.1, 1994, pp. 31-44.
47. Yeager, C. D., "Design of A Machine Base and Actuator Joint Connections for A Hexapod Coordinate Measuring Machine," Master's Thesis, University of Florida, 1998.

BIOGRAPHICAL SKETCH

The author was born on December 12, 1963, in Tainan, Taiwan. He attended the National Central University at Chung-Li, Taiwan, where he received his Bachelor's degree in 1986 from the Department of Mechanical Engineering.

While completing his undergraduate education, he served in the Taiwanese Army as a second lieutenant in the tank troop for two years. After finishing the compulsory military service, he worked for six months with the General Electric (USA) Solid State Ltd., as a maintenance engineer. After the brief employment with GE, he joined the Aeronautic Industry Development Center at Tai-Chung, Taiwan, where he was a supervisor in the Tool Shop for building the master models for fighter planes.

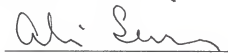
The author came to the United States in the fall of 1991 to pursue higher education. He completed the Master of Science program in mechanical engineering at the University of Florida in 1993. The author then moved to the University of Wisconsin-Madison, where he married Yalin. In the fall of 1994, he returned to the University of Florida to continue in the doctoral program in mechanical engineering. After completing his doctorate, he will be joining the Cummins Engine Company at Columbus, Indiana as a metrology engineer.

I certify that I have read this study and that in my opinion it conforms to acceptable standards of scholarly presentation and is fully adequate, in scope and quality, as a dissertation for the degree of Doctor of Philosophy.



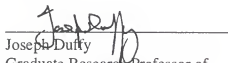
John C. Ziegert, Chairman
Associate Professor of Mechanical
Engineering

I certify that I have read this study and that in my opinion it conforms to acceptable standards of scholarly presentation and is fully adequate, in scope and quality, as a dissertation for the degree of Doctor of Philosophy.



Ali A. Seireg
Ebaugh Professor of Mechanical
Engineering

I certify that I have read this study and that in my opinion it conforms to acceptable standards of scholarly presentation and is fully adequate, in scope and quality, as a dissertation for the degree of Doctor of Philosophy.



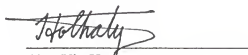
Joseph Duffy
Graduate Research Professor of
Mechanical Engineering

I certify that I have read this study and that in my opinion it conforms to acceptable standards of scholarly presentation and is fully adequate, in scope and quality, as a dissertation for the degree of Doctor of Philosophy.



Paul A. C. Mason
Assistant Professor of Mechanical
Engineering

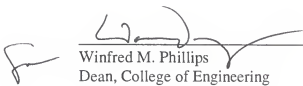
I certify that I have read this study and that in my opinion it conforms to acceptable standards of scholarly presentation and is fully adequate, in scope and quality, as a dissertation for the degree of Doctor of Philosophy.



Chat Yin Ho
Professor of Mathematics

This dissertation was submitted to the Graduate Faculty of the College of Engineering and to the Graduate School and was accepted as partial fulfillment of the requirements for the degree of Doctor of Philosophy.

May, 1998



Winfred M. Phillips
Dean, College of Engineering

Karen A. Holbrook
Dean, Graduate School